

Wind and Temperature Measurements by Doppler Lidar in the Arctic Middle Atmosphere

Dissertation

zur Erlangung des akademischen Grades

doctor rerum naturalium (Dr. rer. nat.)

der Mathematisch-Naturwissenschaftlichen Fakultät der Universität Rostock

vorgelegt von

Jens Hildebrand,

geboren am 30. Juni 1983 in Dresden,

wohnhaft in Bad Doberan

1. Gutachter: Prof. Dr. Franz-Josef Lübken,
Universität Rostock

2. Gutachter: Prof. Dr. Patrick Joseph Espy,
Norges teknisk-naturvitenskapelige universitet, Trondheim

Datum des Einreichens der Arbeit: 25. Oktober 2013

Datum der Verteidigung: 4. April 2014

Abstract

Wind and temperature are fundamental parameters for a comprehensive understanding of atmosphere dynamics. Especially the propagation of waves strongly depends on the background wind field, which thus influences the coupling of atmospheric layers. Wind measurements with high spatial and temporal resolution within the middle atmosphere are rare. The Rayleigh/Mie/Raman (RMR) lidar at the Arctic Lidar Observatory for Middle Atmosphere Research (ALOMAR) in Northern Norway (69° N, 16° E) routinely measures temperatures and aerosols since 1997, wind measurements are performed since 2009. The wind retrieval relies on measuring the Doppler shift of light which is backscattered by moving air molecules. It is challenging since the relative Doppler shift is on the order of $\Delta\nu/\nu_0 \sim 10^{-8}$ only. The method uses a steep edge of an absorption line of molecular iodine to resolve small frequency variations of the backscattered light. The ALOMAR RMR lidar is designed as a twin lidar with two steerable telescopes, which allows measuring two wind components simultaneously. To provide a comprehensive picture of the atmosphere and its dynamics simultaneous wind and temperature measurements are required. Such information is delivered by the current retrieval in the altitude region from 30 to 80 km.

This thesis presents the instrumental setup and the wind retrieval method. Measurements of vertical wind, simultaneous measurements of the same horizontal wind component with both telescopes, and other remote sensing techniques are used for validation. Winds and temperatures measured from 2009 to 2012 in the Arctic winter reveal large seasonal and year-to-year variability, especially during sudden stratospheric warmings and afterward. On short time scales gravity waves are observed in temperatures and winds. Their temporal evolution during long measurement of 60 h is investigated.

Kurzfassung

Wind und Temperatur sind für ein umfassendes Verständnis der Dynamik der Atmosphäre fundamentale Parameter. Besonders die Ausbreitung von Wellen hängt stark vom Hintergrundwindfeld ab. Windmessungen in der mittleren Atmosphäre mit hoher räumlicher und zeitlicher Auflösung sind selten. Das Rayleigh/Mie/Raman-Lidar (RMR-LIDAR) in dem ALOMAR-Observatorium (Arctic Lidar-Observatory for Middle Atmosphere Research) in Nordnorwegen (69° N, 16° O) misst seit 1997 routinemäßig Temperaturen und Aerosole, Windmessungen werden seit 2009 durchgeführt. Das Prinzip der Windmessung beruht auf der Doppler-Verschiebung, die Licht erfährt, das an sich bewegenden Luftteilchen rückgestreut wird. Da die relative Doppler-Verschiebung $\Delta\nu/\nu_0$ nur etwa 10^{-8} beträgt, ist die Windbestimmung sehr anspruchsvoll. Die Methode nutzt die steile Flanke einer Absorptionslinie molekularen Iods um kleine Frequenzveränderungen des rückgestreuten Lichts aufzulösen. Das ALOMAR RMR-Lidar ist ein Zwillingssystem mit zwei schwenkbaren Teleskopen, es kann zwei Windkomponenten gleichzeitig messen. Um ein umfassendes Bild der Atmosphäre und ihrer Dynamik zu erhalten, sind gleichzeitige Wind- und Temperaturmessungen nötig. Die gegenwärtige Auswertung erlaubt solche Analysen im Höhenbereich von 30 bis 80 km.

Diese Arbeit erläutert den instrumentellen Aufbau und die Windanalysetechnik. Vertikalwindmessungen, gleichzeitige Messungen des Zonalwindes mit beiden Teleskopen und andere Fernerkundungstechniken werden zur Validierung genutzt. Winde und Temperaturen, die von 2009 bis 2012 im arktischen Winter gemessen wurden, zeigen große saisonale und Jahr-zu-Jahr-Variationen, insbesondere während und nach stratosphärischen Erwärmungen. Auf kurzen Zeitskalen werden im Wind und in der Temperatur Schwerewellen beobachtet.

Contents

| | | |
|----------|--|-----------|
| 1 | Introduction | 13 |
| 2 | Atmospheric dynamics | 17 |
| 2.1 | Wind approximations | 17 |
| 2.1.1 | Geostrophic wind | 17 |
| 2.1.2 | Gradient wind | 17 |
| 2.1.3 | Thermal wind | 18 |
| 2.2 | Gravity Waves | 18 |
| 2.3 | Mean circulation | 19 |
| 2.4 | Polar vortex and sudden stratospheric warmings | 21 |
| 3 | Measuring wind in the middle atmosphere | 23 |
| 3.1 | Lidar | 23 |
| 3.1.1 | Principle | 23 |
| 3.1.2 | Scattering mechanisms | 24 |
| 3.1.3 | Doppler effect | 25 |
| 3.1.4 | Different techniques to derive wind by lidar | 27 |
| 3.2 | Other techniques to measure winds in the middle atmosphere | 28 |
| 3.2.1 | Meteorological rockets | 28 |
| 3.2.2 | Balloons | 29 |
| 3.2.3 | Radars | 30 |
| 3.2.4 | Airglow observations | 30 |
| 3.2.5 | Microwave radiometers | 31 |
| 4 | The Doppler Rayleigh Iodine Spectrometer | 35 |
| 4.1 | Principle of DORIS | 35 |
| 4.2 | Instrumental setup | 37 |
| 4.2.1 | The ALOMAR RMR lidar | 38 |
| 4.2.2 | DORIS setup | 40 |
| 4.3 | Wind retrieval | 42 |
| 4.3.1 | Temperature retrieval | 45 |
| 4.3.2 | Measurement uncertainties | 45 |
| 4.4 | Calibration | 45 |
| 4.4.1 | Experimental setup for calibration | 46 |
| 4.4.2 | Iodine spectrum and stabilization frequency | 46 |
| 4.4.3 | Entrance ratio | 49 |
| 4.4.4 | Validity of a calibration | 50 |

Contents

| | | |
|--|--|------------|
| 4.5 | Performance monitoring | 50 |
| 4.5.1 | Seeder Doppler ratio | 50 |
| 4.5.2 | Laser frequency offset | 51 |
| 4.6 | Summary – exemplary retrieval | 53 |
| 5 | Data set and validation | 55 |
| 5.1 | Data set | 55 |
| 5.2 | Validation and intercomparison | 57 |
| 5.2.1 | Measurements of vertical wind speed | 58 |
| 5.2.2 | Coplanar wind measurements | 59 |
| 5.2.3 | Combination with the ALOMAR sodium lidar | 62 |
| 6 | Geophysical results | 65 |
| 6.1 | Monthly mean winds and temperatures in Arctic winter | 66 |
| 6.1.1 | Comparison to other wind data sets | 68 |
| 6.2 | Variability in winds and temperatures in January | 69 |
| 6.2.1 | January 2010 and January 2012 | 71 |
| 6.3 | Case study – gravity waves in wind and temperature | 75 |
| 6.3.1 | Hodograph analysis | 78 |
| 6.3.2 | Gravity wave energy density | 82 |
| 7 | Summary and outlook | 85 |
| 7.1 | Summary and conclusions | 85 |
| 7.2 | Outlook | 87 |
| Appendix A Data processing | | 91 |
| A.1 | Database | 91 |
| A.2 | Basic processing | 91 |
| A.3 | Temperature retrieval | 91 |
| A.4 | Wind retrieval | 92 |
| A.5 | Laser frequency offset | 92 |
| A.6 | Used software | 93 |
| Appendix B Calibration in details | | 95 |
| B.1 | Instrumental modifications | 95 |
| B.2 | Lists of calibration measurements | 98 |
| Appendix C Estimates | | 105 |
| C.1 | Projecting line-of-sight wind to horizontal wind | 105 |
| C.2 | Different approaches to derive temperature deviations | 107 |
| Appendix D Detailed wind results | | 109 |
| D.1 | Vertical wind measurements | 109 |
| D.2 | Coplanar wind measurements | 111 |
| D.3 | Winds and temperatures in Arctic winter | 112 |
| D.3.1 | Cumulated monthly mean winds and temperatures in Arctic winter | 112 |
| D.3.2 | Monthly mean winds and temperatures in Arctic winter for the years 2009 to 2012 | 112 |

List of Tables

| | | |
|-----|--|-----|
| 3.1 | Scattering mechanisms | 25 |
| 3.2 | Middle atmosphere wind lidars | 29 |
| 3.3 | Remote sensing instruments for wind measurements in the middle atmosphere | 32 |
| 5.1 | Nighttime-measurement hours per year and month | 56 |
| 5.2 | Comparison of zonal winds measured by RMR lidar data and Na lidar data | 64 |
| 6.1 | Deduced background and wave parameters | 82 |
| B.1 | List of scans of the iodine-vapor cell at the detection system | 100 |
| B.2 | Measured iodine cell transmittance $T_{I_2 \nu_0}$ | 100 |
| B.3 | List of calibration measurements to determine entrance ratio | 102 |
| B.4 | List of test measurements with the LPS | 103 |
| D.1 | Nighttime measurements of vertical pointing NWT which last for 1 h or longer | 109 |
| D.2 | Nighttime measurements of vertical pointing SET which last for 1 h or longer | 110 |
| D.3 | Nighttime measurements with both telescopes pointing coplanar which last for longer than 1 h | 111 |

List of Tables

List of Figures

| | | |
|------|---|----|
| 1.1 | Vertical profiles of temperature, zonal wind, and meridional wind for summer and winter | 13 |
| 1.2 | Geographic location of ALOMAR | 14 |
| 2.1 | Latitude-height sections of zonal mean temperature and zonal mean zonal wind | 20 |
| 3.1 | Altitude coverage of different wind measurement techniques for the middle atmosphere | 32 |
| 4.1 | Effect of wind and temperature on the Cabannes line | 36 |
| 4.2 | Sketch of the DORIS setup | 36 |
| 4.3 | Effect of wind and temperature on Doppler signal and Doppler ratio | 36 |
| 4.4 | Modeled Doppler ratio as function of temperature and wind speed | 37 |
| 4.5 | Schematic setup of the ALOMAR RMR lidar | 38 |
| 4.6 | Scheme of the detection system of the ALOMAR RMR lidar | 39 |
| 4.7 | Scheme of the control loop for the seed laser frequency | 40 |
| 4.8 | Laser pulse spectrometer | 41 |
| 4.9 | Exemplary lidar backscatter signal | 42 |
| 4.10 | Exemplary lidar count rate during calibration measurement | 46 |
| 4.11 | Frequency scan, results from seed laser platform | 47 |
| 4.12 | Determination of iodine spectrum and stabilization frequency | 48 |
| 4.13 | Determination of entrance ratio during seed laser scan | 49 |
| 4.14 | Exemplary time series of seeder Doppler ratio | 51 |
| 4.15 | Retrieval of frequency offset | 52 |
| 4.16 | Exemplary time series of frequency offset and resultant wind offset | 53 |
| 4.17 | Exemplary wind and temperature retrieval | 53 |
| 5.1 | Seasonal distribution of nighttime-measurement hours | 56 |
| 5.2 | Measurements as function of season and time of day | 57 |
| 5.3 | Distribution of measurement lengths for the months November to March for the years 2009 to 2012 | 58 |
| 5.4 | Exemplary altitude profiles of vertical wind with internal and atmospheric calibration | 59 |
| 5.5 | Coplanar zonal wind measurement on 19.01.2012 | 60 |
| 5.6 | Coplanar zonal wind measurement on 19.11.2009 | 61 |
| 5.7 | Nightly mean altitude profiles of zonal wind measured by RMR and Na lidar . | 63 |
| 5.8 | Time-height section of zonal wind measured by RMR and Na lidar | 63 |
| 5.9 | Single altitude profiles of zonal wind measured by RMR and Na lidar | 64 |

List of Figures

| | | |
|------|--|-----|
| 6.1 | Sounding volumes of different lidar and radar instruments | 65 |
| 6.2 | Cumulated monthly mean temperatures and horizontal winds | 67 |
| 6.3 | January mean temperatures and horizontal winds for the years 2009 to 2012 | 70 |
| 6.4 | Single altitude profiles of temperatures and horizontal winds in January 2010 and 2012 | 71 |
| 6.5 | Temperatures, horizontal winds, and polar vortex during January 2010 | 73 |
| 6.6 | Temperatures and horizontal winds during January and February 2012 | 74 |
| 6.7 | Time-height sections of temperature, zonal wind, and meridional wind, and respective mean altitude profiles for 21.–23.01.2012 | 76 |
| 6.8 | Time-height sections of temperature deviation, zonal wind deviation, and meridional wind deviation for 21.–23.01.2012 | 77 |
| 6.9 | Combination of temperature and wind deviations | 78 |
| 6.10 | Exemplary altitude profiles of temperature deviation for 21.–23.01.2012 | 79 |
| 6.11 | Altitude profiles of temperature deviation, zonal wind deviation, meridional wind deviation and respective hodographs | 80 |
| 6.12 | Altitude profiles of gravity wave potential and kinetic energy density | 83 |
| A.1 | Exemplary laser pulse form | 93 |
| B.1 | Effect of improperly mounted mirrors for etalon bypass on entrance ratio | 97 |
| B.2 | Effect of RFS phase lag on entrance ratio | 99 |
| C.1 | Different methods to derive temperature deviations | 107 |
| D.1 | Cumulated monthly mean temperatures and horizontal winds | 113 |
| D.2 | Monthly mean temperatures and horizontal winds for 2009 | 114 |
| D.3 | Monthly mean temperatures and horizontal winds for 2010 | 115 |
| D.4 | Monthly mean temperatures and horizontal winds for 2011 | 116 |
| D.5 | Monthly mean temperatures and horizontal winds for 2012 | 117 |

List of Acronyms and Symbols

This lists do not contain acronyms and symbols which are used in one chapter only.

Acronyms

| | |
|---------|--|
| ALOMAR | Arctic Lidar Observatory for Middle Atmosphere Research |
| DoRIS | Doppler Rayleigh Iodine Spectrometer |
| ECMWF | European Centre for Medium-Range Weather Forecasts |
| HWM07 | Horizontal Wind Model, version 2007 |
| IAP | Leibniz-Institute for Atmospheric Physics, Kühlungsborn |
| LPS | Laser pulse spectrometer |
| MF | Medium frequency; 0.3–3 MHz |
| NWT | North-West Telescope |
| RFS | Rotary fiber selector |
| RMR | Rayleigh/Mie/Raman; scattering mechanisms used by the ALOMAR RMR lidar |
| SET | South-East Telescope |
| SKIYMET | All-sky interferometer meteor radar |
| SSW | Sudden stratospheric warming |
| UT | Universal Time; in fact Coordinated Universal Time (UTC) |

Symbols

| | |
|---------------------|---|
| c | Speed of light |
| D_{meas} | Measured Doppler ratio |
| D'_{meas} | Rescaled measured Doppler ratio |
| D_{model} | Modeled Doppler ratio |
| D_{seeder} | Seeder Doppler ratio |
| E_{tel} | Entrance ratio; E_{NWT} or E_{SET} |
| f | Coriolis parameter |
| g | Gravitational acceleration |
| k | Zonal wave number |
| k_{B} | Boltzmann constant |
| l | Meridional wave number |
| λ | Light's wavelength |
| m | Vertical wave number |
| N | Buoyancy frequency, also referred to as Brunt-Väisälä frequency |
| ν | Light's frequency |
| ω | Observed wave frequency |

List of Acronyms and Symbols

| | |
|----------------|---|
| $\hat{\omega}$ | Intrinsic wave frequency |
| T | Temperature |
| T_{I_2} | Transmittance of the iodine-vapor cell |
| u | Zonal wind speed |
| \bar{u}_h | Background horizontal wind speed in the direction of wave propagation |
| v | Meridional wind speed |
| $v_{l.o.s.}$ | Line-of-sight wind speed |
| w | Vertical wind speed |

Chapter 1 Introduction

Earth's atmosphere is a gaseous layer around Earth. It consists mainly of nitrogen (78 %), oxygen (21 %), and argon (0.9 %), and some trace gases. The atmosphere protects and ensures life on Earth. Some constituents filter ionizing radiation from space and the Sun which causes harm in organisms. Others (like water vapor, carbon dioxide, methane, and ozone) are responsible for the natural greenhouse effect, which ensures quite warm temperatures needed for life. And finally, nearly all animals and plants need oxygen to breathe.

While the atmosphere's chemical composition does not change substantially with height up to about 100 km altitude (referred to as homosphere), it is divided into layers by means of temperature gradient. Altitude profiles of temperature, and zonal and meridional wind for typical summer and winter state for the location of ALOMAR are shown in Fig. 1.1. These profiles will be discussed shortly in the following; detailed explanations are presented in Chap. 2.

First, focus on the left panel of Fig. 1.1. Starting from ground, the lowest layer is characterized by negative temperature gradient, i.e., temperature decreases with increasing altitude.

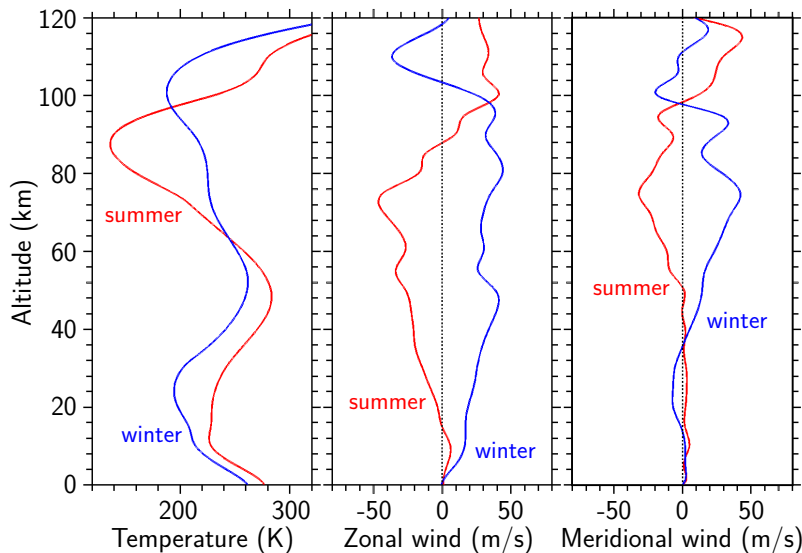


Figure 1.1 Vertical profiles of temperature, zonal, and meridional wind for summer and winter. The temperature profiles are extracted from the NRLMSISE-00 reference atmosphere (Picone *et al.*, 2002). The wind speed profiles are extracted from the HWM07 model (Drob *et al.*, 2008). The summer profiles (red) correspond to 1 July, the winter profiles (blue) to 1 January; extracted for the location of ALOMAR (69° N, 16° E).

Chapter 1 Introduction

This layer is referred to as troposphere, its upper border is the tropopause. The next layer, with positive temperature gradient, is positive, is named stratosphere and is terminated by the stratopause. It is followed by the mesosphere, again with negative temperature gradient, until the mesopause. The highest layer is the thermosphere, which is characterized by steep increase of temperature with altitude. Stratosphere and mesosphere together form the middle atmosphere. In the troposphere and the stratosphere the temperature is higher in summer than in winter. Regarding higher solar irradiation during summer this is obvious. Contrary the mesosphere is coldest in summer. This counterintuitive behavior is elucidated in Sect. 2.3.

Zonal wind (see middle panel of Fig. 1.1) is eastward in the entire middle atmosphere during winter. This feature in zonal wind is referred to as polar vortex, highest wind speeds occur around the stratopause. Around the mesopause the winter zonal wind reverses to westward wind in the lower thermosphere. During summer zonal wind is weak eastward in the troposphere and westward in the stratosphere and mesosphere. In the lower thermosphere summer zonal wind is again eastward. Meridional winds (see right panel of Fig. 1.1) are generally weaker than zonal winds, especially in the troposphere and the stratosphere. In the mesosphere meridional wind is northward during winter and southward during summer.

The counterintuitive paradoxon of the warm winter mesopause and cold summer mesopause is particularly pronounced in polar regions. This is also true for the strong eastward winds in winter. This, and further special characteristics, make the Arctic exceptionally interesting for atmospheric research. A unique set of instruments for studies of the entire atmosphere is assembled on the Norwegian island of Andøya, which is located north of the Arctic circle (see Fig. 1.2(a)). Sounding rockets are launched from the Andøya Rocket Range since 1962 (*Ege-*

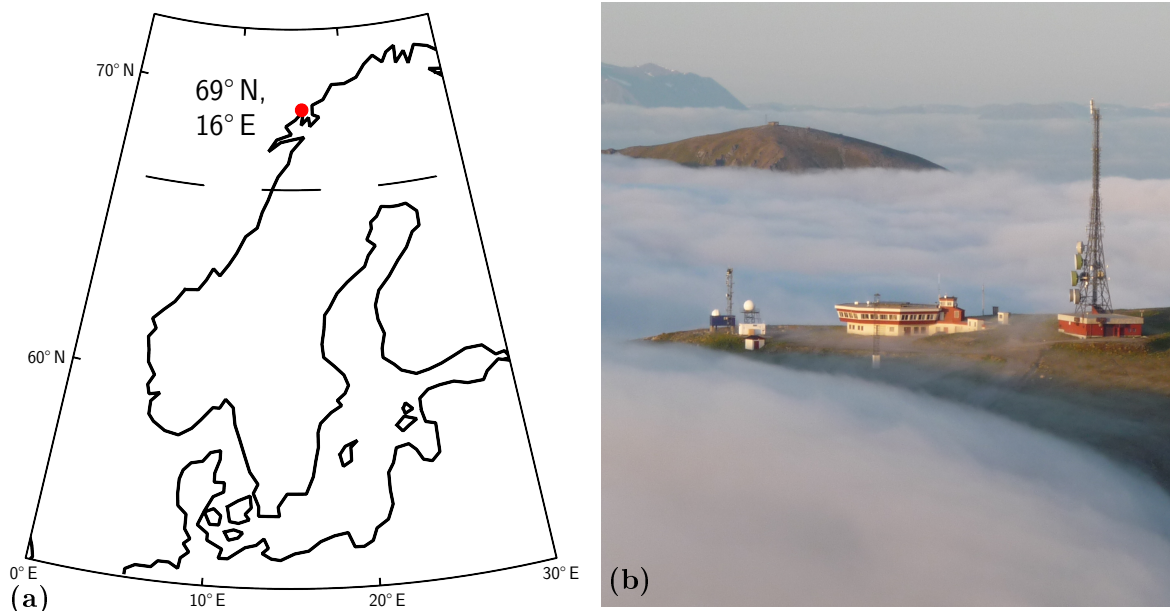


Figure 1.2 Geographic location of ALOMAR: (a) Map of Scandinavia and the Baltic region, showing the location of ALOMAR (red dot) on the island of Andøya in Northern Norway; (b) the ALOMAR observatory on top of Ramnan mountain (380 m a.s.l.) above low clouds in July 2009.

land, 2000). Since April 1984 a sodium resonance lidar was in operation nearby (*Fricke and von Zahn, 1985*). This lidar was the first lidar that detected a noctilucent cloud (*Hansen et al., 1989*). In June 1994 a new lidar observatory (Arctic Lidar Observatory for Middle Atmosphere Research, ALOMAR, see Fig. 1.2(b)) started operation. Today it hosts four lidar instruments: a Rayleigh/Mie/Raman lidar for tropospheric studies (troposphere lidar; *Frioud et al. (2006)*), an ozone lidar (*Hoppe et al., 1995*), a sodium resonance lidar (*She et al., 2002*), and a Rayleigh/Mie/Raman lidar for middle atmosphere studies (ALOMAR RMR lidar; *von Zahn et al. (2000)*). The first permanently installed radar on Andøya, the ALOMAR SOUSY¹ radar, started operation in July 1994 (*Singer et al., 1995*). Today several radar systems for atmospheric studies (see Sect. 3.2.3) are part of ALOMAR.

The counterintuitive paradoxon of the warm winter mesopause and cold summer mesopause can be explained only with the help of gravity waves (see Sect. 2.2). The propagation and filtering of these atmospheric waves is crucially determined by the background wind field. Hence, knowledge of horizontal winds in the entire atmosphere is important for a comprehensive understanding of the dynamics and the thermal structure of the atmosphere. This thesis is focussed on wind measurements in the Arctic middle atmosphere by a complex lidar system. Lidars are very useful instruments for atmospheric studies, since the combination of different lidar techniques allows to cover the whole lower and middle atmosphere from the ground up to about 110 km altitude with a fair temporal and vertical resolution. The ALOMAR RMR lidar, which is used for this thesis, started operation in June 1994. It measures temperatures and aerosols in the middle atmosphere on a routine basis since 1997 (*Schöch, 2007; Fiedler et al., 2011*). Since 2009 the wind measurement capability of the ALOMAR RMR lidar, called Doppler Rayleigh Iodine Spectrometer (DORIS), is used to measure wind speeds in the middle atmosphere (*Baumgarten, 2010*). By now wind speeds and temperatures in the middle atmosphere can be measured simultaneously between about 30 and 80 km altitude. This thesis introduces the wind retrieval method in detail and presents the wind results from the winter seasons 2009 to 2012.

Structure of this thesis

Chapter 2 gives a short introduction about some aspects of atmospheric dynamics. An overview of methods to measure winds in the middle atmosphere is presented in Chap. 3. The experimental setup and the retrieval to derive winds with the ALOMAR RMR lidar are described in Chap. 4. The data set and validation of the derived wind speeds are presented in Chap. 5. Afterward, geophysical results are shown in Chap. 6; this includes the mean state, a more detailed analysis of variability from year to year and within single months, and a case study of a measurement spanning three days, which shows some interesting features of wave-like structures. The results of this thesis are summarized in Chap. 7, together with an outlook to future improvements. The appendix presents further details of data processing (App. A) and calibration measurements (App. B). Different approaches for the derivation of horizontal wind speeds from line-of-sight wind speeds discussed in App. C. That section also describes different approaches for the calculation of temperature perturbations. Detailed results from selected measurements and monthly mean winds and temperatures are presented in App. D.

¹Sounding System

Chapter 2 Atmospheric dynamics

What is wind? Wind is the directed motion of air caused by atmospheric pressure differences. The strength of wind is determined mainly by the pressure gradient. Although the cause for wind is the motion of air from an area of higher pressure to an area of lower pressure, the wind direction is not straight from the high pressure area to the low pressure area. This is due to different reasons, which are presented in the following.

This chapter includes also a short overview about gravity waves, the mean circulation, and the polar vortex during winter.

2.1 Wind approximations

Several approximations of actual wind exist. They are derived as balanced states resulting from an equilibrium of forces. Depending on the forces, that are taken into account, different approximations are regarded. For a system whose horizontal extent is much bigger than its vertical, like Earth's atmosphere is, the gravitational force is negligible for various studies. Forces under consideration are the pressure gradient force, the Coriolis force, and centripetal force, friction. The following discussion is restrained to a qualitative description. A mathematical treatment is found in *Holton (1992)*.

2.1.1 Geostrophic wind

The geostrophic approximation assumes straight isobars. Therefore it takes only pressure gradient force and Coriolis force into account. The air, which is in motion to balance the pressure gradient, is deflected due to the Coriolis force. Since both forces are in equilibrium the resultant geostrophic wind moves parallel to the isobars. Therefore, it not balances the pressure gradient.

The geostrophic approximation is a valuable approximation for the free atmosphere and explains jet streams. But it neglects friction, both between air and ground and between different air masses. Friction would reduce the flow and hence weaken the Coriolis force, leading to a predominance of the gradient force and hence to a flow from high pressure to low pressure. This is then called ageostrophic wind.

2.1.2 Gradient wind

The gradient wind is an extension of the geostrophic wind since it incorporates curvature of isobars. This means that a third force has to be taken into account: the centripetal force. The balance of three forces results again in a wind blowing parallel to the isobars, which not balances the pressure gradient.

When the curved isobars encircle a low pressure area, the centripetal force acts against the pressure gradient force. Hence, the gradient wind is weaker than the geostrophic wind. In case of a high pressure area the centripetal force acts in the same direction as the pressure gradient force. Therefore, the gradient wind is stronger than the geostrophic wind.

2.1.3 Thermal wind

In the previous sections temperature was ignored. We now assume a horizontal temperature gradient, additionally to the horizontal pressure gradient. The temperature gradient causes an altitude dependency of the tilting angle of isobaric surfaces: Over a warm region the thickness of the layer between two isobaric surfaces is larger than over a cold region.

If the temperature gradient is parallel to the pressure gradient, the slope of isobaric surfaces increases with altitude in the case of a warm high pressure area and a cold low pressure area, or decreases and might invert in case of a cold high and a warm low. In the former case the geostrophic wind increases with altitude, in the latter case the geostrophic wind decreases with altitude and might even invert.

If the temperature gradient is not parallel to the pressure gradient, then the geostrophic wind will rotate with altitude, and either increase or decrease. In the case of cold-air advection the geostrophic wind will rotate counterclockwise with altitude and increase. Contrary, in the case of warm-air advection the geostrophic wind will rotate clockwise with altitude and decrease.

The thermal wind is actually not a wind, but rather a vertical shear of the geostrophic wind. It explains the enhancement of jet streams at certain altitudes. The thermal wind relation allows estimating the geostrophic wind at different pressure levels, provided that the temperature field is known and the geostrophic wind at a certain start level.

2.2 Gravity Waves

Perturbations of the steady state of the atmosphere which show some periodic behavior are denoted as atmospheric waves. Examples are tides, which are generated primarily by periodic heating due to solar irradiation; planetary waves (also referred to as Rossby waves) as meanders of the circumpolar jet streams; and gravity (or buoyancy) waves, whose restoring force is gravity/buoyancy. We will focus on the latter ones. An extensive review of the dynamics of gravity waves is provided by *Fritts and Alexander (2003)*.

As mentioned above, waves appear in observation data as periodic perturbations of the background state. They might be recognized in single altitude profiles of temperature or wind speed, but more information about their characteristics is revealed in time-height sections. Maxima (or minima) that descend with time indicate upward propagating waves. The vertical direction of propagation can be determined from an arbitrary physical quantity that is affected by the wave (e.g., temperature or wind). Contrary, to determine the horizontal direction of propagation zonal and meridional wind need to be known. Since the wave is advected by the background wind, an instrument at a fixed location does not observe the actual, intrinsic, wave parameters. The intrinsic frequency $\hat{\omega}$ and the observed frequency ω of a wave are related by

$$\hat{\omega} = \omega - k\bar{u} - l\bar{v}, \quad (2.1)$$

where k and l are the zonal and meridional wave number, and \bar{u} and \bar{v} are the background zonal and meridional wind, respectively. The intrinsic frequency of a wave is coupled to its spatial characteristics and the atmospheric background via the dispersion relation:

$$\hat{\omega}^2 = \frac{N^2(k^2 + l^2) + f^2 \left(m^2 + \frac{1}{4H^2}\right)}{k^2 + l^2 + m^2 + \frac{1}{4H^2}}, \quad (2.2a)$$

$$m^2 = \frac{(k^2 + l^2)(N^2 - \hat{\omega}^2)}{\hat{\omega}^2 - f^2} - \frac{1}{4H^2}. \quad (2.2b)$$

Here N is the buoyancy frequency (see below), f is the Coriolis parameter ($f = 2\Omega \sin \phi$, with angular speed of Earth's rotation Ω and ϕ as latitude of observation), m denotes the vertical wave number, and H the pressure scale height. From the dispersion relation follows the range of the intrinsic frequency: $N > \hat{\omega} > f$. This thesis will briefly touch low-frequency waves with $\hat{\omega} \sim f$. These waves, also referred to as inertia-gravity waves, have such large horizontal wavelengths that their characteristics are affected by the Coriolis effect.

The buoyancy frequency (also referred to as Brunt-Väisälä frequency) describes the stability of the background atmosphere, it is defined as:

$$N^2 = g \frac{\partial \ln \theta}{\partial z} = \frac{g}{T} \left(\frac{\partial T}{\partial z} + \frac{g}{c_p} \right), \quad (2.3)$$

with g as gravitational acceleration, θ as potential temperature, T as temperature, and c_p as specific heat capacity at constant pressure.

Gravity waves are filtered at so-called critical levels. These are defined by the background wind speed \bar{u}_h in the direction of wave propagation. When \bar{u}_h approaches the horizontal phase speed c_h , the intrinsic phase speed $\hat{c}_h = c_h - \bar{u}_h$ and the vertical wavelength vanish. The actual critical level for inertia-gravity waves follows from the simplified dispersion relation

$$\hat{\omega}^2 = \frac{N^2(k^2 + l^2)}{m^2} + f^2 \quad (2.4)$$

as the altitude where the intrinsic frequency $\hat{\omega}$ approaches the Coriolis parameter f (since $m \rightarrow \infty$), which is lower than the level where $\bar{u}_h(z)$ approaches c_h (*Fritts and Alexander, 2003*).

When the amplitude of a wave grows too large the wave becomes unstable and finally breaks. The energy and momentum of the wave are then transferred to the background atmosphere. If, e.g., a wave with westward phase speed breaks, it deposits westward momentum which in turn leads to a westward acceleration. Therefore, waves influence the background flow as they transport energy and momentum between different altitudes.

2.3 Mean circulation

The following description is compiled from *Geller (1983)*; *Holton (1992)*; *Meriwether and Gerrard (2004)*.

First, we consider only the vertical temperature structure, no latitudinal (i.e., seasonal) dependencies. Temperature in the troposphere is primarily determined by solar heating of Earth's surface. Hence, temperature is highest over ground and decreases with altitude. In the stratosphere ultraviolet radiation from the Sun is absorbed by ozone. This results

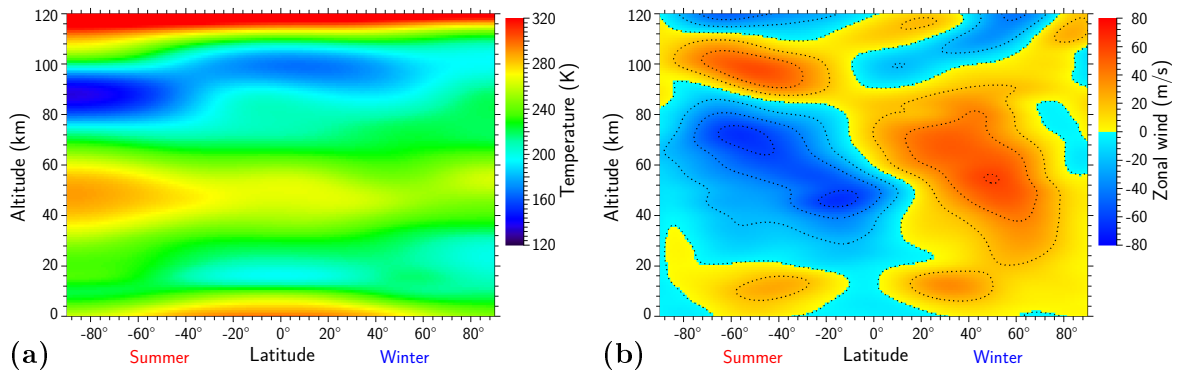


Figure 2.1 Latitude-height sections of zonal mean temperature (a) and zonal mean zonal wind (b) for 1 January. The temperature data are extracted from the NRLMSISE-00 reference atmosphere (Picone *et al.*, 2002). The wind speed data are extracted from the HWM07 model (Drob *et al.*, 2008).

in a temperature maximum at around 50 km altitude. In the mesosphere the temperature decreases, since there is no heating due to absorption. But in the thermosphere absorption by oxygen causes again an increase of temperature.

From the radiation balance we would expect the entire summer hemisphere to be warmer than the winter hemisphere. This is not the case, e.g., the summer mesopause is colder than the winter mesopause (cf. Fig. 1.1 and Fig. 2.1(a)). From the radiation balance we would also expect that the jet streams increase with altitude and are not closed. This is also not the case: The summer jet is closed at about 90 km altitude and the winter jet is closed at about 100 km (see Fig. 2.1(b)). Hence, there must be an additional forcing, which decelerates the jet streams at these altitudes and also explains the cold summer mesopause and the relatively warm winter stratopause.

Such additional forcing is induced by breaking gravity waves in the respective altitude. These waves are generated in the troposphere and propagate upward, they transport energy and momentum. As discussed above, they are either filtered at critical levels or propagate further upward until they break. During winter the zonal wind is eastward, hence only westward propagating waves are not filtered by zonal wind. These westward waves propagate upward until their amplitudes have grown so much that they break in the upper mesosphere. There they deposit their westward momentum. Due to the Coriolis force, the westward acceleration results in a meridional wind toward the winter pole. In a similar manner during summer only eastward propagating waves are able to propagate into the mesosphere, break there and deposit eastward momentum. This eastward acceleration is deflected toward the equator. Therefore, a meridional flow is established, from the summer pole, crossing the equator, toward the winter pole. Due to continuity of mass, this meridional flow causes sinking air above the winter pole and rising air above the summer pole. The sinking air over the winter pole adiabatically warms, causing the relatively warm polar winter stratopause. The rising air over the summer pole adiabatically cools, causing the cold polar summer mesopause. As a consequence of the thermal wind balance, the stratospheric jets in both hemispheres decrease and even change sign.

2.4 Polar vortex and sudden stratospheric warmings

As discussed above, a strong eastward jet exists in the winter stratosphere and mesosphere at polar latitudes at about 70° . This jet is referred to as polar vortex jet (or polar night jet). It spans the altitude range between about 20 and 90 km, highest wind speeds occur around the stratopause. The polar vortex is not pinned to a fix location. During winter it might take a more elliptic shape or its center might move southward.

The high wind speeds of the vortex isolate the air inside the vortex from air masses of lower latitudes. Due to the sinking of air inside the vortex the upper stratosphere is warmer than at lower latitudes, while the lower stratosphere is colder inside the vortex.

The vortex jet is a region of enhanced wave activity compared to regions inside or outside the vortex. This is explained by less filtering at critical levels due to the strong eastward winds and less wave saturation (*Meriwether and Gerrard, 2004*).

Due to the interaction of planetary waves it might happen, that the polar vortex gets displaced, deformed, or even split. This might result in an event which is referred to as sudden stratospheric warming (SSW). These events are characterized by strong increase of stratopause temperature by up to 50 K within a few days. SSW are classified by the World Meteorological Organization into “minor” and “major” warmings, both on a zonal-mean view: A minor warming is defined by a positive zonal mean temperature gradient on the 10 hPa pressure level between 60° and 90° latitude. A major warming is defined additionally by negative zonal mean zonal wind on the 10 hPa pressure level at 60° latitude (*Labitzke, 1981*). The typical temporal evolution of an SSW was described by *Labitzke (1972)*.

A leading contribution to the understanding of SSW was given by *Matsuno (1971)*. The basic idea is, that planetary waves, which are generated by orography, propagate upward until they are filtered at a critical level. There they decelerate the eastward polar vortex and heat the polar air just below the critical level. The eastward jet might even reverse to westward winds. Due to the deceleration of the eastward jet the critical level shifts downward, accompanied by lowering of the altitude of wind reversal and warming.

Chapter 3 Measuring wind in the middle atmosphere

As discussed above, wind measurements are essential for a comprehensive understanding of atmospheric dynamics. Unfortunately, wind measurements are difficult in a large part of the middle atmosphere. The absence of free electrons prevent radar measurements between about 20 and 60 km altitude, the so-called radar gap. Wind measurements are possible in this altitude range by meteorological rockets and balloons. However, these instruments provide only sporadic snapshots. The lidar technique covers the complete middle atmosphere and allows simultaneous measurements of atmospheric temperatures and wind speeds with reasonable temporal and vertical resolution on a routine basis.

This chapter first addresses the lidar principle in general and examines different scattering mechanisms and the Doppler effect, and afterward discusses various approaches to measure winds by lidar. The second part gives an overview of various other techniques to measure winds in the middle atmosphere. According to the respective measurement principle all of them have their advantages and drawbacks, they cover different altitude ranges and differ regarding their temporal resolutions and sounding volumes.

3.1 Lidar

3.1.1 Principle

The term “lidar” is actually an acronym for “light detection and ranging”, hence describes a measurement method. In general linguistic usage “lidar” is also used for an instrument which applies this method. Since this thesis deals with atmospheric physics it will focus on lidars for remote sensing of atmospheric properties.

A lidar is an, in most cases ground-based, active remote sensing instrument. Short pulses of light are emitted into the atmosphere where the light is scattered by air molecules, aerosols (e.g., clouds and dust particles), and metal atoms (see Sect. 3.1.2 for different scattering mechanisms). Some part of the backscattered light is collected by receiving telescopes and detected by photo detectors. The time lapse between emission and detection corresponds to the range at which the light was scattered. Without regard of instrumental properties, the amount of detected backscattered light gives information on the volume backscatter coefficient of the target, hence the product of its scattering cross-section and number density. Assuming a constant scattering cross-section throughout the sounding volume, the volume backscatter coefficient is proportional to the density of the scattering particles. So, taking the range dependent quadratic decrease of received backscattered light into account, the backscatter profile can be transformed directly into a profile of atmospheric density. Under some assumptions, a temperature profile can be derived from the density profile (*Kent and*

Wright, 1970; Hauchecorne and Chanin, 1980). Hence, it is possible to derive two important atmospheric parameters with fair effort. Even more sophisticated studies (e.g., probing aerosols, measuring wind speeds) can be done by analyzing the spectrum of the backscattered light, its polarization or backscattering at different wavelengths. Therefore, the lidar technique in general is quite versatile.

3.1.2 Scattering mechanisms

In Earth's atmosphere different light scattering mechanisms occur, which can be used for lidar soundings. Most important scattering mechanisms are elastic scattering from aerosols, elastic and inelastic scattering from air molecules, and fluorescence.

Elastic scattering at particles larger than 1 nm (aerosols) is called aerosol scattering. For spherical particles the process is called **Mie scattering**; this term is sometimes applied also for scattering at aspherical particles (e.g., *Mishchenko et al., 1999*). The scattering cross-section of aerosol particles depends strongly on their size and shape; for spherical particles with a radius of 50 nm the backscatter cross-section is $\sim 10^{-19} \text{ m}^2/\text{sr}$ (*Baumgarten, 2001*). Aerosol scattering is important in the troposphere, in the presence of stratospheric aerosol layers, and for noctilucent clouds in the upper mesosphere.

The notation of scattering processes occurring from air molecules is not straightforward. In a review article *Young (1981)* summarizes, that “molecular scattering consists of Rayleigh scattering and vibrational Raman scattering” and “**Rayleigh scattering** consists of rotational Raman lines and the central Cabannes line”. The **Cabannes line** results from elastic scattering without energy transfer. The **rotational Raman scattering** causes only small energy differences, i.e., the wavelength of the photon is shifted only slightly: $\Delta\lambda = 0.34 \text{ nm}$ for $\lambda_0 = 532 \text{ nm}$, for scattering on N_2 ($\Delta j = 2$) (*Rasetti, 1929*). If the vibrational state of the molecule is affected, the process is called **vibrational Raman scattering**. The wavelength shift is larger than for rotational Raman scattering: $\Delta\lambda = 75.8 \text{ nm}$ for $\lambda_0 = 532 \text{ nm}$, for scattering on N_2 ($\Delta\nu = 1$) (*Rasetti, 1929*). The scattering cross-section for Raman scattering on N_2 is on the order of $10^{-35} \text{ m}^2/\text{sr}$ (*Hyatt et al., 1973*). At a wavelength of 532 nm the Rayleigh scattering cross-section for air is $\sim 10^{-31} \text{ m}^2$ (*Bates, 1984*). Due to the exponential decrease of air density with altitude, the amount of light backscattered by air molecules decreases rapidly. Hence, depending on the sensitivity and power of a lidar system, molecular scattering cannot be used at altitudes above about 90 km.

Between about 80 and 110 km altitude a layer with relatively high number densities of metal atoms exists (e.g., for Na $\sim 1000 \text{ atoms per cm}^3$ (*Fricke and von Zahn, 1985*)). Using light of an appropriate wavelength, **resonance fluorescence** can be excited at these metal atoms. The scattering cross-section for this process is quite high, namely $\sim 10^{-15} \text{ m}^2$ (*Fricke and von Zahn, 1985*). So even the low absolute number density (compared to $\sim 10^{13}$ air molecules per cm^3) yields a much higher backscatter signal than molecular scattering.

The lidar used for this thesis resolves molecular and aerosol scattering, hence Rayleigh, Mie, and Raman scattering, explaining its name RMR lidar (Rayleigh/Mie/Raman). Table 3.1 summarizes some characteristics of these scattering mechanisms. In fact, only the Cabannes line is used for the wind and temperature measurements presented in this thesis.

Table 3.1 Scattering mechanisms used by the ALOMAR RMR lidar with respective scattering cross-section and wavelength shift for $\lambda_0 = 532$ nm, which is the wavelength used for the wind retrieval.

| name | scatterer | σ (m ² /sr) | $\Delta\lambda$ (nm) | reference |
|--------------------------|---------------|-------------------------------|------------------------|------------------------------|
| Rayleigh (Cabannes line) | air molecules | 10^{-32} | 0 | <i>Bates (1984)</i> |
| rotational Raman | air molecules | 10^{-35} (N ₂) | 0.34 (N ₂) | <i>Hyatt et al. (1973)</i> , |
| vibrational Raman | air molecules | | 75.8 (N ₂) | <i>Rasetti (1929)</i> |
| “Aerosol” (Mie) | aerosols | 10^{-19} ($r = 50$ nm) | 0 | <i>Baumgarten (2001)</i> |

3.1.3 Doppler effect

Various applications of the Doppler effect exist. This thesis deals with the Doppler effect occurring when light is scattered on moving air particles. This implies two basic conditions: First, the velocity of the particles is much smaller than the speed of light; and second, since light propagates independent of a medium (compared to sound propagating in air), only relative movements are important (but not absolute movements).

If source and observer of an electromagnetic wave (such as light) with a given frequency ν are at rest, consecutive wavefronts arrive the observer with the same time-lag as they leave the source. The time-lag Δt_{obs} is given by the wave’s phase velocity c and its wavelength λ :

$$\Delta t_{\text{obs}} = \frac{\lambda}{c}. \quad (3.1)$$

Now, assuming that the observer is moving away from the source with a velocity v , the time-lag between two consecutive wavefronts is somewhat larger, since the observer “runs away” from the next wavefront:

$$\Delta t_{\text{obs}} = \frac{\lambda}{c - v}. \quad (3.2)$$

Hence, the observed frequency ν_{obs} is slightly smaller than the emitted frequency ν_{src} :

$$\nu_{\text{obs}} = \frac{1}{\Delta t_{\text{obs}}} \quad (3.3a)$$

$$= \frac{(c - v) \cdot \nu_{\text{src}}}{c} \quad (3.3b)$$

$$= \nu_{\text{src}} \cdot \left(1 - \frac{v}{c}\right). \quad (3.3c)$$

Emitted and observed wavelength and frequency are related by

$$\frac{\lambda_{\text{obs}}}{\lambda_{\text{src}}} = \frac{\nu_{\text{src}}}{\nu_{\text{obs}}}, \quad (3.4)$$

yielding for the difference between observed and emitted wavelength:

$$\Delta\lambda = \lambda_{\text{obs}} - \lambda_{\text{src}} \quad (3.5a)$$

$$= \frac{c}{c - v} \cdot \lambda_{\text{src}} - \lambda_{\text{src}} \quad (3.5b)$$

$$= \frac{v}{c} \cdot \lambda_{\text{src}}. \quad (3.5c)$$

Chapter 3 Measuring wind in the middle atmosphere

In lidar application the Doppler effect occurs two times: when the light hits the scatterer (i.e., the moving air particle) and when the light leaves the scatterer. Therefore, the final equations for Doppler shift between detected and emitted light are:

$$\Delta\lambda = 2 \cdot \frac{v}{c} \cdot \lambda_{\text{src}} \quad (3.6a)$$

and

$$\Delta\nu = -2 \cdot \frac{v}{c} \cdot \nu_{\text{src}}. \quad (3.6b)$$

The Doppler effect has to be taken into account at two aspects: first, the random thermal motion of air particles; and second, the mean motion of an ensemble of air particles, known as wind.

Thermal motion

Independent of air motion, all molecules inside an air parcel are moving randomly. This is called thermal motion, which is described by the Maxwell-Boltzmann distribution. For lidar measurements only the motion along the line-of-sight is of interest. Hence, the one-dimensional Maxwell-Boltzmann distribution is sufficient:

$$p(v) \propto \exp\left(-\frac{m}{2k_{\text{B}}T}v^2\right), \quad (3.7)$$

with m as the scatterer's mass, atmospheric temperature T , and Boltzmann constant k_{B} . Taking the Doppler effect into account (Eq. (3.6a)), this velocity distribution leads to a wavelength distribution of the backscattered light:

$$p(\lambda) \propto \exp\left(-\frac{m}{2k_{\text{B}}T} \frac{(\lambda - \lambda_0)^2}{4\lambda_0^2} c^2\right). \quad (3.8)$$

For N_2 molecules ($m = 4.651 \cdot 10^{-26}$ kg) the thermal broadening is on the order of 10^{-3} nm. For example, $T = 250$ K yields with

$$\sigma_\lambda = \frac{2\lambda_0}{c} \sqrt{\frac{k_{\text{B}}T}{m}} \quad (3.9a)$$

and

$$\delta\lambda = 2\sqrt{2\ln 2} \cdot \sigma_\lambda \quad (3.9b)$$

a standard deviation σ_λ of about $0.7 \cdot 10^{-3}$ nm and a full width at half maximum $\delta\lambda$ of about $1.6 \cdot 10^{-3}$ nm.

Since the thermal broadening is caused by Doppler shift, it is also referred to as Doppler broadening.

Wind

For emitted frequency of $\nu_0 = 532$ nm the Doppler shift due to wind is on the order of 10^{-5} nm. Hence, the relative Doppler shift $\frac{\Delta\nu}{\nu_0}$ is on the order of 10^{-8} only. For example, Eq. (3.6a) yields for a line-of-sight wind speed of 10 m/s a Doppler shift of about $3.5 \cdot 10^{-5}$ nm. This is four orders of magnitude smaller than the wavelength shift due to rotational Raman scattering. Hence, both can be clearly distinguished. On the other hand, the Doppler shift is two orders of magnitude smaller than the Doppler broadening.

3.1.4 Different techniques to derive wind by lidar

The measurement of wind speed by lidar relies on determining the frequency shift caused by the Doppler effect when light is scattered on moving particles. Different approaches exist to measure the frequency shift. The following summary is inspired by the project proposal for the Doppler capability of the ALOMAR RMR lidar (*Baumgarten, 2005*).

Heterodyne detection technique

When light of two slightly different frequencies is superposed, interference yields a beat whose frequency equals the difference of the initial frequencies. Superposing part of the emitted light and the (Doppler shifted) backscattered light allows then determining the Doppler shift by measuring the periodic variation of the intensity of the superposed light. This technique is also referred to as coherent technique since coherence of the phase of the backscattered light in the scattering volume is required.

The coherence of the phase is disturbed by atmospheric inhomogeneities. The size of this disturbance depends on the wavelength and on the size of the telescopes: Large wavelengths (i.e., infrared light) and small telescopes are preferable. Since the Rayleigh scattering cross-section is inverse proportional to the fourth power of the wavelength ($\sigma \propto \lambda^{-4}$), Rayleigh scattering of infrared light is quite weak. Hence, this method relies on aerosol scattering and is therefore limited to atmosphere regions that contain reasonable amounts of aerosols, i.e., the troposphere.

Direct detection techniques

A different approach is to measure the frequency shift directly. Two techniques are widely established: Measuring the interference pattern behind a Fabry-Pérot interferometer (fringe imaging technique) or using steep frequency filters to transform frequency changes into intensity variations (edge technique). Direct detection techniques are also known as incoherent techniques since single backscattered photons from the sounding volume are used, independent of their individual phases.

Fringe imaging technique A Fabry-Pérot interferometer (FPI) consists of two parallel highly reflecting surfaces. If light is coupled into an FPI perpendicular to these surfaces, some small portion of the light is transmitted directly, other portions are reflected multiple times between the surfaces before they are also transmitted. Portions of the transmitted light might or might not be in phase. This results in a circular interference pattern behind the FPI, referred to as fringes. For a given FPI the actual shape of these fringes depends on the frequency of the incident light. Hence, analyzing variations of the interference pattern allows to determine frequency shifts. This technique has been applied by, e.g., *Tepley (1994)* and *Rees et al. (1996)*. It requires sophisticated effort concerning the alignment and is sensitive to thermal drifts (e.g., *Friedman et al., 1997*).

Edge technique The edge technique uses filters whose transmittance depends on the frequency of the incident light to convert a frequency shift into an intensity variation behind the filters. Steep filters can be achieved, e.g., with Fabry-Pérot interferometers or with molecular absorption filters. While tunable FPIs allow to vary their filter characteristics, they require sophisticated effort concerning their alignment. Molecular absorption filters are restricted to selected lines of their absorption spectrum, but are more stable and easier to handle.

Chapter 3 Measuring wind in the middle atmosphere

The intensity variation behind the filter depends not only on the frequency of the incident light, but also on its spectral width. For Rayleigh scattering the spectral width depends on atmospheric temperature (see Sect. 3.1.3). Hence, atmospheric temperature must be measured simultaneously. The edge technique can be realized with one or two filters.

The **double edge technique** applies two filters with opposed filter characteristics. A frequency shift causes increased intensity behind one filter and decreased intensity behind the other one. This technique requires two channels for the wind measurement and a third one to measure atmospheric temperature and aerosols. This method was applied by, e.g., *Chanin et al.* (1989) and *Garnier and Chanin* (1992) using Fabry-Pérot interferometers.

For the **single edge technique** only one filter with a steep edge is used. Hence, only two channels are required: One to measure the Doppler shift, the other one to take atmospheric transmission into account and for temperature and aerosol measurements. This yields higher signal and consequently less measurement uncertainty. This technique was described by *Korb et al.* (1992) and applied by, e.g., *Friedman et al.* (1997) using a molecular absorption filter. It is implemented in the ALOMAR RMR lidar (*Baumgarten, 2010*), more details are presented in Sect. 4.1.

To summarize, the single edge technique allows simultaneous wind and temperature measurements in the middle atmosphere with only two detection channels. Molecular absorption filters are relatively easy to handle and provide very high spectral stability. This allows to lock the frequency of the emitted light to the same molecular absorption line as the detection system. These qualities make this technique preferable.

Wind retrieval of metal resonance lidars

Metal resonance lidars excite atoms of the according metal to fluorescence. Only atoms for which the frequency of the incident light matches the frequency of the fluorescence transition get excited and reemit a photon. Since single atoms are not at rest, but moving due to thermal motion and atmospheric wind, the frequency of the incident light is affected by Doppler shift (differently for each single atom). For an ensemble of atoms the scattering cross-section is then a function of temperature, line-of-sight wind speed, and emitted frequency (*Fricke and von Zahn, 1985*). Comparing the lidar return signal at at least three different emission frequencies yields then atmospheric temperatures and wind speeds within the metal layer. A detailed description of this method is presented, e.g., in *Kaifler* (2009).

Table 3.2 lists lidar systems that are capable to measure wind speeds in the middle atmosphere.

3.2 Other techniques to measure winds in the middle atmosphere

3.2.1 Meteorological rockets

Sounding rockets are mainly used to transport scientific instruments for in-situ measurements to high altitudes. Smaller kinds of sounding rockets are called meteorological rockets. These rockets release an object at a certain altitude which is then tracked by radar to derive its position (the object simply acts as a radar target). Typical targets are clouds of thin metalized foil snippets (called chaff), metalized inflatable spheres (called falling spheres), metalized

3.2 Other techniques to measure winds in the middle atmosphere

Table 3.2 Middle atmosphere wind lidars with respective altitude coverage. Simultaneously measured atmospheric quantities are denoted (T : temperature, ρ_{Na} : sodium density).

| lidar | altitude range (km) | combination with | reference |
|--|---------------------|-----------------------|----------------------------------|
| OHP ^a Rayleigh lidar (44° N) | 25–50 | — | <i>Chanin et al. (1989)</i> |
| CEL ^b Rayleigh lidar (44° N) | 25–50 | — | <i>Garnier and Chanin (1992)</i> |
| Arecibo Rayleigh lidar (18° N) | 10–60 | — | <i>Tepley (1994)</i> |
| Arecibo Rayleigh lidar (18° N) | 18–45 | — | <i>Friedman et al. (1997)</i> |
| OHP ^a Rayleigh-Mie lidar (44° N) | 8–50 | — | <i>Souprayen et al. (1999)</i> |
| ALOMAR Na lidar (69° N) | 80–110 | T, ρ_{Na} | <i>She et al. (2002)</i> |
| SOR ^c Na lidar (35° N) | 80–105 | T, ρ_{Na} | <i>Liu et al. (2002)</i> |
| UIUC ^d Na lidar on Maui (21° N) | 80–100 | T, ρ_{Na} | <i>Franke et al. (2005)</i> |
| CSU ^e Na lidar (41° N) | 80–105 | T, ρ_{Na} | <i>Yuan et al. (2009)</i> |
| extension to CSU ^e Na lidar (41° N) | 10–45 | T | <i>Huang et al. (2009)</i> |
| Rayleigh lidar at Hachijōji (37° N) | 8–25 | — | <i>Shibata et al. (2009)</i> |
| ALOMAR RMR lidar (69° N) | 30–80 | $T, \text{aerosols}$ | <i>Baumgarten (2010)</i> |
| USTC ^f Rayleigh lidar (42° N ^g) | 8–40 | — | <i>Xia et al. (2012)</i> |

^a Observatory of Haute Provence

^b Centre d'Essais des Landes

^c Starfire Optical Range

^d University of Illinois at Urbana-Champaign

^e Colorado State University

^f University of Science and Technology of China

^g this lidar is mobile

parachutes or starutes¹ (e.g., *Widdel, 1990; Schmidlin et al., 1991; Olsen and Kennedy, 1974*). Taking the mass and shape of the radar target into account allows to derive wind speeds from the (horizontal) motion of the object while it (slowly) descends. Additionally, it is possible to derive atmospheric density (and resultant atmospheric temperature) from the descent rate. Parachutes and starutes may be equipped with thermistors to measure temperatures directly (e.g., *Keckhut et al., 1999*).

The maximum altitude is limited by too high descend rates due to low air density. The lowest altitude for chaff is given by dissolving of the foil cloud (caused by air turbulences). For falling spheres the lowest altitude is defined by air pressures high enough to let the sphere collapse. This results in an altitude coverage of approximately 70–105 km for chaff (*Widdel, 1987, 1990*), about 35–90 km for falling spheres (e.g., *Lübken and Müllemann, 2003; Müllemann and Lübken, 2005*), and approximately 20–70 km for starutes (*Schmidlin et al., 1991*).

3.2.2 Balloons

In a similar way it is possible to derive wind speeds from the horizontal motion of an ascending or drifting balloon. The position of the balloon is either determined by tracking the balloon by radar or the balloon is equipped with tracking techniques (e.g., a GPS² receiver) and submits its position by telemetry. Balloons carrying radiosondes are launched worldwide on a routine basis to provide information for weather forecasts. These balloons reach top altitudes of about 20–30 km (e.g., *Seidel et al., 2001*). Bigger high-altitude balloons carrying complex scientific instruments can reach altitudes of about 40 km (e.g. *Engel et al., 2009*).

¹ portmanteau of “stable parachute”

²Global Positioning System; a satellite navigation system

3.2.3 Radars

Different radar techniques exist, providing various approaches to derive wind speeds. Following *Hocking (1997)*, three main methods are applied: the Doppler method, the spaced-antenna method, and interferometric methods. The radar principle in general relies on the backscattering of the emitted radio wave at irregularities of refractive index. Distinct radar techniques differ in the way they deduce the movement of these irregularities.

For the **Doppler method** a narrow radar beam is pointed in one specified direction. The backscattered wave experiences a Doppler shift corresponding to the motion of the irregularities of refractive index. Measuring this Doppler shift yields line-of-sight wind speed. A three-dimensional wind field can be derived by pointing the beam to various directions. An exemplary instrument of this type which is operated by IAP is the Saura MF radar (*Singer et al., 2003b, 2007*), it is located 15 km south of ALOMAR. It covers the altitude range ≈ 50 –100 km with a vertical and temporal resolution of 1 km and 30 min, respectively.

The **spaced-antenna method** employs one transmitting antenna and at least three spatially separated receiving antennas. Using correlation techniques, a diffraction pattern on the ground (i.e., an image) of the scattering layer is derived from the backscattered signals from different antennas. From drift speed and drift direction of the ground level diffraction pattern the horizontal wind field at the scattering layer is deduced. An exemplary instrument of this type which is operated by IAP is the Andenes MF radar (*Singer et al., 1997*), it is located 2 km south of ALOMAR. Measurements cover the altitude range ≈ 50 –100 km with a vertical and temporal resolution of 2 km and 30 min, respectively.

The **interferometric method** is a combination of both previous techniques: Correlation of backscattered signal of spaced antennas is used to locate discrete scatterers. Then the Doppler shift for single scatterers is determined, yielding line-of-sight wind speed. Combining measurements from all scatterers within a given volume and time interval results in a three-dimensional wind field. Typical discrete scatterers are the ionized trails of meteors; these systems are then called meteor radars. An exemplary instrument of this type which is operated by IAP is the SKiYMET meteor radar Andenes (*Hocking et al., 2001; Singer et al., 2003a*), it is located 2 km south of ALOMAR. It covers the altitude range ≈ 80 –100 km with a vertical and temporal resolution of 2 km and 1 h, respectively.

3.2.4 Airglow observations

In the upper mesosphere and lower thermosphere certain chemical reactions, and relaxation and recombination processes cause emission of light at distinct wavelengths. Involved species are, e.g., molecular and atomic oxygen, hydroxyl, and sodium (e.g., *Meinel, 1950; Barth, 1961; Hecht, 2004*). Since these species are moving with atmospheric motion their emission lines are Doppler shifted. Hence, measuring the Doppler shift yields wind speeds.

With ground-based instruments the only altitude information is derived from assuming the layer of the respective species at a certain altitude. For instance, the ERWIN II³ instrument (*Kristoffersen et al., 2013*) measures the Doppler shift at three different wavelengths for three different species (OH, O₂, O(¹S)) that are layered at three different altitudes (87, 93, and 97 km).

Spaceborne instruments derive altitude information by sounding the atmosphere in limb-

³advanced E-Region Wind Interferometer

3.2 Other techniques to measure winds in the middle atmosphere

viewing geometry. Two instruments were flown from 1991 to 2005 on UARS⁴: HRDI⁵ (*Hays et al.*, 1993) and WINDII⁶ (*Shepherd et al.*, 1993). HRDI employed a triple Fabry-Pérot interferometer to measure the spectral shape of emission lines of O₂. WINDII used a Michelson interferometer to transform the Doppler shift into a phase shift. It observed emission lines of O₂, O(¹S), O(¹D), O⁺(²P), and OH.

The TIDI⁷ instrument (*Killeen et al.*, 2006) onboard the TIMED⁸ satellite started operation in 2002 and is still active. Similar to HRDI it employs a Fabry-Pérot interferometer to resolve the shape of emission lines of O₂ and OI.

3.2.5 Microwave radiometers

Another type of radiation from atmospheric constituents is microwave radiation. It originates from vibrational and rotational transitions in molecules, which are thermally excited. Due to the thermal excitation microwave radiation is not limited to certain layers like airglow, but emitted over the entire atmosphere. The line shape of light emitted in the troposphere and stratosphere is not only affected by thermal broadening but also by pressure broadening. This allows ground-based instruments to derive rough altitude information. Spaceborne instruments obtain altitude resolution by applying limb-view geometry.

Launched in 2004, MLS⁹ (*Wu et al.*, 2008) onboard the Aura satellite is still in operation. MLS was not designed to directly measure wind speeds, but it can resolve the Doppler shift of an O₂ emission line using a digital autocorrelation spectrometer. In the height range 70–92 km the altitude resolution is ~ 8 km.

The instrument SMILES¹⁰ (*Baron et al.*, 2013) was attached to the International Space Station for a campaign between autumn 2009 and spring 2010. It used two acousto-optical spectrometers to resolve the spectrum of emission lines of O₃ and H³⁵Cl. The vertical resolution is 5–10 km in the altitude range 35–80 km.

The ground-based radiometer WIRA¹¹ (*Rüfenacht et al.*, 2012) observes an emission line of O₃ and derives wind speed at five altitude levels between 30 and 79 km with a temporal resolution of one day.

Summary

All these techniques differ in basic parameters like altitude coverage, vertical, horizontal, and temporal resolution. Figure 3.1 depicts the altitude range covered by these techniques. Lidars and microwave radiometers are the only instruments that cover the stratosphere and mesosphere on routine basis. Table 3.3 lists the altitude range, and vertical and temporal resolution of exemplary instruments. The horizontal extent of sounding volumes differs for all these instruments remarkably, ranging from 5 km diameter at 85 km altitude for Saura MF radar and 5 km by 6 km at 90 km altitude for ERWIN II to 5–10 km by 500–700 km for SMILES.

Apart from these technical parameters the instruments differ in the way they contribute to a better understanding of Earth's atmosphere. In-situ measurements by rockets and bal-

⁴Upper Atmosphere Research Satellite

⁵High Resolution Doppler Imager

⁶WIND Imaging Interferometer

⁷TIMED Doppler Interferometer

⁸Thermosphere Ionosphere Mesosphere Energetics and Dynamics

⁹Microwave Limb Sounder

¹⁰Superconducting Submillimeter-Wave Limb-Emission Sounder

¹¹wind radiometer

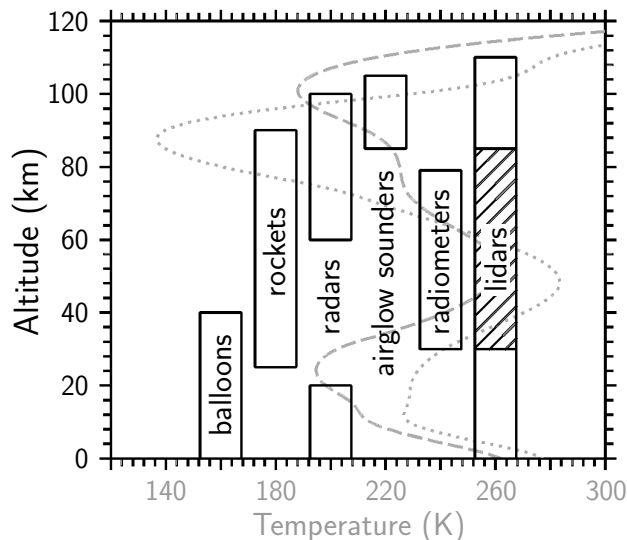


Figure 3.1 Altitude coverage of different wind measurement techniques for the middle atmosphere. The shaded part of the lidar column denotes the current altitude range of the wind capability of the ALOMAR RMR lidar. See text for details of respective techniques and exemplary instruments. Gray lines denote temperature profiles for summer (dotted) and winter (dashed).

Table 3.3 Remote sensing instruments for wind measurements in the middle atmosphere. Instruments are divided into radars, microwave radiometers, and airglow sounders. For spaceborne instruments the corresponding spacecraft is given in parentheses. See text for respective details. Lidar instruments are listed separately in Tab. 3.2.

| instrument | altitude range (km) | resolution | | reference |
|------------------|------------------------|------------|----------|------------------------------------|
| | | temporal | vertical | |
| Andenes MF radar | 50–100 | 30 min | 2 km | <i>Singer et al. (1997)</i> |
| Saura MF radar | 50–100 | 30 min | 1 km | <i>Singer et al. (2003b, 2007)</i> |
| SKiYMET radar | 80–100 | 1 h | 2 km | <i>Singer et al. (2003a)</i> |
| MLS (Aura) | 70–92 | — | ~ 8 km | <i>Wu et al. (2008)</i> |
| SMILES (ISS) | 35–80 | — | 5–10 km | <i>Baron et al. (2013)</i> |
| WIRA | 30–79 | 1 d | 8–15 km | <i>Rüfenacht et al. (2012)</i> |
| HRDI (UARS) | 10–110 | — | ~ 6 km | <i>Hays et al. (1993)</i> |
| WINDII (UARS) | 80–300 | — | ~ 2 km | <i>Shepherd et al. (1993)</i> |
| TIDI (TIMED) | 85–105 | — | ~ 2 km | <i>Killeen et al. (2006)</i> |
| ERWIN II | 87, 93, 97 | 3 min | ~ 5 km | <i>Kristoffersen et al. (2013)</i> |

loons have very high vertical and temporal resolution, but are launched only sporadically on a campaign basis. Satellite instruments deliver data on global scales, but with very limited spatial and temporal resolution. Ground-based instruments yield continuous data at distinct locations with fairly high temporal and vertical resolution. An integrated understanding of atmospheric processes is only possible by combining all of these different techniques.

3.2 Other techniques to measure winds in the middle atmosphere

The Rayleigh lidar technique is the only technique that is capable to measure wind speeds in the radar gap with a reasonable temporal and vertical resolution. In principle, observations are limited only by weather conditions. The WIRA instrument is not limited by such restrictions, but its low vertical and temporal resolution allows only the measurement of large-scale planetary waves. Gravity waves with periods of few hours and vertical wavelengths of few kilometers can only be resolved by lidar. Additionally, the lidar techniques (Rayleigh lidar and metal resonance lidar) allow simultaneous measurements of wind and temperature.

Chapter 4 The Doppler Rayleigh Iodine Spectrometer – instrumental setup and wind retrieval

This chapter gives a comprehensive overview of DORIS, the wind measurement capability of the ALOMAR RMR lidar. It starts with a description of the wind retrieval in a qualitative manner. Subsequently the instrumental setup of the lidar and particularly DORIS is presented. A detailed description of the wind retrieval follows, including calibration and performance monitoring.

4.1 Principle of DORIS

The principle of the Doppler Rayleigh Iodine Spectrometer (DORIS) relies on the Doppler effect (Sect. 3.1.3) and application of the single edge technique (Sect. 3.1.4). As frequency discriminator the steep edge of an absorption line of molecular iodine is used. The filter consists of a cell which is filled with iodine vapor. Its temperature and pressure are adjusted to ensure that all iodine is in the gas phase. The frequency of the emitted light is locked to the same absorption line; hence, emitter and detection system are tightly coupled to the same wavelength.

The spectral shape of the backscattered light is affected by atmospheric temperature, wind, and aerosols. To simplify the discussion we focus on the aerosol free atmosphere, i.e., Rayleigh scattering and the resultant Cabannes line. Figure 4.1 illustrates the effect of varying wind and temperature on the Cabannes line: Wind shifts the Cabannes line (panel (a)), while temperature broadens it (panel (b)). Both results in varying transmittance through the iodine cell. The wind effect is much bigger than the temperature effect, but since temperatures in the middle atmosphere range from 130 K in the upper summer mesosphere (*Lübken, 1999*) to more than 300 K during stratospheric warmings in winter (*von Zahn et al., 1998*) the temperature effect is not negligible. Hence, it is required to measure temperature simultaneously.

Figure 4.2 shows schematically the setup for the wind retrieval. The backscattered light is split into two parts. One part is detected directly, referred to as reference channel. The other one passes through an iodine-vapor cell before it is detected, referred to as Doppler channel. The reference channel is used to measure temperatures and aerosols, and to take signal variations (due to atmospheric transmission or varying laser power) into account when deriving the transmittance through the iodine cell. The signal ratio of Doppler channel and reference channel is referred to as Doppler ratio. It is a measure of wind speed and temperature. This is shown in Fig. 4.3. The green shaded area corresponds to the signal measured behind the iodine cell, whereas the signal of the reference channel corresponds to the complete area below the blue curve. The ratio of both signals is indicated by the red mark at the

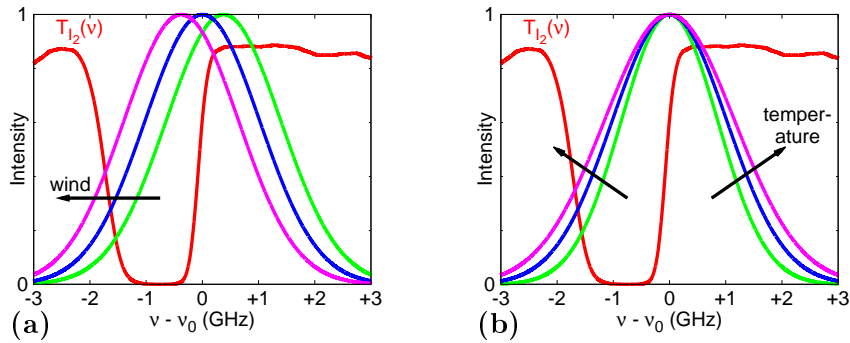


Figure 4.1 Effect of wind and temperature on the Cabannes line; the transmittance spectrum of the iodine-vapor cell is shown in red. **(a)** Constant temperature (250 K), variable wind speed (green: -100 m/s, blue: 0 m/s, magenta: $+100$ m/s); **(b)** constant wind (0 m/s), variable temperature (green: 175 K, blue: 250 K, magenta: 325 K). Black arrows indicate the effect of increasing wind speed or temperature, respectively.

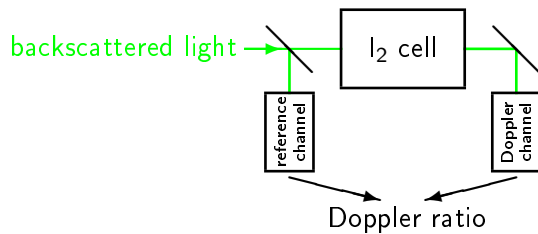


Figure 4.2 Sketch of the DORIS setup; see text for details.

right ordinate. Comparing panels (a) and (b), the negative Doppler shift of the Cabannes line causes a decrease of Doppler ratio. Comparing panels (a) and (c), the broadening of the Cabannes line causes a slight increase of Doppler ratio. Hence, the Doppler ratio depends on

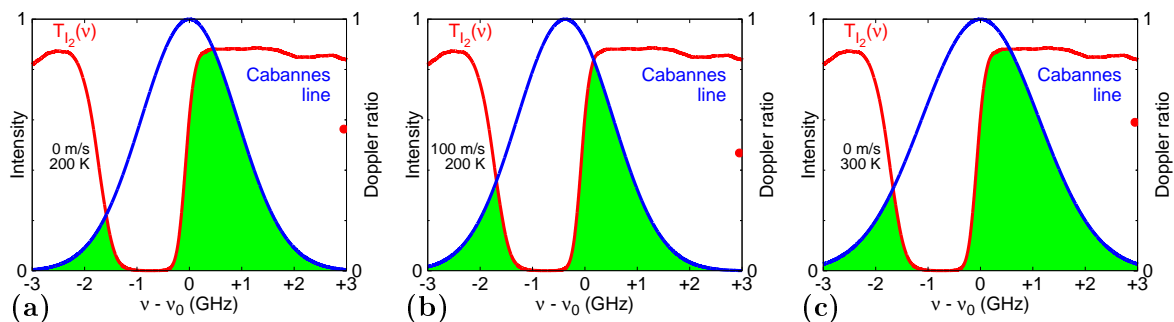


Figure 4.3 Effect of wind and temperature on Doppler signal and Doppler ratio. The green shaded area corresponds to the Doppler signal, while the whole area below the blue curve corresponds to the reference signal. The ratio of both is the Doppler ratio, indicated by the red mark at right ordinate. **(a)** zero wind, 200 K; **(b)** 100 m/s, 200 K; **(c)** zero wind, 300 K.

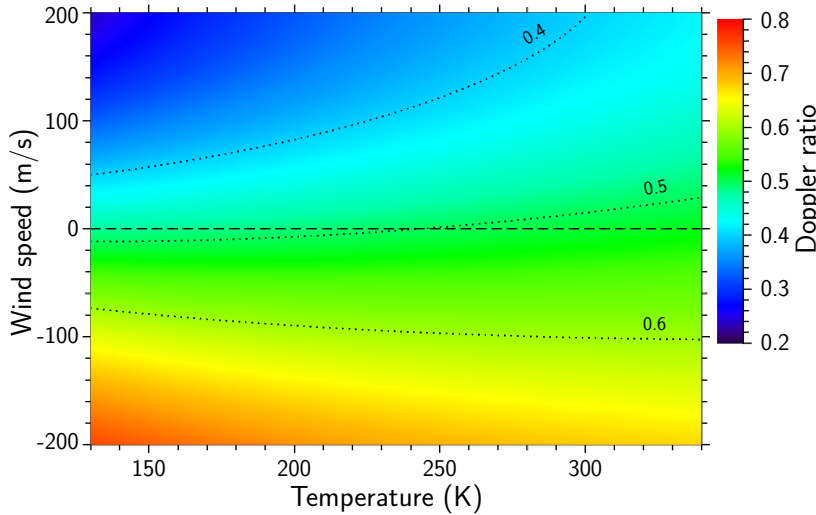


Figure 4.4 Modeled Doppler ratio as function of temperature and wind speed. Dotted lines indicate isolines for Doppler ratio of 0.4, 0.5, and 0.6. Dashed line is line for zero wind speed. This matrix was derived during a calibration measurement on 07.09.2010.

wind speed and temperature. This is also apparent in Fig. 4.4, which shows modeled Doppler ratio D_{model} for various combinations of wind $v_{\text{l.o.s.}}$ and temperature T . The shape of this modeled matrix is determined by the shape of the iodine absorption line. The wind speed response is much steeper than the temperature response: $\frac{\partial D_{\text{model}}}{\partial v_{\text{l.o.s.}}} = 1.0 \cdot 10^{-3} (\text{m/s})^{-1}$ and $\frac{\partial D_{\text{model}}}{\partial T} = 2.1 \cdot 10^{-4} \text{K}^{-1}$ for $v_{\text{l.o.s.}} = 0 \text{ m/s}$ and $T = 240 \text{ K}$. This yields a wind sensitivity on temperature of $\frac{\partial v_{\text{l.o.s.}}}{\partial T} = 0.21 \text{ m/s K}^{-1}$, which is smaller than the actual measurement uncertainty (see Sect. 4.3.2). If temperature is known, the Doppler ratio is a unique measure of wind speed. Hence, this matrix can be used as a lookup table to retrieve wind speed from measured Doppler ratio and temperature.

Although the acronym DORIS implies Rayleigh scattering at molecules, the same principle is applicable for scattering at aerosols. Due to their higher mass the thermal broadening of the backscattered light is much weaker. This results in steeper wind response and nearly no temperature response of the Doppler ratio. To calculate wind in the aerosol loaded atmosphere the amount of aerosol backscatter signal must be calculated before the wind retrieval.

4.2 Instrumental setup

The ALOMAR RMR lidar was designed to provide measurement capabilities for a wide range of tasks and parameters (*von Zahn et al.*, 2000). Additionally, due to its remote location in the Arctic, high reliability, large degree of automation, and opportunities for remote control are required. Hence, it is a quite complex instrument. Therefore, the following Sect. 4.2.1 describes only shortly the most important features, more detailed descriptions of the complete lidar or single sub-systems are presented in *Fiedler and von Cossart (1999)*; *von Zahn et al. (2000)*; *Fiedler et al. (2008)*; and *Baumgarten (2010)*. Main components for the DORIS setup are addressed in Sect. 4.2.2.

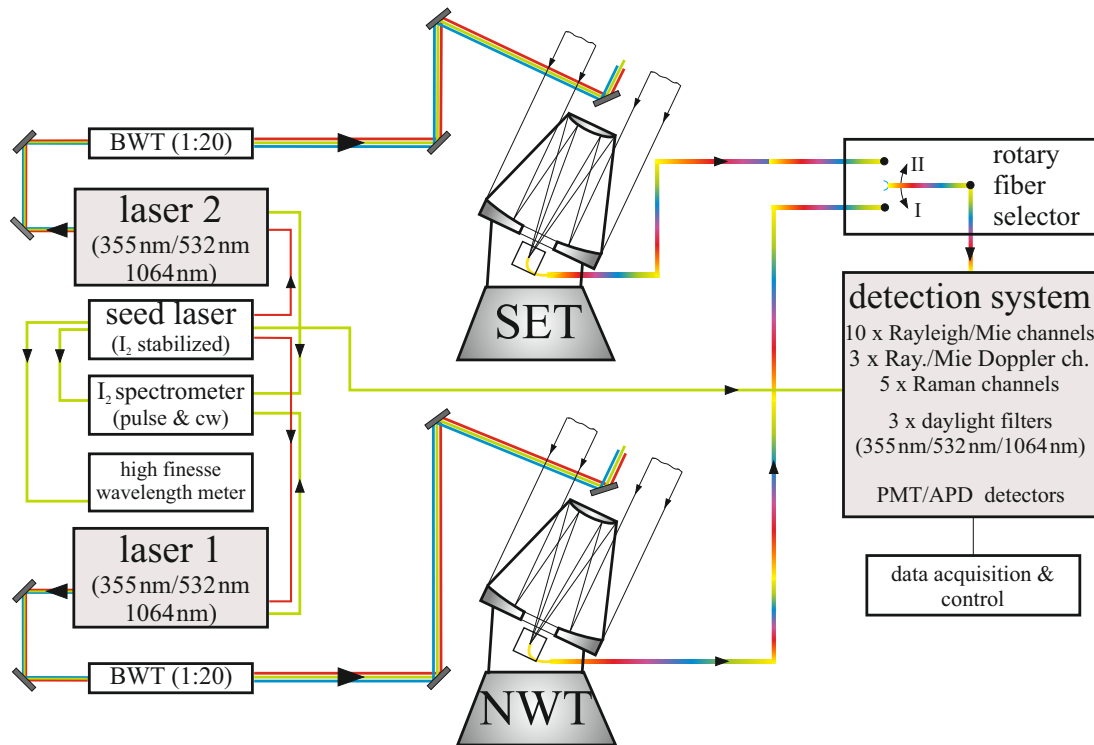


Figure 4.5 Schematic setup of the ALOMAR RMR lidar, see text for details.

4.2.1 The ALOMAR RMR lidar

The ALOMAR RMR lidar is a twin lidar: It employs two identical lasers to emit pulsed laser beams and two telescopes to receive the backscattered light, but only one single detection system to count the received photons. Figure 4.5 gives an overview of the whole system.

Both power lasers¹ are Nd:YAG² lasers, which are injection-seeded by one continuous wave seed laser³. The frequency of the seed laser is controlled by absorption spectroscopy (see Sect. 4.2.2 for details). Part of the 532 nm emission of the seed laser is guided to a commercial wavelength meter⁴, to an iodine spectrometer (LPS, see Sect. 4.5.2), and to the detection system. The power lasers emit light of three wavelengths simultaneously: the fundamental (1064 nm), the second harmonic (532 nm), and the third harmonic (355 nm). The emitted pulses are about 10 ns long. The energy per pulse is ~ 1.6 J (i.e., the peak power is ~ 160 MW); respective values for the 532 nm emission, which is used for DORIS, are ~ 0.5 J and ~ 50 MW (*von Cossart, 2013*). The pulse repetition rate is 30 Hz. To reduce the beam divergence the diameter of the beams is widened to 20 cm, the beam divergence is $\lesssim 70$ μ rad (*von Cossart, 2013*). Applying motorized beam guiding mirrors the laser beams are guided to the top of the receiving telescopes and emitted along their optical axes.

The receiving telescopes are of the Cassegrain design. The primary mirrors have a diameter of 1.8 m, the focal length is 8.3 m, the field of view is 180 μ rad. Both telescopes can be tilted to off-zenith angles of up to 30° and steered to different directions: The North-West Telescope

¹Quanta-Ray PRO-290-30, made by Spectra Physics

²Neodymium-doped yttrium aluminum garnet; Nd:Y₃Al₅O₁₂

³Prometheus 100NE, made by Innolight GmbH

⁴Wavelength Meter Angstrom WS Ultimate MC4, made by HighFinesse Laser and Electronic Systems

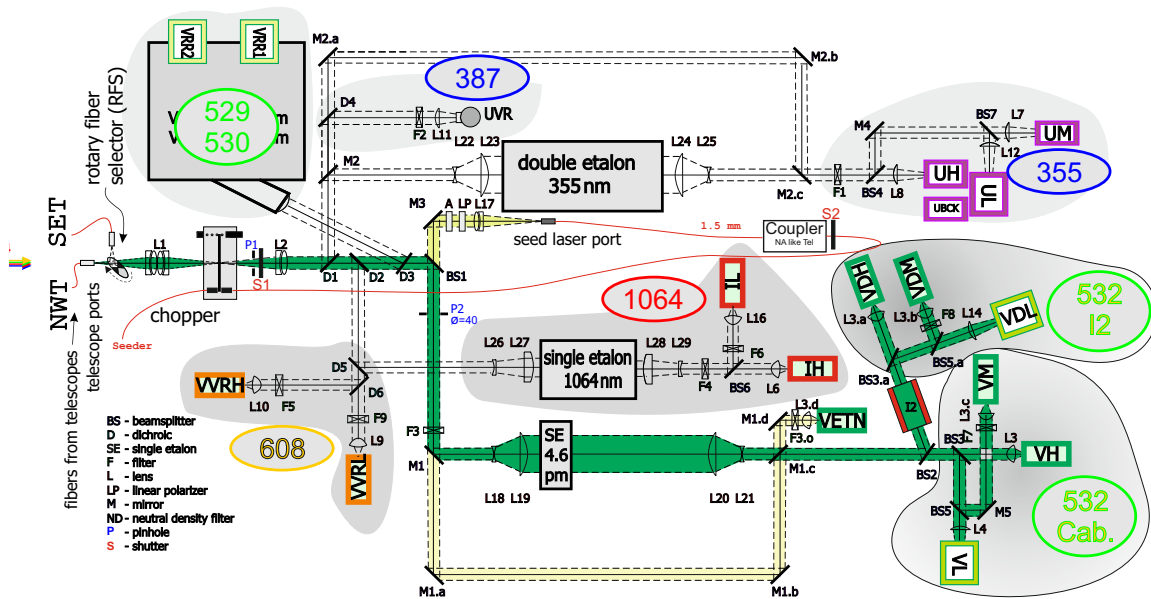


Figure 4.6 Scheme of the detection system of the ALOMAR RMR lidar. The green highlighted branch is the 532 nm branch used for DORIS. Numbers in ovals denote the accordingly detected wavelength (in nm). Rectangles with colored frames depict the detectors, the first letter denotes the spectral range (U: ultraviolet, V: visible, I: infrared), the last letter the sensitivity (L: low, M: medium, H: high); RR: rotational Raman, VR: vibrational Raman. See text for details.

(NWT) can be steered to the north-west quadrant, the South-East Telescope (SET) to the south-east quadrant. The focal optics contain a camera which takes an image of the laser beam in about 1 km altitude. This is used for a beam stabilization algorithm which controls the beam guiding mirrors to keep the laser beam in the center of the field of view of the telescope.

The received backscattered light is guided through optical fibers to the polychromatic detection system, which is shown schematically in Fig. 4.6. A segmented rotating mirror (rotary fiber selector, RFS) is used to feed light from both telescope ports alternately into the detection system. The light passes a chopper and is separated by wavelength into different channels using dichroic mirrors. The channels for elastic scattered ultraviolet (355 nm), infrared (1064 nm), and green (532 nm) light are equipped with Fabry-Pérot interferometers as daylight filters (these can be bypassed for the 355 nm and the 532 nm branch). Most of the channels consist of two or three detectors with different sensitivities, they are activated at different times after the laser pulse. This increases the dynamic range of the channel, hence the covered altitude range. In sum the detection system consists of 18 detectors to convert the backscattered photons into electric signals, photomultiplier tubes and more sensitive avalanche photodiodes. The 532 nm branch is also fed with light from the seed laser, this is

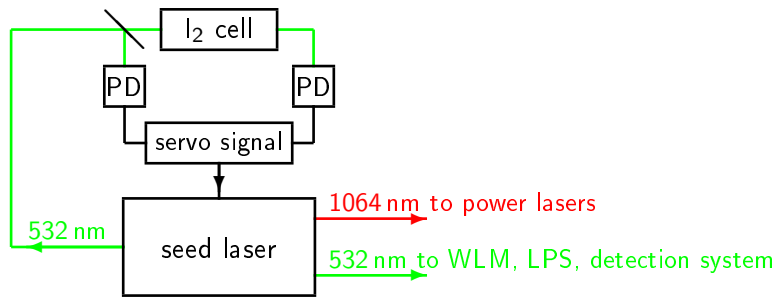


Figure 4.7 Scheme of the control loop for the seed laser frequency, see text for details.

controlled by the chopper. The aperture of the seed laser port is like that of the telescope ports. The temperature of the detection room is stabilized to avoid thermal expansions on the detection system which would affect its alignment.

Raw data for each laser/telescope are recorded with an internal integration of typically 1000 laser pulses (i.e., ≈ 33 s). The backscatter signal is sorted to range bins of 50 m.

4.2.2 DORIS setup

This section presents the instrumentation which is required especially for DORIS, the wind retrieval capability of the ALOMAR RMR lidar. Basic component is the actual edge filter, but the DORIS setup includes also stabilizing and monitoring the frequency of the emitted light.

Frequency stabilized seed laser

The stability of the emitted laser frequency is crucial for the wind retrieval. The transmitting lasers are injection-seeded by a stabilized seed laser. Their frequency cannot be more stable than the frequency of the seed laser. Hence, the frequency of the seed laser should be as stable as possible. The high stability of the seed laser is achieved by absorption spectroscopy. Figure 4.7 shows a scheme of the setup. Part of the 532 nm radiation from the seed laser is split into two parts. One part passes through an iodine-vapor cell and is detected afterward, the other part is detected directly. The transmittance of the iodine-vapor cell depends strongly on the frequency of the light. Hence, the signal ratio is a measure of the light's frequency. By varying the temperature and the length of the laser resonator of the seed laser, its frequency is controlled to keep the signal ratio constant. The control rate for this is about 8 Hz. The resulting frequency stability of the seed laser is better than 6 MHz over three years (*Fiedler et al.*, 2008) and less than 1 MHz over several hours respectively.

The power lasers are seeded by the infrared emission of the seed laser. The 532 nm emission is guided to a wavelength meter, to the laser pulse spectrometer (see next paragraph), and to the detection system.

Monitoring of actually emitted laser frequency

As mentioned it is very crucial to know the actual frequency of the emitted light very precisely. Since seeding the transmitting lasers does not ensure the emitted light has exactly the same frequency ν_0 as the seed light (*Nicklaus et al.*, 2007), it is required to measure the frequency ν of the emitted light. Since the frequency ν_0 of the seed light is known and very stable, it is sufficient to measure the frequency offset $d\nu = \nu - \nu_0$. This is done with the so-called

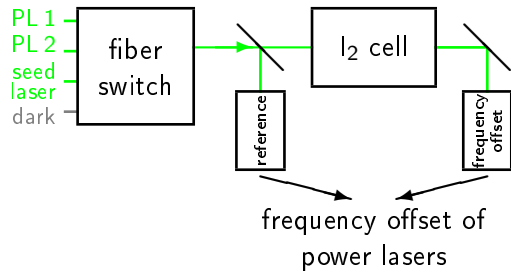


Figure 4.8 Sketch of the laser pulse spectrometer, see text for details.

laser pulse spectrometer (LPS). A sketch of the LPS is shown in Fig. 4.8. Light from different sources and a dark fiber are coupled into the LPS using a fiber switch. The dark fiber is used to determine the offset voltage of the detectors. The LPS is able to resolve the shapes of the ~ 10 ns long laser pulses. The incident light is split into two parts: One part is detected directly, the other one passes through an iodine-vapor cell and is detected afterward. Since the transmittance of the iodine-vapor cell depends strongly on the frequency of the incident light, it is possible to derive information about the frequency of the light coupled into. The retrieval and an exemplary time series of the frequency offset are presented in Sect. 4.5.2.

Edge filter and subsequent Doppler channel

As mentioned in Sect. 4.1, a cell of molecular iodine is used as frequency discriminator. The cell has a length of 15 cm. To ensure that all iodine is in the gas phase, it is heated to constant temperature of $38\text{ }^{\circ}\text{C}$ ($\pm 0.003\text{ K}$). The Doppler and the reference channel are denoted by 532 I2 and 532 Cab. in Fig. 4.6. The beam splitter in front of the iodine cell has a transmittance of 40 %.

Since the Doppler shift is calculated from the signal ratio of the Doppler channel and the reference channel, it is necessary to take variations of the detection efficiency ratio of both channels into account. This is done by feeding light from the seed laser into the detection system shortly after each laser pulse. For the seed laser light the signal ratio does not depend on frequency (since the frequency of the seed laser is stable), but only on detection efficiency ratio. The timing of seed laser light on the detection system is controlled by the chopper. To demonstrate its action, Fig. 4.9 shows exemplary range profiles of lidar raw signal measured with two different detectors of the 532 nm branch: the one with the highest sensitivity (VH, red) and the one with the lowest sensitivity (VL, green). The right ordinate denotes elapsed time after firing the laser, the left ordinate denotes corresponding range at which light was backscattered. The VH detector is an avalanche photodiode (APD). To prevent it from overload due to high signal from low altitudes it is gated. The gating altitude was set to 34 km (since the telescope was tilted 20° off-zenith, this yields a range of about 36.2 km). The VL detector is a photomultiplier tube (PMT). It is not gated, its lower range limit is defined by the chopper blade, which opens at a range of about 13 km. The atmospheric signal gets weaker with range and vanishes when the range profile gets flat. Then most of the signal is atmospheric background, i.e., stray light from the sun or the moon. Approximately 1.2 ms after the laser pulse, the chopper enables light from the seed laser into the detection system, causing a steep signal increase. Around 0.2 ms later the chopper blocks the light from the telescope, all measured signal is now from the seed laser and thermionic emission from the

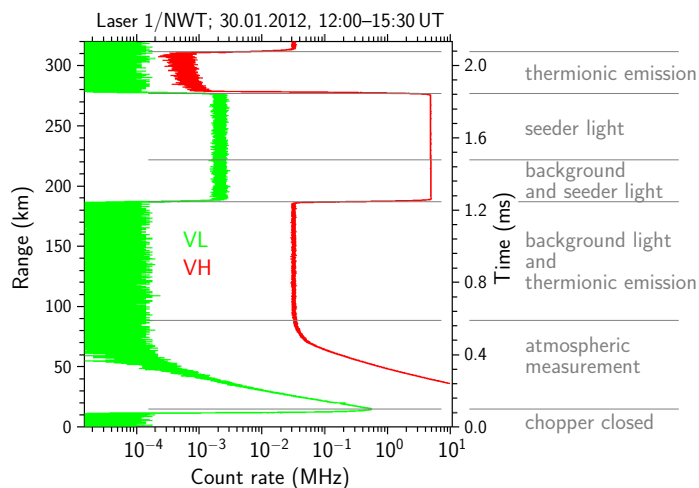


Figure 4.9 Exemplary lidar backscatter signal from two detectors (highest and lowest sensitivity) of the reference channel, measured with laser 1/NWT. Right ordinate denotes time elapsed since firing the laser, left ordinate denotes corresponding range. See text for details.

detector. Again roughly 0.4 ms later the seed laser light is also blocked by the chopper, no light hits the detectors. The period in which only seed laser light hits the detectors (≈ 1.48 – 1.85 ms after firing the laser) is used to measure the detection efficiency ratio of Doppler and reference channel. Exemplary time series are presented in Sect. 4.5.1.

4.3 Wind retrieval: from measured Doppler ratio to wind speed

The measurement principle presented in Sect. 4.1 is very idealized: Apart from the transmittance spectrum of the actual iodine cell it takes no instrumental effects into account. Hence, this has to be done in the further retrieval. This is outlined in this section.

The Doppler ratio introduced in Sect. 4.1 is modeled with assumptions concerning only atmospheric parameters (but no instrumental), it is called **modeled Doppler ratio** D_{model} . It is modeled for given wind speed and temperature, using a transmittance spectrum of the iodine cell which is normalized properly:

$$D_{\text{model}} = \frac{\int d\nu I(\nu) T_{I_2}(\nu)}{\int d\nu I(\nu)}, \quad (4.1)$$

with $I(\nu)$ as incident light intensity, dependent on atmospheric temperature and wind, and $T_{I_2}(\nu)$ as transmittance spectrum of the iodine cell.

The actually measured signal ratio of Doppler and reference channel depends not only on atmospheric conditions but also on instrumental effects. To distinguish it from the modeled

Doppler ratio, it is called **measured Doppler ratio** D_{meas} :

$$D_{\text{meas}} = \frac{S_{\text{I}_2}}{S_0} \quad (4.2a)$$

$$= \frac{\int d\nu I(\nu) T_{\text{I}_2}(\nu)}{\int d\nu I(\nu)} \cdot \frac{Q_{\text{I}_2}}{Q_0} \cdot B|_{\text{tel}}, \quad (4.2b)$$

with S_{I_2} and S_0 as the detected signals behind and in front of the iodine cell, Q_{I_2} and Q_0 as detection efficiencies of the respective detectors, and $B|_{\text{tel}}$ as beam splitting ratio, cumulating beam splitter and alignment for light coupled into the detection system through one of the telescope ports.

Combining Eqs. (4.1) and (4.2b) yields:

$$D_{\text{model}} = D_{\text{meas}} \cdot \frac{1}{\frac{Q_{\text{I}_2}}{Q_0} \cdot B|_{\text{tel}}}. \quad (4.3)$$

Hence, it is necessary to determine the detection efficiency ratio $\frac{Q_{\text{I}_2}}{Q_0}$ and the alignment factor $B|_{\text{tel}}$.

To measure the ratio of detection efficiencies $\frac{Q_{\text{I}_2}}{Q_0}$ (which may vary with time), light from the seed laser is coupled into the detection system 1.2 ms after each laser pulse (see Fig. 4.9). This yields the **seeder Doppler ratio** D_{seeder} :

$$D_{\text{seeder}} = \frac{Q_{\text{I}_2}}{Q_0} \cdot T_{\text{I}_2}|_{\nu_0} \cdot B|_{\text{seeder}}, \quad (4.4)$$

with $T_{\text{I}_2}|_{\nu_0}$ as transmittance of the iodine cell at the seed laser frequency ν_0 ; $B|_{\text{seeder}}$ corresponds to $B|_{\text{tel}}$, but for the seeder port.

Hence, applying the seeder Doppler ratio on Eq. (4.3) eliminates the detection efficiency ratio but entails further rescaling:

$$D_{\text{model}} = D_{\text{meas}} \cdot D_{\text{seeder}}^{-1} \cdot T_{\text{I}_2}|_{\nu_0} \cdot \frac{B|_{\text{seeder}}}{B|_{\text{tel}}}. \quad (4.5)$$

The transmittance of the iodine cell at the seeder frequency $T_{\text{I}_2}|_{\nu_0}$ can be measured during calibration measurements and taken into account.

The quotient of the alignment factors $B|_{\text{tel}}$ and $B|_{\text{seeder}}$ can be measured during calibration measurements as well. For this, light from the seed laser is coupled into the detection system simultaneously through the telescope ports and the seeder port (see Sect. 4.4 for details). Then the ratio of the Doppler ratios measured through telescope port ($D|_{\text{tel}}$) and through seeder port ($D|_{\text{seeder}}$) yields the **entrance ratio** E_{tel} :

$$E_{\text{tel}} = \frac{D|_{\text{tel}}}{D|_{\text{seeder}}} \quad (4.6a)$$

$$= \frac{\frac{\int d\nu I(\nu) T_{\text{I}_2}(\nu)}{\int d\nu I(\nu)} \cdot \frac{Q_{\text{I}_2}}{Q_0} \cdot B|_{\text{tel}}}{\frac{\int d\nu I(\nu) T_{\text{I}_2}(\nu)}{\int d\nu I(\nu)} \cdot \frac{Q_{\text{I}_2}}{Q_0} \cdot B|_{\text{seeder}}} \quad (4.6b)$$

$$= \frac{B|_{\text{tel}}}{B|_{\text{seeder}}}. \quad (4.6c)$$

Hence, E_{tel} accounts for differences between $B|_{\text{seeder}}$ and $B|_{\text{tel}}$.

This gives for the comparison of modeled and measured Doppler ratio:

$$D_{\text{model}} = D_{\text{meas}} \cdot D_{\text{seeder}}^{-1} \cdot T_{I_2|\nu_0} \cdot E_{\text{tel}}^{-1} = D'_{\text{meas}}. \quad (4.7)$$

To summarize: It is needed to rescale the measured Doppler ratio D_{meas} with the seeder Doppler ratio D_{seeder} , the iodine transmittance $T_{I_2|\nu_0}$ at the stabilization frequency, and the entrance ratio E_{tel} in order to compare this rescaled measured Doppler ratio D'_{meas} with the lookup table of modeled Doppler ratio D_{model} .

To derive unambiguous line-of-sight wind speed from the comparison of D'_{meas} and D_{model} temperature is needed. The temperature retrieval is shortly outlined in Sect. 4.3.1. Due to the difference between actually emitted frequency and seed laser frequency, the retrieved line-of-sight wind needs to be shifted by a wind offset that corresponds to the frequency offset (see Sect. 4.5.2). For off-zenith measurements the line-of-sight wind has to be transformed to zonal or meridional wind speed. This is described in the following paragraph.

Projection of line-of-sight wind to horizontal wind

The measured wind speed corresponds to the wind along the line of sight of the lidar. Hence, it contains contributions from horizontal and vertical wind components as well. Various approaches how to transform the measured line-of-sight winds obtained during off-zenith measurements to horizontal winds are discussed in literature. The most common assumption is that the vertical wind is close to zero or negligible compared to the horizontal wind (e.g., *Chanin et al.*, 1989; *Souprayen et al.*, 1999; *Franke et al.*, 2005; *Liu et al.*, 2007). Others assume a uniform wind field and couple coplanar measurements to derive wind in the corresponding plane (e.g., eastward and westward pointing laser/telescope) to derive zonal wind (e.g., *Xia et al.*, 2012).

Liu et al. (2002) compare two approaches to calculate horizontal wind from off-zenith and zenith measurement and to estimate its measurement uncertainty, which are presented in detail in App. C.1. They conclude, that it is sufficient to take the variability of vertical wind into account for estimation of measurement uncertainty, and to ignore the actually measured vertical wind for projecting line-of-sight wind to horizontal wind. Analysis of wind data from DORIS backs this conclusion: Taking the vertical wind ($w \lesssim 2$ m/s, see App. C.1) into account would not alter the derived horizontal wind speed to an extent larger than the actual measurement uncertainty ($\Delta v_{\text{l.o.s.}} \sim 2\text{--}5$ m/s). In the retrieval which is presented in this thesis, vertical winds are not included for the projection to horizontal winds, neither in projection of line-of-sight winds onto the horizontal plane nor for estimation of measurement uncertainty. Appendix C.1 compares different estimates with regard to over- or underestimation of derived horizontal wind (when neglecting vertical wind component) and its measurement uncertainty.

For a typical measurement setup of the ALOMAR RMR lidar, the NWT points to North and the SET points to East. The zenith-distance angle θ is typically 20° or 30° . Zonal wind u and meridional wind v are then calculated from the respective line-of-sight wind $v_{\text{l.o.s.}}$ following:

$$u = \frac{1}{\sin \theta_{\text{SET}}} \cdot v_{\text{l.o.s.}}|_{\text{SET}} \quad (4.8a)$$

and

$$v = \frac{1}{\sin \theta_{\text{NWT}}} \cdot v_{\text{l.o.s.}}|_{\text{NWT}}. \quad (4.8b)$$

During coplanar measurements the zonal wind derived by NWT is

$$u = -\frac{1}{\sin \theta_{\text{NWT}}} \cdot v_{\text{l.o.s.}}|_{\text{NWT}}. \quad (4.8c)$$

4.3.1 Temperature retrieval

As stated in Sect. 3.1.1 the lidar raw signal can be transformed to a vertical profile of atmospheric density. For this purpose the reference channel of the 532 nm branch is used. Assuming the atmosphere is in hydrostatic equilibrium and obeys the perfect gas law, a temperature profile can be calculated from the relative density profile by hydrostatic integration (*Kent and Wright, 1970; Hauchecorne and Chanin, 1980*). The idea is to start the temperature integration at high altitude and guessing a start temperature (e.g., from a reference atmosphere). During the downward integration atmospheric density increases exponential, resulting in a fast approximation of the derived temperature toward the actual atmospheric temperature. A few kilometers below the start altitude the influence of the guessed start temperature vanishes. A detailed description of this method and its application to data of the ALOMAR RMR lidar are presented in *Schöch (2007)*.

4.3.2 Measurement uncertainties

The measurement uncertainty ΔS of the raw signal is given by Poisson statistics and the uncertainty in determining the background count rate. The uncertainty ΔT of the derived temperature follows directly from hydrostatic integration, with a small contribution which originates from guessing the temperature at the start altitude for the hydrostatic integration. Due to exponential increase of atmospheric density this contribution decreases very fast. The uncertainty $\Delta v_{\text{l.o.s.}}$ of line-of-sight wind follows from the uncertainty $\Delta D'_{\text{meas}}$ of measured Doppler ratio (which is determined by ΔS_0 , ΔS_{I_2} , and $\Delta D_{\text{seed}}'$) and temperature uncertainty ΔT , and the respective partial derivative of the modeled Doppler ratio matrix:

$$\Delta v_{\text{l.o.s.}} = \sqrt{\left(\left(\frac{\partial D_{\text{model}}}{\partial v_{\text{l.o.s.}}} \right)^{-1} \cdot \Delta D'_{\text{meas}} \right)^2 + \left(\frac{\partial D_{\text{model}}}{\partial T} \cdot \left(\frac{\partial D_{\text{model}}}{\partial v_{\text{l.o.s.}}} \right)^{-1} \cdot \Delta T \right)^2}. \quad (4.9)$$

The final uncertainty of zonal, meridional, or vertical wind speed includes additionally a contribution from measurement uncertainty $\Delta d\nu$ of the frequency offset $d\nu$. Typical measurement uncertainties of the line-of-sight wind for 1 h integration are ≈ 0.8 m/s and ≈ 7 m/s at 50 km and 80 km altitude, respectively.

4.4 Calibration

The need for various calibrations was mentioned in the previous section. This includes determination of the actual transmittance spectrum $T_{\text{I}_2}(\nu)$ of the iodine cell and finding the

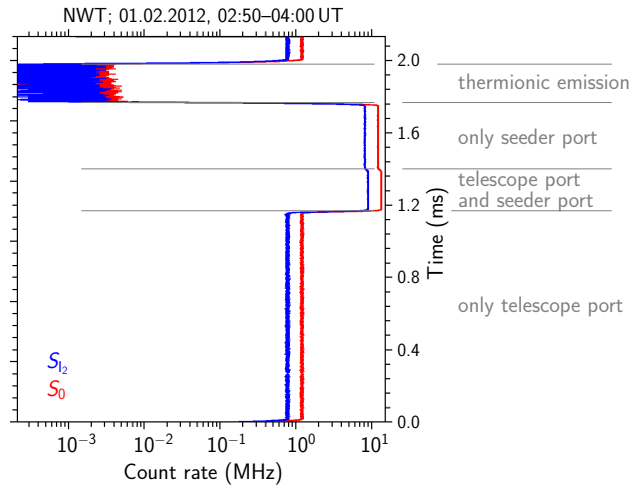


Figure 4.10 Exemplary lidar count rate from Doppler channel (S_{I_2} , blue) and reference channel (S_0 , red) during calibration measurement. See text for details.

stabilization frequency ν_0 , and the entrance ratio E_{tel} . Both calibrations are described in Sects. 4.4.2 and 4.4.3, respectively, on the basis of an exemplary calibration on 8/9 February 2012. A calibration is only valid as long as the respective experimental setup remains unchanged, this is discussed qualitatively in Sect. 4.4.4. This section starts with a description of the experimental setup for calibration measurements.

4.4.1 Experimental setup for calibration

For calibration it is needed to feed light from the seed laser into the detection system through the telescope ports and the seed laser port simultaneously. It is possible to unplug the telescope fibers from the telescopes and connect them with fibers carrying light from the seed laser. In this way seed laser light is fed into the detection system through the same ports like backscattered light during normal atmospheric measurements. Figure 4.10 shows the resulting profiles of lidar count rate, similar to the profiles shown in Fig. 4.9 for an atmospheric measurement. The time axis refers now to an internal trigger, not to firing of the lasers. The chopper blade opens directly after the trigger pulse, enabling light from the telescope ports. Nearly 1.2 ms later the chopper enables additionally light from the seed laser port, 1.4 ms after the trigger pulse light from the telescopes is blocked. All light is blocked roughly 1.8 ms after the trigger pulse.

4.4.2 Iodine spectrum and stabilization frequency

For deriving a transmittance spectrum of the iodine cell at the detection system the frequency of the seed laser can be varied. Figure 4.11 shows for the calibration on 8/9 February 2012 the temporal evolution of seed laser frequency (red line, scale relative to stabilization frequency ν_0) and signal ratio from the seed laser absorption spectroscopy (blue line), which was presented in Sect. 4.2.2 and Fig. 4.7. Around 17 UT the seed laser frequency was stabilized at a signal ratio of 0.35. After that the frequency was driven out of the absorption line and subsequently the frequency control was inactive until 20:10 UT. Then the scan of the frequency started, covering the frequency range of interest four times. One scan direction

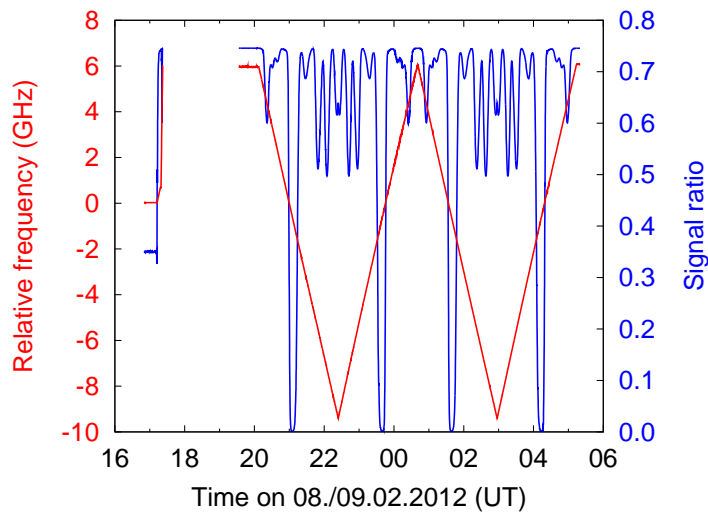


Figure 4.11 Frequency scan, results from seed laser platform: frequency of the seed laser (red line, left ordinate) and signal ratio at seed laser iodine cell (blue line, right ordinate) over time. Frequency axis is relative to stabilization frequency ν_0 . See text for details.

takes about 2 h and 15 min. The whole calibration sequence ended at 5:20 UT on the next morning.

Figure 4.12 shows various data from the detection system for the same calibration measurement. Panel (a) shows the measured signals for the Doppler channel (S_{I_2}) and the reference channel (S_0), for seed laser port and both telescope ports. The signal variation of the reference channel (e.g., gray line for seed laser port) is influenced by the output power of the seed laser, whereas the signal of the Doppler channel (e.g., orange line for seed laser port) is additionally influenced by the transmittance of the iodine cell. Comparing with Fig. 4.11, the frequency was stabilized around 17 UT, outside the absorption line around 20 UT, and subsequently scanning. Around 20 UT S_0 is constant, whereas S_{I_2} decreases abruptly shortly before 20 UT: During the data gap the iodine cell had been removed from the optical path and was inserted again at 19:50 UT, affecting only S_{I_2} . Panel (b) shows the Doppler ratio S_{I_2}/S_0 for the seed laser port, on which we focus in the following. Obviously the Doppler ratio contains values larger than 1. This is because the Doppler ratio is not normalized, i.e., it does not correspond to the transmittance of the iodine cell. Normalization can be done using the period when the iodine cell was not in the optical path (i.e., before 19:50 UT): During that time, the normalized Doppler ratio has to be 1 in order to correspond to transmittance of the iodine cell (which is 1 while the cell is removed from the optical path). The normalized Doppler ratio, now referred to as transmittance of the iodine cell, is shown in panel (c). For the period, during that the iodine cell was removed from optical path (before 19:50 UT), the transmittance is 1 (emphasized by dotted line). The transmittance $T_{I_2}|_{\nu_0}$ at the stabilization frequency ν_0 is marked with a dashed blue line. When the transmittance data $T_{I_2}(t)$ are coupled with the frequency data $\nu(t)$ from Fig. 4.11 a transmittance spectrum $T_{I_2}(\nu)$ is obtained. The resulting transmittance spectrum is shown in panel (d). Comparison with a theoretical spectrum calculated from the I_2 atlas (*Gerstenkorn and Luc, 1978*) for a cell with given length and iodine concentration allows to shift the spectrum along the frequency axis to get an absolute frequency scale. The stabilization frequency ν_0 and corresponding transmittance $T_{I_2}|_{\nu_0}$ are marked by vertical respectively horizontal orange lines. The measured iodine transmittance

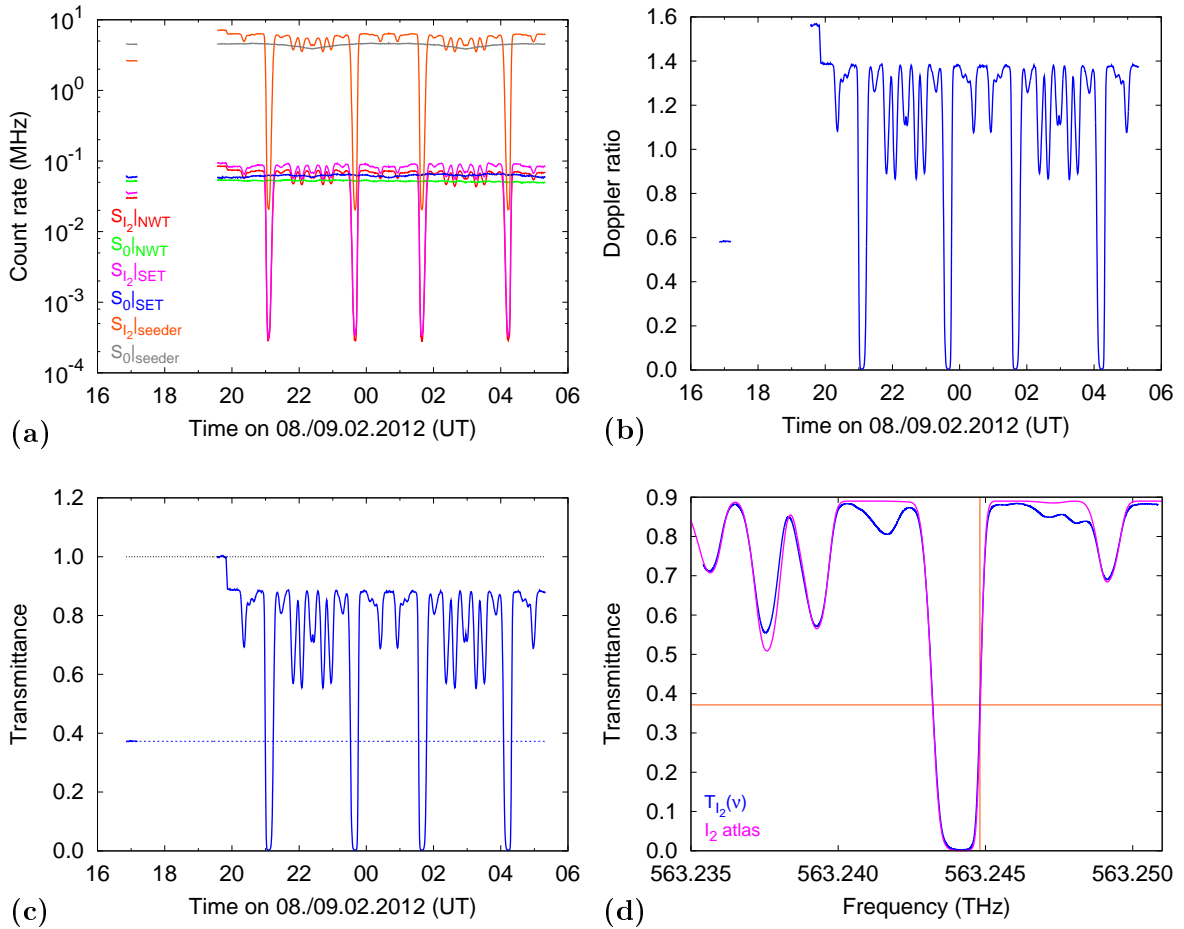


Figure 4.12 Determination of iodine spectrum and stabilization frequency: (a) signal for different detectors and for different ports over time; (b) Doppler ratio S_{I_2}/S_0 for seed laser port over time; (c) normalized Doppler ratio over time, this corresponds to the actual transmittance T_{I_2} of the iodine cell; (d) transmittance spectrum $T_{I_2}(\nu)$ of the iodine cell, vertical and horizontal orange lines mark the stabilization frequency ν_0 and the corresponding transmittance $T_{I_2}|\nu_0$.

spectrum shows some minor differences to the theoretical spectrum. These might be caused by the glass windows of the iodine cell. This highlights the necessity to measure the actual transmittance spectrum and to include in the wind retrieval.

This transmittance spectrum is finally used to model the lookup table of Doppler ratio for various combinations of temperature and wind speed, as shown in Sect. 4.1 and Fig. 4.4. Actually the shape of the transmittance spectrum varies slightly for different ports of the detection system. Therefore, the Doppler ratio matrix is modeled for each telescope port and during the wind retrieval the respective lookup table is used.

Appendix B.2 lists calibration measurements during which the iodine spectrum was determined. The derived transmittance $T_{I_2}|\nu_0$ is tabulated in Tab. B.2.

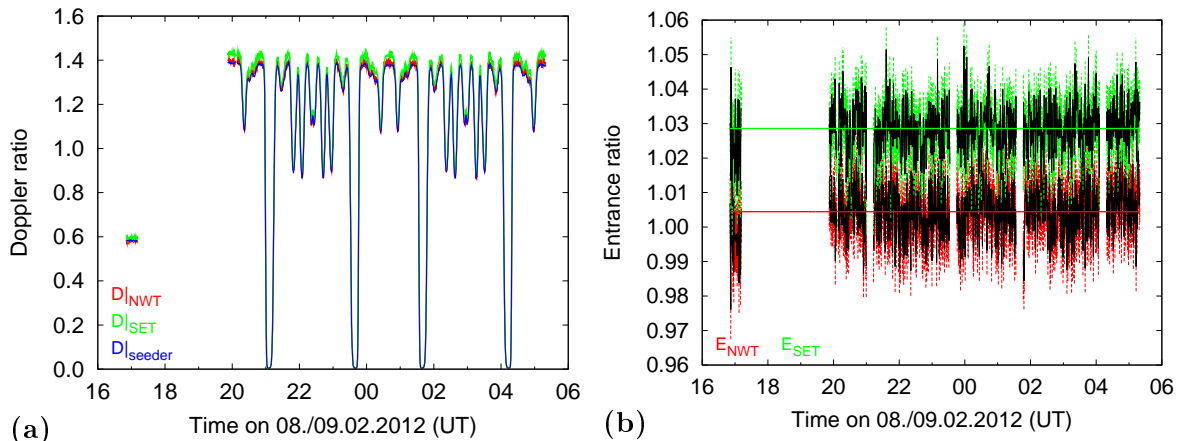


Figure 4.13 Determination of entrance ratio during seed laser scan: **(a)** Doppler ratios for NWT (red), SET (green), and seed laser port (blue); **(b)** entrance ratio $E_{\text{tel}} = D|_{\text{tel}}/D|_{\text{seeder}}$ for NWT (red error bars) and SET (green error bars), horizontal lines denote the respective average.

4.4.3 Entrance ratio

The entrance ratio E_{tel} accounts for differences in the alignment between the seed laser port and the telescope ports. The ports have different images on the detector areas. This leads to different Doppler ratios when light is coupled into the detection system either through seed laser port or telescope ports (*Baumgarten, 2010*). The entrance ratio depends on the elements along the optical paths from the telescopes, respectively the seed laser port, to the detectors. This includes: telescope fibers, dichroic mirrors at detection system, the daylight filter or its bypass, and polarizer and attenuator in seed laser branch. The entrance ratio is stable as long as the design of the detection system and the telescope fibers are not changed. Hence, it differs for daylight and nighttime configuration (due to the daylight filter) and for winter and summer configuration (the dichroic mirror D3 is installed during winter but removed during summer).

The entrance ratio can be determined during seed laser scans, since it does not depend on the frequency of the incident light, but shorter calibration measurements without scanning the seed laser frequency are also sufficient. The only requirement is that the iodine cell is in the optical path like during normal measurements. The retrieval is quite simple: Measure the count rates of Doppler channel and reference channel for light from seed laser port and telescope ports, build the respective Doppler ratios, and finally build the ratio of the Doppler ratios (see Eq. (4.6)).

Figure 4.13(a) shows Doppler ratios for all ports of the detection system, measured during a calibration measurement on 8/9 February 2012. This panel corresponds to Fig. 4.12(b), except that the period, during that the iodine cell was removed from the optical path, is excluded. While $D|_{\text{NWT}}$ (red line) and $D|_{\text{seeder}}$ (blue line) are hard to distinguish, the difference between $D|_{\text{SET}}$ (green line) and $D|_{\text{seeder}}$ is obvious. Figure 4.13(b) shows resulting entrance ratios for NWT (red error bars) and SET (green error bars). The temporal variation of E_{tel} is caused by measurement uncertainty, as final value we take the average. The entrance ratio for NWT is close to 1 (1.0078), while E_{SET} is 1.028. In the latter case, neglecting this factor would lead to false line-of-sight wind speeds by few 10 m/s.

A list of entrance ratios determined during calibration measurements is presented in App. B.2.

4.4.4 Validity of a calibration

Different instrumental changes affect the validity of a calibration. Work on the detection system changes the entrance ratio E_{tel} , just as new telescope fibers do. But both do not affect the transmittance spectrum $T_{\text{I}_2}(\nu)$ of the iodine-vapor cell. The transmittance spectrum remains constant as long as the cell's characteristics not alter. On the other hand, changing the stabilization of the seed laser affects the seed laser frequency ν_0 , and therefore the transmittance $T_{\text{I}_2}|_{\nu_0}$ of the iodine-vapor cell at the detection system and the seeder Doppler ratio D_{seeder} . Correspondingly, the analysis of data which are obtained over several years requires detailed overview of all instrumental changes. This includes variation of the seed laser frequency, replacement of telescope fibers, and routine and particular modifications at the detection system (e.g., bypassing the daylight filter and replacement of detectors respectively). A complete overview of these changes is given in App. B.1.

The bypass of the daylight filter is somewhat delicate. Although the mirrors (labeled M1 and M1.c in Fig. 4.6) are mounted on kinematic bases to allow reproducible positioning, it might happen that the mirrors are not installed properly. In that case the beam path on the detection systems differs from its normal way, resulting in a variation of the amount of light that hits the detector area. This variation is different for all ports of the detection system (seed laser port, NWT port, SET port) and different for reference and Doppler channel. As is shown in Sect. 4.5.1, it is possible to detect such improperly installed mirrors, but currently it is not possible to take the resultant effects automatically into account during the wind retrieval (see App. B.1). Estimating an additional factor C_E to Eq. (4.7) allows to describe the effect of such misalignment:

$$D_{\text{model}} = D'_{\text{meas}} = D_{\text{meas}} \cdot D_{\text{seeder}}^{-1} \cdot T_{\text{I}_2}|_{\nu_0} \cdot E_{\text{tel}}^{-1} \cdot C_E. \quad (4.10)$$

4.5 Performance monitoring

4.5.1 Seeder Doppler ratio

The DORIS branch of the detection system consists of two channels: reference channel in front of the iodine-vapor cell and Doppler channel behind the iodine-vapor cell. Since the measurement principle of DORIS relies on the measurement of small variations of the signal ratio of both channels, it is necessary to monitor the detection efficiency ratio of both channels precisely. By feeding light from the stable seed laser into the detection system after each laser pulse (see Sect. 4.2.2 and Fig. 4.9) it is possible to measure the signal ratio autonomous from the atmospheric measurement. This yields the seeder Doppler ratio D_{seeder} which is a measure of detection efficiency ratio. Furthermore, monitoring the seeder Doppler ratio allows detecting if the bypass of the daylight filter is mounted properly. Figure 4.14 shows time series of seed laser count rates ($S_0|_{\text{seeder}}$ and $S_{\text{I}_2}|_{\text{seeder}}$) and seeder Doppler ratio $D_{\text{seeder}} = S_{\text{I}_2}|_{\text{seeder}} \cdot S_0|_{\text{seeder}}^{-1}$ for 21–23 January 2012. Obvious are the abrupt changes at about 15 UT and 7 UT, respectively. These are caused by changing from daylight to nighttime configuration and vice versa. Note that during the first night $S_0|_{\text{seeder}}$ and $S_{\text{I}_2}|_{\text{seeder}}$ are lower than during day, even though the daylight filter is bypassed, while during the second night $S_0|_{\text{seeder}}$ and $S_{\text{I}_2}|_{\text{seeder}}$ are remarkably higher. This is due to improper mounting of the bypass of the daylight filter. The impact on the seeder Doppler ratio is also shown in the lower panel.

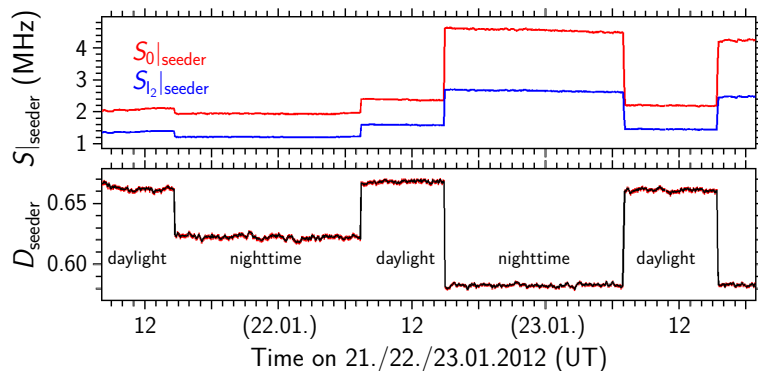


Figure 4.14 Exemplary time series of seed laser count rates (upper panel) $S_{0|\text{seedler}}$ (red) and $S_{I_2|\text{seedler}}$ (blue) and seed Doppler ratio $D_{\text{seedler}} = S_{I_2|\text{seedler}} \cdot S_{0|\text{seedler}}^{-1}$ (lower panel) on 21.–23.01.2012. See text for details.

The idea to take the seeder Doppler ratio into account is only to monitor temporal variations of the detection efficiency ratio. The more obvious larger variations of D_{seedler} are due to changes of the experimental setup. They are taken into account during the wind retrieval by the telescope entrance ratio E_{tel} .

4.5.2 Laser frequency offset

The offset between seed laser frequency and actually emitted frequency is measured with the laser pulse spectrometer (LPS). The setup of the LPS was presented in Sect. 4.2.2.

Assuming only small frequency offsets (small enough to assume the edge of the iodine absorption line to be linear), a simple approach to derive the frequency offset is to transform the signal ratio difference (between power laser and seed laser) into a frequency difference:

$$\frac{S_{I_2}}{S_0} \Big|_{\nu} - \frac{S_{I_2}}{S_0} \Big|_{\nu_0} \propto T_{I_2} \Big|_{\nu} - T_{I_2} \Big|_{\nu_0} \quad (4.11a)$$

$$\propto (\nu - \nu_0) \cdot \frac{\partial T_{I_2}}{\partial \nu} \quad (4.11b)$$

$$\propto d\nu. \quad (4.11c)$$

This simple approach is not always valid because of two reasons. First, the frequency offset might be too large to assume a linear shape of the edge of the absorption line. Second, due to different line widths of power laser and seed laser the shape of the edge might differ for seed laser and power laser. Hence, a better approach to derive the frequency offset is to take the actual shape of the absorption line into account.

During calibration measurements the power laser frequency can be varied by slowly varying the seed laser frequency. This allows to determine the shape of the edge of the absorption line with power laser and seed laser. Figure 4.15(a) shows the edge measured with laser 1 and the seed laser. Slight differences between laser 1 and seed laser are apparent. In a similar approach like the one for the wind retrieval (cf. Sect. 4.1 and Fig. 4.4) this data is used to simulate a matrix of power laser signal ratio for various combinations of seed laser signal ratio (i.e., seed laser frequency) and frequency offset. The resulting matrix is shown in Fig. 4.15(b). This matrix is then used as lookup table to derive frequency offset from seed laser signal ratio

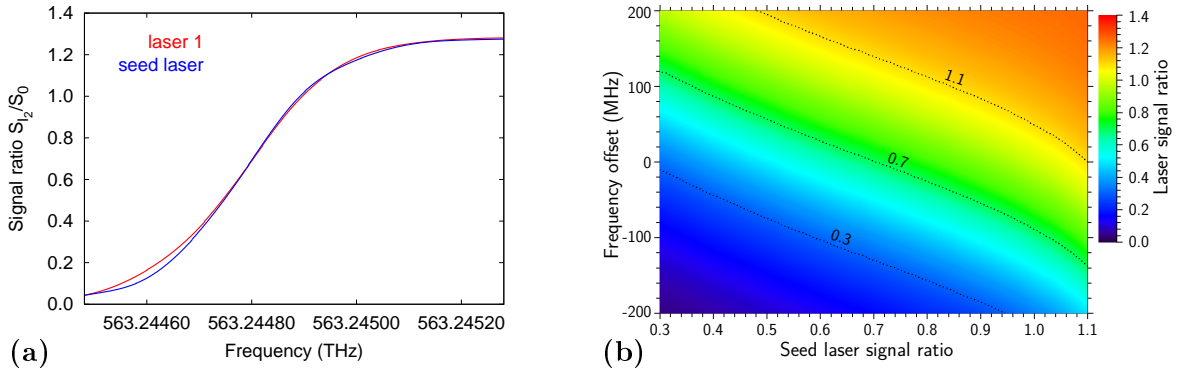


Figure 4.15 Retrieval of frequency offset: (a) edge of absorption line determined with power laser 1 (red) and seed laser (blue); (b) modeled lookup table to derive frequency offset, dotted lines indicate isolines for laser signal ratio of 0.3, 0.7, and 1.1. The data were obtained during a calibration measurement on 18.09.2009. See text for details.

and power laser signal ratio (similar to the Doppler ratio matrix shown in Fig. 4.4). Since the lookup table regards different seed laser signal ratios the matrix is valid even if the seed laser frequency is changed.

To transform the frequency offset into a line-of-sight wind speed offset, Eq. (3.6b) is applied. A frequency offset of 1 MHz yields a wind speed offset of about -0.266 m/s (for $\nu_0 \approx 563.25$ THz):

$$dv_{\text{l.o.s.}} = -\frac{c}{2\nu_0} \cdot d\nu \quad (4.12a)$$

$$\frac{dv_{\text{l.o.s.}}}{\text{m/s}} = -0.266 \cdot \frac{d\nu}{\text{MHz}}. \quad (4.12b)$$

This offset is taken into account when calculating line-of-sight wind speed.

Some attention concerning the sign of the correction is advisable. The wind speed offset needs to be subtracted from the derived line-of-sight wind. Let us assume zero wind and negative frequency offset. This negative frequency offset causes a somewhat smaller Doppler ratio (see Fig. 4.3(b) vs. (a)). This smaller Doppler ratio looks just as zero frequency offset and positive line-of-sight wind. Since Eq. (4.12b) yields positive wind offset, we have to subtract this positive wind offset from the initially derived positive line-off-sight wind to obtain finally zero line-of-sight wind.

Figure 4.16 shows exemplary time series of frequency offset of laser 1 and laser 2 and respective wind offset for 21–23 January 2012. For laser 1 the frequency offset changed during the first 25 min from about 5 MHz to -40 MHz and is subsequently more stable between about -30 to -40 MHz, yielding an offset of line-of-sight wind speed of about 7 to 12 m/s. The frequency offset of laser 2 is -5 to -20 MHz, yielding an offset of line-of-sight wind of about 1 to 5 m/s.

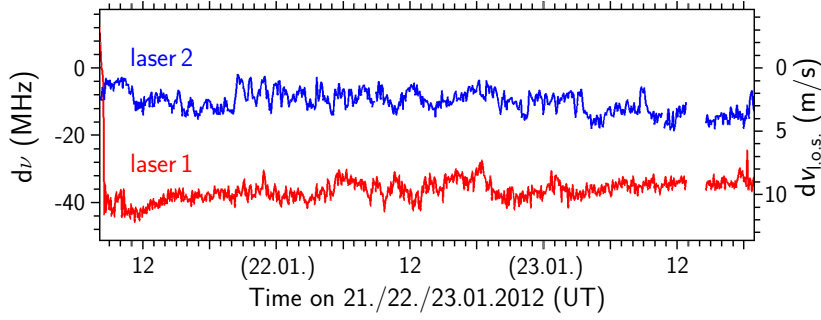


Figure 4.16 Exemplary time series of frequency offset (left ordinate) and resultant wind offset (right ordinate) for laser 1 (red) and laser 2 (blue) on 21.–23.01.2012.

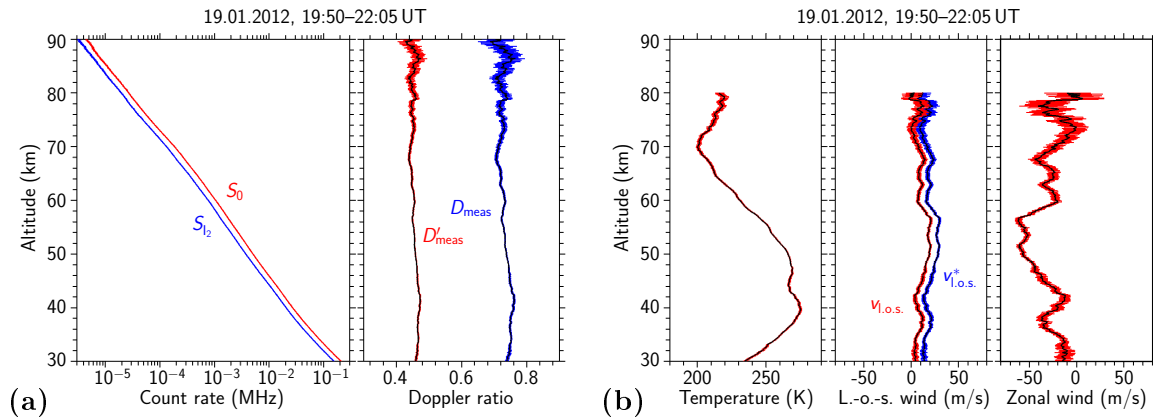


Figure 4.17 Exemplary retrieval with data measured with laser 1/NWT on 19 January 2012. (a) Count rates of Doppler channel (blue) and reference channel (red) and resulting Doppler ratio before (blue error bars) and after rescaling (red error bars). (b) Temperature calculated from reference channel, apparent line-of-sight wind without correction of frequency offset (blue error bars) and actual line-of-sight wind after correction of frequency offset (red error bars), final zonal wind speed. See text for details.

4.6 Summary – exemplary retrieval

This chapter closes with a brief recapitulation of the wind retrieval on the basis of an example. For this, data from laser 1/NWT measured on 19 January 2012 is used, integrated between 19:50 and 22:05 UT. On that day the NWT pointed to east, the zenith-distance angle was 20° . The left panel of Fig. 4.17(a) shows measured altitude profiles of lidar backscatter signal of reference channel (red) and Doppler channel (blue). The ratio of both, the measured Doppler signal D_{meas} , is shown in the right panel with blue error bars. This measured Doppler ratio is then rescaled according to Eq. (4.7) with seeder Doppler ratio D_{seeder} , iodine transmittance $T_{I_2}|_{\nu_0}$ at stabilization frequency and telescope entrance ratio E_{tel} . The resultant altitude profile of rescaled measured Doppler ratio D'_{meas} is shown with red error bars. From the count rate of the reference channel a temperature profile is derived, which is shown in the left panel of Fig. 4.17(b). Using the profiles of rescaled Doppler ratio and temperature, and the lookup table of modeled Doppler ratio D_{model} yields a profile of ap-

Chapter 4 The Doppler Rayleigh Iodine Spectrometer

parent line-of-sight wind $v_{1.o.s.}^*$. This is shown in the middle panel of Fig. 4.17(b) with blue error bars. Considering the wind offset due to the frequency offset between power laser and seed laser true line-of-sight wind $v_{1.o.s.}$ is obtained, shown with red error bars. In the last step the line-of-sight wind is projected onto the horizontal plane, taking the azimuth and zenith-distance angle into account. The resultant altitude profile of, in this example, zonal wind speed is shown in the right panel of Fig. 4.17(b).

Chapter 5 Data set and validation

This chapter presents the data set which is used for this thesis. In this context a short overview of other data sets of middle atmosphere wind speeds is given. Then the ALOMAR RMR lidar data set is analyzed with regard to seasonal and daily coverage, and measurement length. After that three ways to show the quality of the retrieved winds are presented: vertical wind measurements, coplanar measurements of zonal wind with both lasers/telescopes of the ALOMAR RMR lidar, and finally comparison to winds measured with the co-located ALOMAR sodium lidar during a joint campaign in January 2009. Detailed analysis of derived horizontal winds and comparison to data obtained by co-located radar instruments and extracted from models follows in the next chapter.

5.1 Data set

Reports of regular lidar wind observations are rare. *Tepley (1994)* presents results obtained during 43 good nights with at least 6 h measurement data per night, cumulated between midsummer 1991 and end of 1992. The covered altitude range is 10–60 km. *Souprayen et al. (1999)* present data obtained during 170 nights between 1994 and 1997; with the restriction, that only two thirds of the data (measured since May 1996) are absolute wind measurements. The covered altitude range is 8–50 km. Sodium lidar data covering multiple years are published, e.g., by *Franke et al. (2005)* (96 h in July 2002 and October/November 2003) and *Yuan et al. (2012)* (431 h cumulated on several days in January 2003–2009). The ALOMAR Na lidar, which shares the receiving telescopes of the ALOMAR RMR lidar is operated regularly (e.g., *She et al., 2002; Kaifler, 2009; Hildebrand et al., 2012; Suzuki et al., 2013; Szewczyk et al., 2013*).

Radar instruments are operated more or less continuously. Data covering several years from Arctic sites are presented by, e.g., *Hall et al. (2003); Kumar and Hocking (2010); Sandford et al. (2010); Imura et al. (2011); Singer et al. (2012)*. These radar data are obtained very regularly but do not cover the upper stratosphere and lower mesosphere.

Results of several campaigns with meteorological rockets at Arctic locations have been published by, e.g., *Meyer et al. (1987)* (110 rockets between December 1983 and February 1984), *Lübken and Müllemann (2003)* (24 falling spheres between July and September 2001), and *Müllemann and Lübken (2005)* (125 rockets between April and October during various campaigns).

During the years 2009 to 2012 the ALOMAR RMR lidar was operated for 2943 h. All of these measurements were performed with DORIS. This data contain wind measurements with various telescope pointings, and daylight and nighttime measurements. To avoid difficulties arising from possible instabilities of the daylight filter, the data set used for this thesis is restricted to nighttime measurements (with one exception to show the daylight capability).

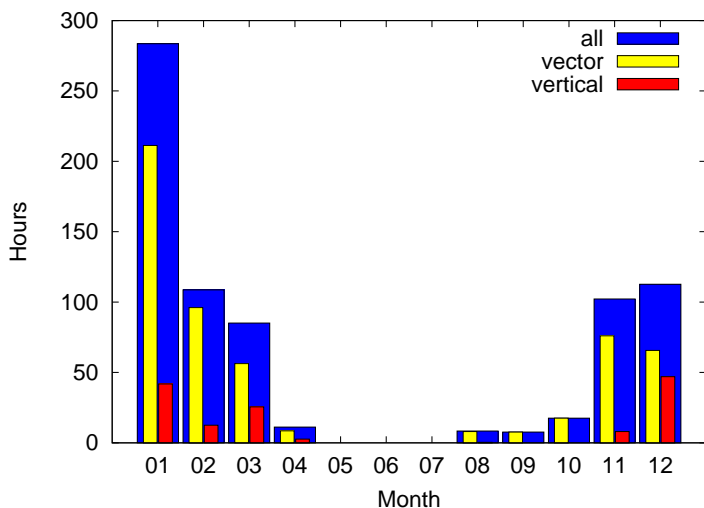


Figure 5.1 Nighttime-measurement hours per month for the years 2009 to 2012. Yellow: twin operation with one telescope pointing East and the other one pointing North; red: at least one system (i.e., laser/telescope combination) was used for vertical measurements; blue: all measurements regardless of single-system or twin operation and telescope pointing. Differences between yellow plus red and blue are due to coplanar measurements or single-system operation with off-zenith beam.

The cumulated seasonal distribution of the remaining 737 h of nighttime measurements for different measurement modes is shown in Fig. 5.1. For three quarters of the measurement hours (547 h), the lidar was operated in “vector” mode: One telescope pointing to East and the other one to North, yielding both components of the horizontal wind field simultaneously. During 138 h at least one telescope was pointing to zenith, performing vertical wind measurements (see Sect. 5.2.1). The remaining 52 h were used for coplanar measurements (especially in January and November 2009; see Sect. 5.2.2) and for very few off-zenith measurements with only one telescope. The vast majority of the nighttime measurements (692 h, 94 %) was conducted in the winter months November until March. So, further analyses will be restricted to this season. Despite the restriction to nighttime measurements between November and March, this data set, spanning 692 h, is the most extensive set of wind speeds measured in the Arctic, covering the upper stratosphere and lower mesosphere region.

Table 5.1 gives an overview of the annual and seasonal distribution of nighttime-measurement hours. During 2010, the year with most measurements, the lidar was operated nearly two and a half times as much as in 2011, the year with least measurements. In 2009 Novem-

Table 5.1 Nighttime-measurement hours per year and month

| | Nov. | Dec. | Jan. | Feb. | Mar. | Σ |
|----------|--------|--------|--------|--------|-------|----------|
| 2009 | 74.06 | 16.38 | 73.10 | 12.31 | 34.68 | 210.53 |
| 2010 | 20.58 | 57.23 | 86.08 | 58.77 | 39.71 | 262.37 |
| 2011 | 5.21 | 27.76 | 38.92 | 28.47 | 5.48 | 105.84 |
| 2012 | 2.36 | 11.31 | 85.48 | 9.12 | 5.26 | 113.53 |
| Σ | 102.21 | 112.68 | 283.58 | 108.67 | 85.13 | 692.27 |

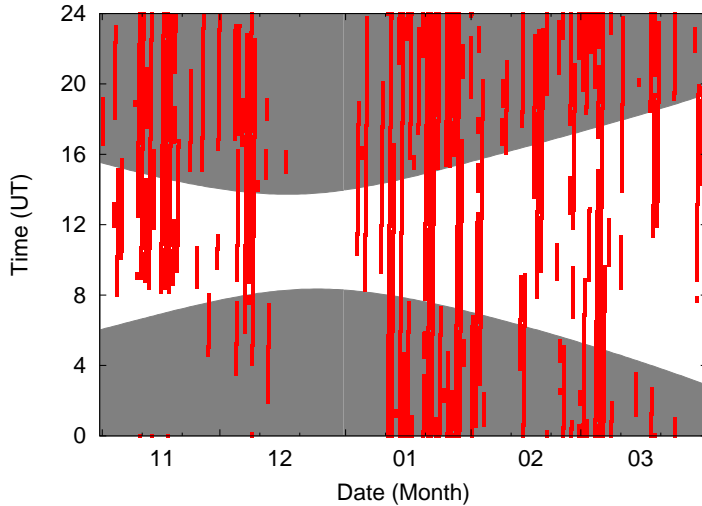


Figure 5.2 Measurements from November to March for the years 2009 to 2012 as function of season and time of day. The shaded area denotes nighttime conditions with solar elevation angles less than -7° .

ber is exceptional: It is the month with most measurements, while in all other years it is the month with least measurements; 2009 accounts for 72 % of all November measurements. Unfortunately, the amount of measurements decreased dramatically in 2011 and 2012; but January 2012 is the month with second most measurements (behind January 2010).

The cumulated measurement coverage throughout the day and season is shown in Fig. 5.2, nighttime conditions are shaded gray. The lidar is operated whenever it is permitted by available manpower and weather conditions. To capture sudden stratospheric warmings during January, February, and March enhanced effort to perform measurements is applied during these months. This results in a dense measurement coverage, and long continuous measurements. Best measurement coverage is achieved in January, which is also the month with far most measurements (cf. Fig. 5.1 and Tab. 5.1).

The distribution of measurement lengths is shown in Fig. 5.3. For this analysis a single measurement may be interrupted for not longer than one hour and may include different telescope pointings. Nearly 40 % of the measurements last for only up to 3 h, further 40 % last longer than 3 h but not longer than 10 h. The very short measurements are valuable for climatological studies, but do not contribute to analysis of gravity waves with periods of several hours. Only five measurements are longer than one day, four of them in January, the longest lasted for nearly 59 h. This one will be addressed in a detailed case study about wave characteristics in Sect. 6.3.

5.2 Validation and intercomparison

Different methods to validate wind speeds measured with DORIS will be presented. First, vertical wind speeds will be shown; second, coplanar measurements; third, combination with wind speeds measured by the co-located sodium resonance lidar. As mentioned above, only nighttime measurements are considered.

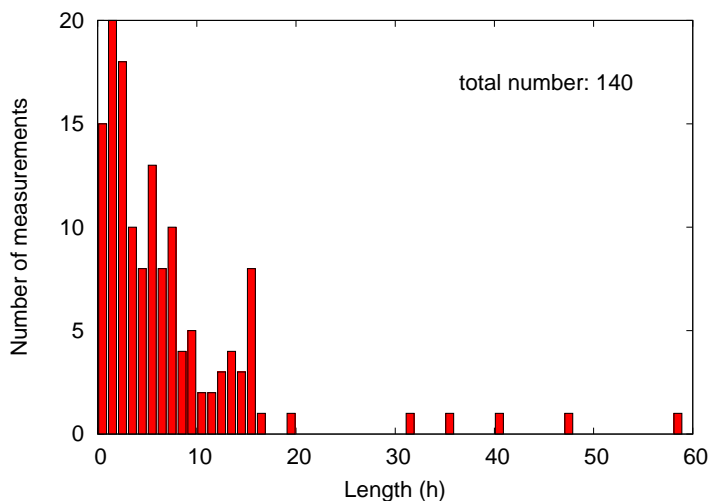


Figure 5.3 Distribution of measurement lengths for the months November to March for the years 2009 to 2012

5.2.1 Measurements of vertical wind speed

The fact that vertical wind is close to zero (see discussion in Sect. 4.3 and App. C.1) can either be used to calibrate the wind retrieval (e.g., *Chanin et al.*, 1989; *Friedman et al.*, 1997; *Garnier and Chanin*, 1992) or to show its fidelity (*Baumgarten*, 2010; *Yuan et al.*, 2009).

The vertical wind measurements are used to validate the internal calibration (see Sect. 4.4 and App. B) and if needed to correct it. For this the data of a whole measurement (i.e., at least one hour, in some cases several hours) are integrated and one single altitude profile for each measurement is calculated. The mean vertical wind $\langle w \rangle$ and the standard deviation σ_w are calculated in the altitude range 45–65 km. This altitude range was chosen since it is the range where the data quality is best: It is the lower part of the most sensitive detectors. Then the entrance ratio E_{tel} is varied and $\langle w \rangle$ and σ_w are calculated again. The E_{tel} for which the sum $|\langle w \rangle| + \sigma_w$ is smallest is regarded as appropriate entrance ratio. Since atmospheric data are used to apply this calibration method, it is called “atmospheric calibration”. Whenever possible this E_{tel} from atmospheric calibration is used instead of the one obtained from internal calibration measurement. But for measurements where this is not possible, E_{tel} from internal calibration is used.

Figure 5.4 shows two examples of vertical wind derived with internal calibration (blue error bars) and atmospheric calibration (red error bars). The first example (panel (a)) shows data from 6 December 2012, measured with the NWT. The initially derived wind profile is straight (the deviation below 40 km altitude is probably caused by concatenation of count rate profiles of different detectors (see App. A.2)) and shifted only slightly toward negative winds ($\langle w \rangle = -2.3$ m/s). The measurement uncertainty ranges from ≈ 1 to ≈ 2.5 m/s. Hence, within in the measurement uncertainty the vertical wind is very close to zero. This demonstrates the ability of DORIS to measure reliable winds in the middle atmosphere. By increasing the entrance ratio by only 0.4% the mean vertical wind became $\langle w \rangle = -0.02$ m/s. The second example (Fig 5.4(b)) shows data from 9 December 2011, measured with the SET. The initially derived altitude profile of vertical wind is obviously bent and has a large negative offset. The mean wind $\langle w \rangle$ is -27.6 m/s, the standard deviation σ_w is 1.2 m/s. This is caused by improper mounting of the daylight filter bypass (see Sect. B.1). For increased

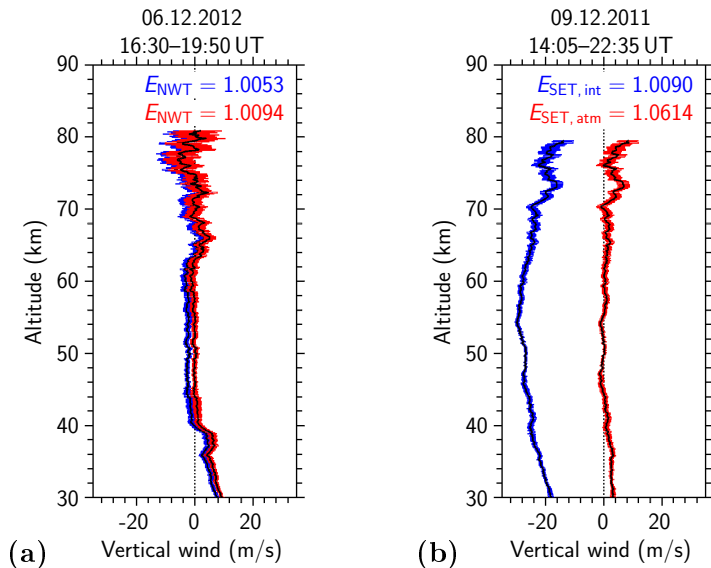


Figure 5.4 Exemplary altitude profiles of vertical wind with internal calibration (blue error bars) and atmospheric calibration (red error bars). Blue and red labels specify respective entrance ratio. **(a)** Vertical wind measured with NWT on 06.12.2012; **(b)** vertical wind measured with SET on 09.12.2011.

entrance ratio (+5%) the mean vertical wind is close to zero the altitude profile is not bent anymore. Hence, the atmospheric calibration provides the possibility to validate the internal calibration and to correct it if needed.

All vertical wind measurements in nighttime configuration that lasted at least 1 h and have good data quality (i.e., they are not disturbed by clouds or technical malfunction) are tabulated in Tabs. D.1 and D.2. The tables list the entrance ratios from internal and atmospheric calibration and the respective mean vertical winds $\langle w \rangle$ and standard deviations σ_w .

The distribution of vertical measurements is somewhat irregular. For example there are many vertical measurements in January 2009, but only for SET, and none between early March 2009 and late November 2010. During that period only the internal calibration can be used for the wind retrieval.

5.2.2 Coplanar wind measurements

Normally, main focus of attention lies on vector wind measurements, i.e., one lidar system (i.e., laser/telescope combination) probing zonal winds, the other one meridional winds. During campaigns in January and November 2009 the main focus laid on coplanar measurements with both systems probing zonal winds. This gives the possibility to compare zonal winds measured independently with both systems. When comparing zonal winds measured with both systems, one has to keep in mind, that the sounding volumes of both systems are separated by a few ten kilometers (typically the zenith-distance angle for both telescopes is 20° , resulting in a distance of the sounding volumes of 36 km at 50 km altitude). Since the wind field is not homogeneous over that distances, it is not expected that both wind speed profiles match exactly. But for integration times long enough to smooth out the effects of

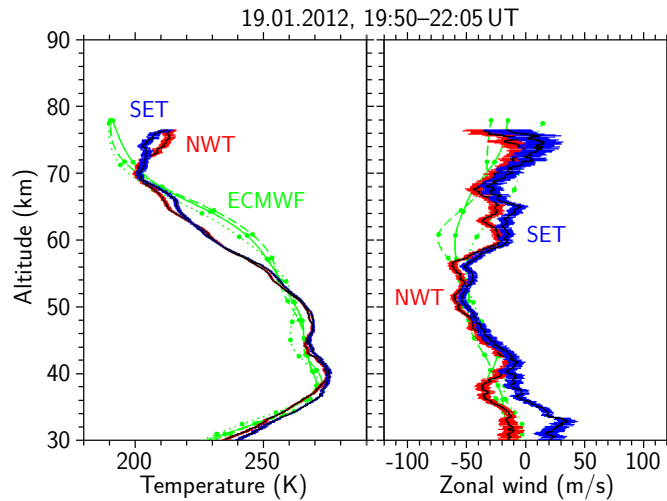


Figure 5.5 Coplanar zonal wind measurement on 19.01.2012; Altitude profiles of temperature (left panel) and zonal wind speed (right panel) measured by NWT (red error bars) and SET (blue error bars); green lines show ECMWF data for 12 UT (dashed), 18 UT (solid), and 0 UT (dotted).

gravity waves the profiles are expected to look similar. This assumption is sometimes used to calibrate or validate wind measurements: *Friedman et al.* (1997) use coplanar measurements to calibrate their wind retrieval, *Yuan et al.* (2009) use coplanar measurements to show the fidelity of their wind retrieval, and *Xia et al.* (2012) derive horizontal winds from coplanar measurements under the assumption of a homogeneous wind field.

Figures 5.5 and 5.6 show results of two exemplary coplanar wind measurements on 19 January 2012 and 19 November 2009.

The measurement in January 2012 (see Fig. 5.5) lasted 2.25 h. The vertical wind measurements from 24 and 28 January are used for atmospheric calibration. Obvious are the low and warm stratopause (275 K at 40 km altitude) and the strong westward winds (≈ -60 m/s at 55 km altitude). This is caused by an SSW, which occurred on 17 January (*Chandran et al.*, 2013; *Matthias et al.*, 2013). Both wind speed profiles show similar shapes above 40 km altitude; the differences below 40 km are probably caused by concatenation of count rate profiles of different detectors. The wind speed profiles are shifted only slightly against each other: Mean differences are 5.7 m/s and 8.5 m/s in the altitude ranges 40–50 km and 50–60 km, respectively (the measurement uncertainties in these altitudes are about 5–8 m/s). Therefore, both wind speed profiles agree within the respective measurement uncertainties, which demonstrates the capability of DoRIS to derive reliable wind speeds. This is also backed by wind speed profiles from ECMWF, which agree with the measured wind speed profiles.

The measurement on 19 November 2009 (see Fig. 5.6(a)) lasted nearly 2 h. Since there are no vertical wind measurements in winter 2009/10, internal calibration is used for this measurement. On first view, zonal winds derived by NWT and SET do not match: NWT wind is stronger and SET wind is weaker. At 50 km altitude the difference is ≈ 30 m/s, at 70 km altitude even ≈ 55 m/s, this yields horizontal wind gradients of about 1 m/s km $^{-1}$. Both wind speed profiles show pronounced wave-like structures. Altitude profiles of zonal wind from ECMWF data are between both. The ECMWF profiles show large temporal variability, increasing with altitude: the topmost value is 65 m/s, 35 m/s, and 5 m/s for the 18 UT, 0 UT, and 6 UT profile, respectively. It looks like the NWT profile is tilted toward higher wind speeds

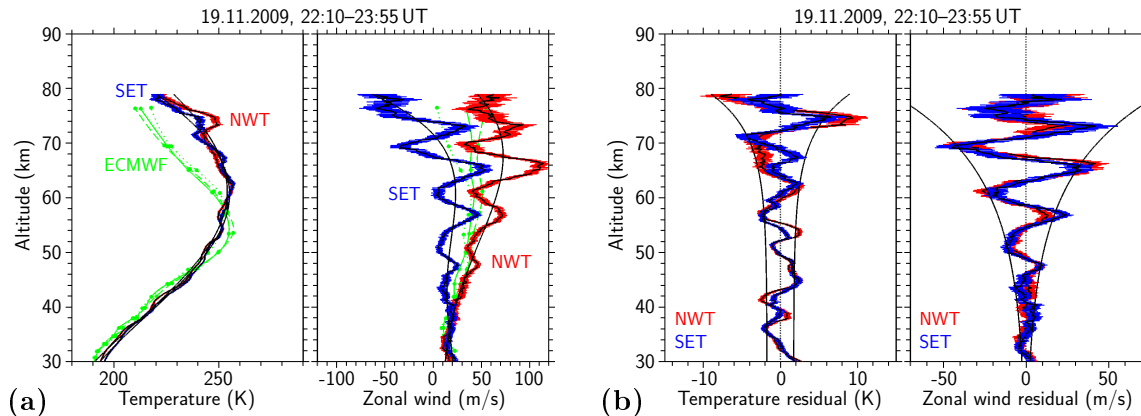


Figure 5.6 Coplanar zonal wind measurement on 19.11.2009. **(a)** Altitude profiles of temperature (left panel) and zonal wind speed (right panel) measured by NWT (red error bars) and SET (blue error bars); green lines show ECMWF data for 18 UT (dashed), 0 UT (solid), and 6 UT (dotted); black lines show polynomial approximation of undisturbed background state. **(b)** Altitude profiles of temperature (left panel) and zonal wind speed (right panel) residuals; black lines show envelope indicating exponential increase of the perturbation amplitude. See text for details.

and the SET profile tilted toward lower wind speeds, relative to the ECMWF profiles. One possible reason for the tilting of the measured wind speed profiles might be a misbehavior of the rotary fiber selector, which would lead to an altitude dependence of backscatter signal. This is discussed below. The temperature and wind speed panels include also polynomial approximations to the measured data (black lines). These fourth-order polynomials shall represent the undisturbed background profiles. Figure 5.6(b) shows the residual profiles for temperature and wind speed, i.e., the background profiles are subtracted from the actually measured profiles. These highlight the wavy structures. The wave-like structures are very similar for NWT and SET, concerning amplitude and altitude of extrema. The mean vertical wavelength is ≈ 7.2 km for temperature and ≈ 8.3 km for zonal wind speed. Note, that the wavelength of temperature residuals shows some stretching between 45 km and 51 km altitude, and between 57 km and 62 km altitude. The wave amplitude increases with altitude, which is typical for upward propagating gravity waves (*Fritts and Alexander, 2003*). The exponential increase can be approximated with an envelope of the form

$$\tilde{X} = a + e^{(z-b)/H_{\tilde{X}}}, \quad (5.1)$$

where \tilde{X} denotes the amplitude of either temperature residual or zonal wind residual, $H_{\tilde{X}}$ is the respective amplitude scale height (which should be twice as large as the pressure scale height (*Fritts and Alexander, 2003*)); the parameters a and b take into account that the wave might start with a certain amplitude a and the exponential growth might start at a certain altitude $\approx b$. The resultant envelopes are indicated by black lines in Fig. 5.6(b). For the temperature residuals the increase of the amplitude is quite small below 60 km altitude. The deduced parameters are: $a = 1.73$ K, $b = 64.31$ km, and $H_{\tilde{T}} = 7.40$ km. Hence, the amplitude scale height is on the same order as the pressure scale height of ≈ 7 km. For the zonal wind speed residuals the increase of the amplitude is more uniform, the deduced parameters are $a = -0.16$ m/s, $b = 16.25$ km, and $H_{\tilde{u}} = 14.26$ km. Hence, the amplitude scale height is

twice as large as the pressure scale height, as expected. The large differences of a and b for temperature and zonal wind are due to large differences in the amplitude growth rates at low altitudes. Differences between the scale heights $H_{\bar{T}}$ and $H_{\bar{u}}$ were also found by *Kaifler* (2009) in a study concerning temperature and wind perturbations within the Na layer. For stand-alone measurements of temperature or wind perturbations, one would explain variations of the respective $H_{\bar{X}}$ by different damping of a wave. But for simultaneous wind and temperature measurements it is hard to explain why a wave should be damped differently in temperature and wind. Probably the pronounced wave-like structure results from the superposition of various waves. This would also explain the above-mentioned stretching of the vertical wavelength of the temperature residuals.

Table D.3 lists all nighttime coplanar measurements of the ALOMAR RMR lidar with duration of at least 1 h. The table includes the mean difference $\langle u_{\text{NWT}} - u_{\text{SET}} \rangle|_{z_1-z_2}$ of both wind speed profiles in certain altitude ranges as a measure for wind speed profile agreement. The agreement of both wind speed profiles is quite good in January and March 2009, and in January 2012. In November 2009 the comparison is good for the first measurement on 17./18.11.2009, but bad for the following measurements.

The poor matching in November 2009 was probably caused by misbehavior of the rotary fiber selector (RFS). A misalignment between its mirror surface and its plane of rotation can cause angular deviations of the beam toward the detector (*Hildebrand et al., 2012*). These are converted by the long optical path (≈ 4 m between RFS and detectors) in combination with the small detector area (≈ 0.024 mm²) into beam displacements at the detectors that cause small signal variations. The impact of an unstable RFS is demonstrated in App. B.1.

5.2.3 Combination with the ALOMAR sodium lidar

The ALOMAR observatory hosts a further lidar instrument which is capable to measure wind speeds in the middle atmosphere: the ALOMAR sodium lidar. This lidar covers the altitude range from about 80 to about 110 km. Since both lidars share the same receiving telescopes, they sound a common volume in the height range of overlap. This height range (≈ 80 – 85 km) is quite small and the respective range limit for both instruments: The Na lidars suffers from small Na density, the RMR lidar suffers from small atmospheric density. A joint measurement campaign was performed in January 2009, yielding more than 40 hours of simultaneous observations. Various results of this campaign are published in *Hildebrand et al. (2012)*.

The observations from the night 26/27 January 2009 will be presented in the following, since they cover a longer period and show the agreement of both instruments on long and short time scales. This simultaneous measurement lasted from 16:35 UT on 26 January until 03:00 UT on 27 January, thus for nearly ten and a half hours.

Figure 5.7 shows the integrated altitude profiles of zonal wind speed measured by RMR and Na lidar. The independently derived wind speeds match nicely in large part of the height range of overlap (79–83 km). The mean zonal wind speeds in the height range of overlap are (-1 ± 8) m/s and (-5 ± 1) m/s for RMR and Na lidar, respectively. Wavy structures are visible in lidar data and also in the included profiles of ECMWF data. These indicate additional temporal variability.

The temporal evolution of the lidar data is shown in Fig. 5.8. The data are smoothed with a running mean filter with window size of 1 h. The horizontal black line at 77–79 km indicates the transition altitude from RMR lidar to Na lidar data; above only Na lidar data is shown. The right panel shows a close-up between 65 and 85 km altitude, highlighting the transition

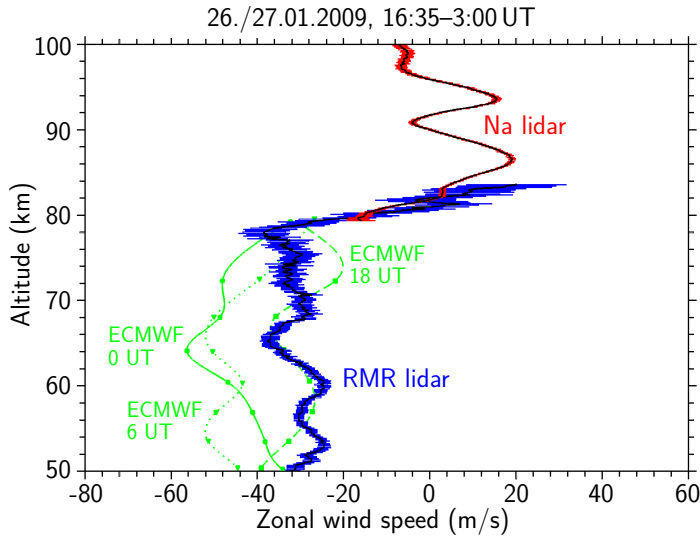


Figure 5.7 Nightly mean altitude profiles of zonal wind speed on 26/27 January 2009 measured by RMR lidar (blue error bars) and Na lidar (red error bars) with the NWT. Integration time is 10.5 h. Green lines show zonal wind speed from ECMWF data for 18 UT (dashed), 0 UT (solid), and 6 UT (dotted). (after *Hildebrand et al. (2012)*)

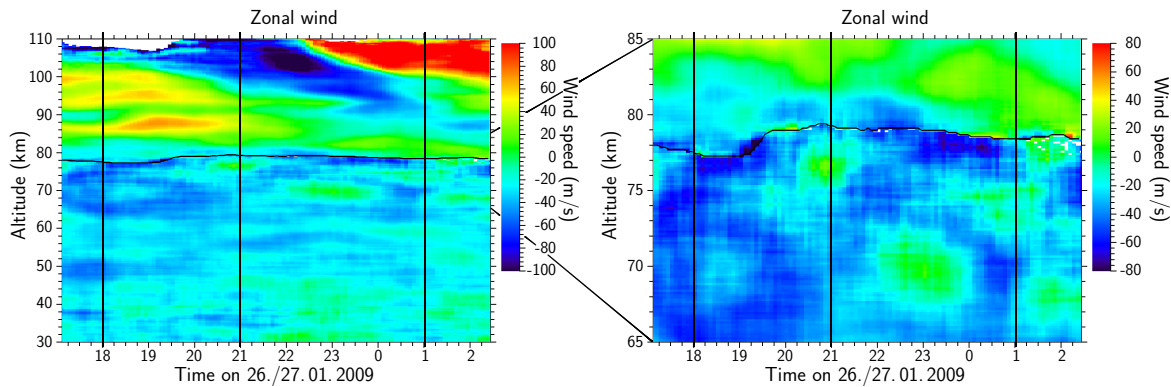


Figure 5.8 Zonal wind speed on 26/27 January 2009 measured by RMR and Na lidar with the NWT. In the height range of overlap (roughly 78–85 km) and above, only wind from Na lidar is shown. Left panel: complete altitude range between 30 and 110 km. Right panel: close-up between 65 and 85 km altitude, highlighting the transition from RMR lidar to Na lidar data at 77–79 km (indicated by black line). Vertical black lines indicate times for which single profiles are shown in Fig. 5.9. (*Hildebrand et al., 2012*)

from RMR to Na lidar data. The transition is smooth most of the time, but there are also some differences of up to 20 m/s (e.g., around 00 UT). Since the measurement uncertainties in this altitude range are $\approx 15\text{--}20$ m/s and ≈ 5 m/s for RMR and Na lidar, respectively, these differences do not falsify the general good agreement. The vertical black lines indicate selected times for which single wind speed profiles are shown in Fig. 5.9. Both lidar wind speeds match well, especially at 18 UT. At 21 UT and 01 UT differences are bigger, but mostly within the error bars. Table 5.2 lists the mean zonal wind speeds measured by RMR lidar and Na lidar in the respective height range of overlap for these selected times. These panels include also wind

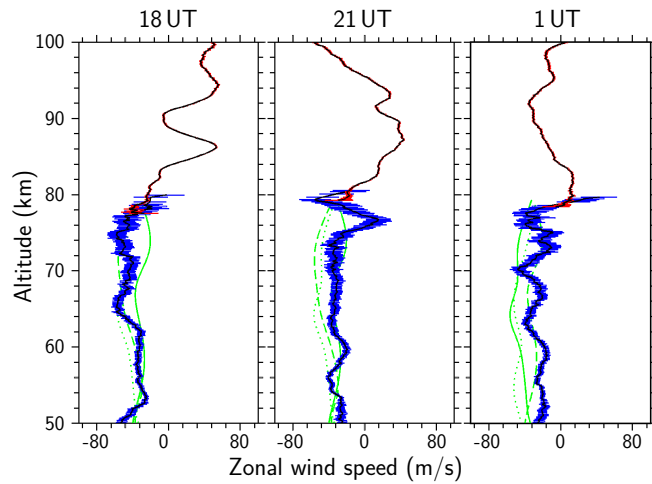


Figure 5.9 Altitude profiles of zonal wind speed on 26/27 January 2009 measured by RMR lidar (blue error bars) and Na lidar (red error bars) with the NWT. Integration time is 1 h. Profiles are centered at 18 UT, 21 UT, and 01 UT. Green lines show wind speed profiles from ECMWF data. (*Hildebrand et al., 2012*)

Table 5.2 Comparison of zonal winds measured by RMR lidar data and Na lidar data

| | 18:00 | 21:00 | 01:00 | 16:35–03:00 |
|------------------------|--------------|--------------|-------------|-------------|
| u_{RMR} (m/s) | -23 ± 17 | -37 ± 18 | 15 ± 18 | -1 ± 8 |
| u_{Na} (m/s) | -31 ± 4 | -20 ± 5 | 6 ± 5 | -5 ± 1 |

speed profiles from ECMWF data. Like in Fig. 5.7 the temporally closest ECMWF profile (solid) differs from the lidar profile. There is no systematic under- or overestimation, it just appears that ECMWF data and lidar data are not in phase with each other.

Chapter 6 Geophysical results

After examination of the quality of the derived wind speeds on selected cases, this chapter presents the whole data set of horizontal winds and compares them to winds measured with co-located radar instruments and winds extracted from models.

While lidar instruments have very narrow fields of view on the order of tens to hundreds microradians, radar instruments probe the atmosphere in much wider sounding volumes. Figure 6.1 compares schematically the sounding volumes of different lidar and radar instruments at ALOMAR. At 85 km altitude, where the altitude ranges of all instruments overlap, the diameters of their sounding volumes differ remarkable (e.g., 15 m for the ALOMAR RMR lidar, 5 km for the Saura MF radar, and 170 km for the SKIYMET radar). These large systematic differences need to be kept in mind when comparing wind speeds derived by lidar and radar. The larger sounding volumes of radars cause a spatial smoothing while the lidar measures at a distinct point in the sky.

For the analysis the lidar data are integrated to profiles of 1 h and cumulated to respective mean profiles. They are limited to measurement uncertainties of $\Delta T < 5\text{K}$ and $\Delta u = \Delta v < 20\text{ m/s}$. Radar data are extracted on corresponding time basis, matching the lidar data as close as possible. For this thesis wind data from the Saura MF, Andenes MF, and SKIYMET radar are available at 2 km (1 km for Saura MF radar) vertical and 30 min temporal resolution (*Hoffmann, 2012; Strelnikova, 2012*).

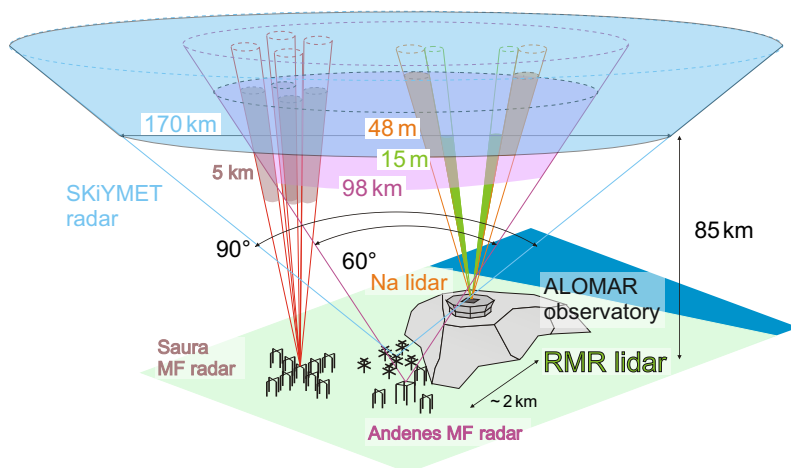


Figure 6.1 Sounding volumes of different lidar and radar instruments, not to scale. The filled parts of the cones indicate the actual sounding volume, the colored numbers their diameters at 85 km altitude. Blue: SKIYMET radar, pink: Andenes MF radar, grayish/red: Saura MF radar, green: ALOMAR RMR lidar, orange: ALOMAR Na lidar.

The ECMWF provides an operational forecast model (Integrated Forecast System, IFS) which assimilates real data. The wind and temperature data shown in this thesis are extracted from IFS cycle Cy36r1, horizontal resolution T1279, for 69.28°N, 16.01°E. These data are available as snapshots for every six hours.

The HWM07 is an empirical model which accumulates data from 35 different instruments (remote sensing and in-situ techniques) obtained over fifty years (*Drob et al.*, 2008). The HWM07 does not incorporate any year-to-year variability. Wind data used in this thesis are extracted on hourly basis for the location 69.3°N, 16.0°E. The observation data used in HWM07 for this location and nighttime base mainly on rocket campaigns (see Tab. 1 in *Drob et al.* (2008)).

6.1 Monthly mean winds and temperatures in Arctic winter

As mentioned in Sect. 5.1 only winds measured during the winter months November until March are considered. Figure 6.2 presents, exemplary for the months January, February, and November, averaged altitude profiles of temperature, zonal wind, and meridional wind cumulated over the years 2009 to 2012. Data for all months are presented in App. D.3.1.

Lidar data are shown in red. The temperature panels include model data from ECMWF, published data from earlier lidar measurements at ALOMAR (*Schöch et al.* (2008); hereinafter referred to as *Scho8*), and data from falling sphere measurements at Andøya Rocket Range (*Lübken and von Zahn* (1991); hereinafter referred to as *LvZ91*). The wind speed panels include model data from ECMWF and HWM07, radar data from Saura MF radar, Andenes MF radar, and SKIYMET radar, and for some months data derived by meteorological rockets and radars over northern Scandinavia (*Meyer et al.* (1987); hereinafter referred to as *Mey87*). Dotted lines indicate the respective standard deviation (if available). All these profiles (except for *Scho8*, *LvZ91*, and *Mey87*) are limited to altitude ranges where at least half of the respective single profiles contribute data (i.e., if there are only four of ten single profiles having data in a certain altitude range, this altitude range is excluded in the mean profile). This means that single profiles cover larger altitude ranges, but these would not be representative. The respective number of single lidar profiles included in each panel is indicated in the upper left corner of each figure. In most cases this value is also representative for the model and the radar data; in some cases less radar profiles are included (e.g., there are no Saura MF radar profiles in January 2009).

On first view we see for the temperatures some month-to-month variation and, especially in January and February, large variability within single months. The large variability in January and February is caused by SSW. Mean temperatures derived by lidar are in most cases several Kelvin higher than ECMWF temperatures. Typically the lidar temperatures are ≈ 5 K higher below ≈ 50 km altitude and above ≈ 65 km altitude, between the lidar temperatures are about 5 K smaller; for November the difference exceeds 20 K above 70 km altitude (the lidar temperatures are backed by *Scho8* and *LvZ91*). Such differences between temperatures derived by lidar and provided by ECMWF were discussed previously by *Scho8*. At the stratopause altitude mean zonal wind is eastward during all months. It is strongest in December (see Fig. D.1(b)), indicating a well established polar vortex. The highest variability in zonal wind occurs in January and February, likely caused by SSW. These will be discussed below. The mean meridional winds are weaker than zonal winds. There is no single predominant distinct direction: e.g., in November the mean meridional wind is southward, it is northward in January and close to zero in March (Fig. D.1(e)). There are some differences between mean winds derived by lidar and other data sets.

6.1 Monthly mean winds and temperatures in Arctic winter

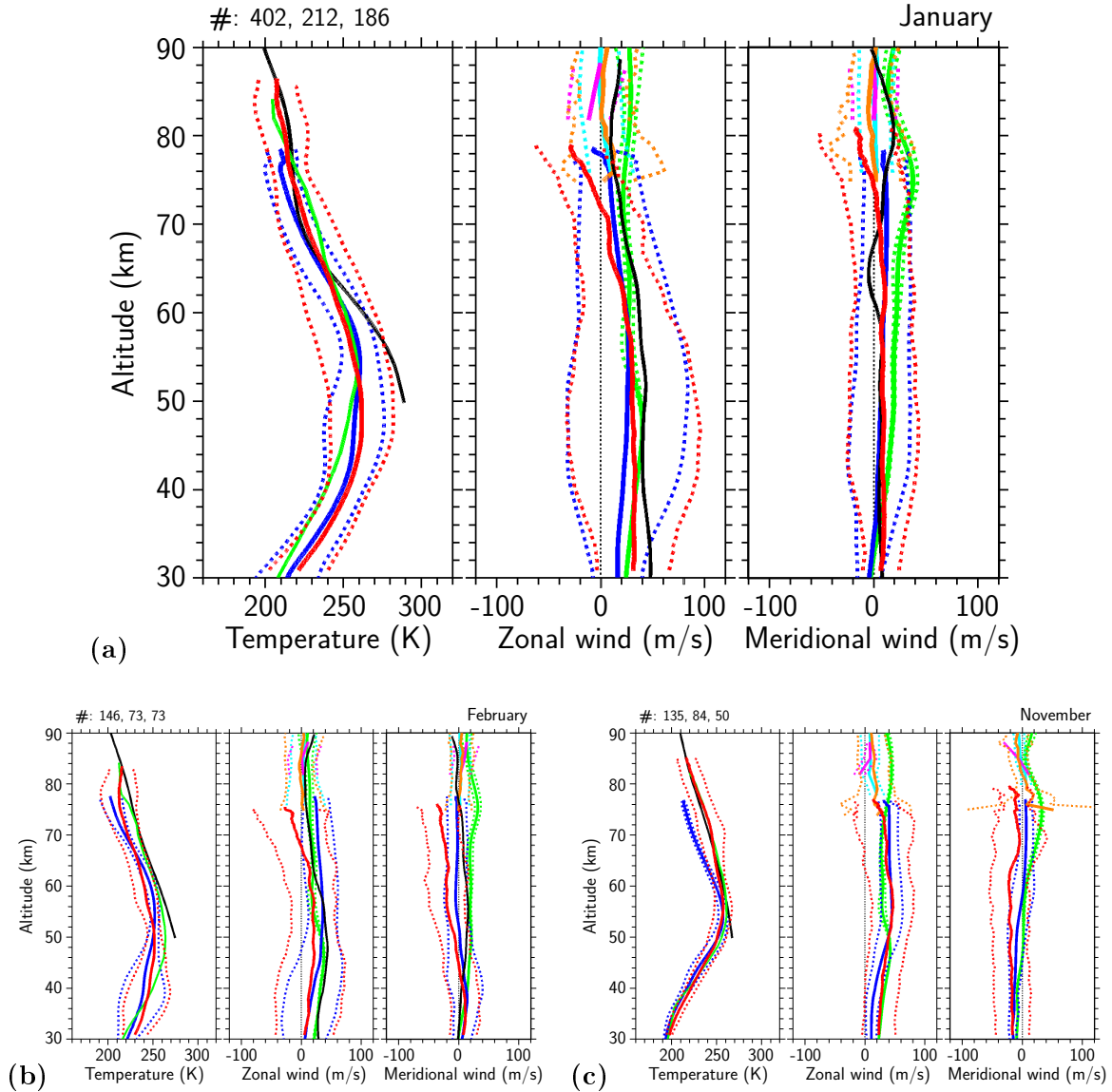


Figure 6.2 Over the years 2009–2012 cumulated monthly mean temperatures and horizontal winds for the months January (a), February (b), and November (c). Red: ALOMAR RMR lidar, orange: Saura MF radar, cyan: Andenes MF radar, magenta: SKiYMET radar, blue: ECMWF, green: *Scho8* for temperatures, *HWM07* for winds, black: meteorological rockets (*LvZ91* for temperatures, *Mey87* for winds). Dotted lines denote the respective standard deviation. The three numbers in the upper left corner indicate the number of lidar profiles included in the panels for temperature, zonal wind speed, and meridional wind speed, respectively.

The data set from *Mey87* is in that way notably, as it contains data from one season only. Due to geophysical variability (see Sect. 6.2) these data are not expected to always match to other data sets. This note applies also to the data sets from *Scho8* and *LvZ91*, albeit both contain data from several years.

6.1.1 Comparison to other wind data sets

The monthly mean winds derived by lidar are now compared to winds from ECMWF and HWM07 models, and to winds measured by radar. The discussion is restricted to the months January, February, and November, which are presented in Fig. 6.2. Similar figures and short discussions for the months March and December are presented in App. D.3.1. Mean winds for every single month of every single year are presented in App. D.3.2.

For the comparison of wind speeds the terms “smaller” and “larger” will be used for values including algebraic sign (i.e., -40 m/s is smaller than 20 m/s although wind is stronger).

January, Fig. 6.2(a) and Fig. 6.3 The zonal wind measured by lidar matches ECMWF data, except below 42 km altitude and above 70 km altitude, differences are up to 20 m/s. The lower part might be affected by improper catenation of count rates of single detectors to one profile per channel (see App. A for details). The behavior in the upper part is seen also in data of 2010 and 2011, while in 2009 the lidar wind is too large, but matches ECMWF and radar profiles perfectly in 2012 (Fig. D.5(a)). The meridional wind derived by lidar matches the ECMWF profile, only below 35 and above 75 km altitude there are slight differences up to 10 m/s. In 2012 the comparison is perfect (Fig. D.5(a)), but not good in 2010 and 2011.

February, Fig. 6.2(b) The zonal wind derived by lidar is too small compared to ECMWF data in the entire altitude range (the difference is 10 m/s at 40 km altitude and 20 m/s at 60 km). This is due to the majority of data from 2010 (46 profiles). In 2009 and 2012 mean lidar winds match better to ECMWF wind (Figs. D.2(b) and D.5(b)), differences are about 10 m/s. The mean meridional wind measured by lidar is too small compared to ECMWF data, especially above 50 km altitude (the difference is 20 ms at 60 km altitude). Again, this is due to numerous measurements in 2010; while data from 2012 (3 profiles) match very well to ECMWF (differences of about 5 m/s) below 60 km altitude and to radar data above (Fig. D.5(b)).

November, Fig. 6.2(c) The zonal wind derived by lidar matches ECMWF data, except below 45 km altitude and above 70 km altitude (differences up to about 10 m/s). In the upper part the comparison to radar data is better for lidar than for ECMWF data; hence, the lidar wind is not thought to be false; this is especially true for 2010, when the difference between lidar and ECMWF is largest (up to 40 m/s at 70 km altitude). The meridional wind measured by lidar is too small compared to ECMWF in the entire altitude range (the differences range up to 25 m/s at 60 km altitude). Most of the data (42 profiles) was acquired in 2009, when the RFS was probably working bad (see Sect. 5.2.2). Seven of the remaining profiles were obtained in 2010 and show good comparison to ECMWF data (differences are less than 5 m/s) below 50 km altitude (see Fig. D.3(d)), above 50 km the lidar wind shows strong wave activity, which is not resolved by ECMWF data.

Summary/Conclusion In general, the horizontal winds measured by lidar and from other data sets are agree. There are some differences, especially at the upper and lower altitude limits of the lidar wind retrieval.

Part of these differences can be attributed to instrumental effects, which had been identified since the DORIS setup is in operation and most of them are solved now. These effects include the RFS, the frequency stability of the emitted laser light, and the determination of the detection efficiency ratio of the detectors. Some misbehavior of the RFS was identified in

February 2009, which probably persisted more or less pronounced until the RFS was replaced in summer 2011. The frequency of laser 1 showed some jitter or 2-mode behavior between November 2010 and January 2011 and between November 2011 and March 2012. As long as this jitter is on time scales of several minutes it can be taken into account easily. But when the laser operates on two modes quasi simultaneously, a more sophisticated effort is needed to take this into account. The quality of the seeder Doppler ratio is determined by the strength of the seed laser light that is feed into the detection system and probably also by its behavior regarding its polarization. During 2009 and beginning of 2010 some short scale fluctuations of the seeder Doppler ratio were observed, which falsely look like short scale variations of the detection efficiency ratio. By increasing the intensity of the seed laser light and installing a polarization filter at the seed laser branch of the detection system the quality of the seeder Doppler ratio was enhanced.

Besides these instrumental effects the observed variability during each month is about 2–6 times larger than the measurement uncertainty. To investigate to what extent this variability is caused by geophysics, we now concentrate on January observations.

6.2 Variability in winds and temperatures in January

Since January is the month with most measurement hours (see Fig. 5.1) and shows high variability in temperature and horizontal winds (see Fig. 6.2(a)), we focus on that month for a more detailed analysis. Figure 6.3 shows mean temperatures, zonal, and meridional winds for each January of the years 2009 (panel (a)) to 2012 (panel (d)). These plots include the same data sets as Fig. 6.2. Again, the data set from meteorological rockets might not be representative, as stated above. The HWM07 data set includes no year-to-year variability. However, the HWM07 profiles in Fig. 6.3 may differ slightly from year to year, this is due to different sampling for each year. Due to the not incorporated year-to-year variability the HWM07 data is not expected to always match to other data sets, but it is regarded as representation of the climatological mean state.

January 2009, Fig. 6.3(a) On 22 January 2009 a very strong SSW occurred (*Matthias et al.*, 2013). During the temporal evolution of an SSW the stratopause sinks. This explains the relatively high temperatures below 40 km altitude and the low temperatures above (compared to Fig. 6.2(a)). The comparison to ECMWF data is poor above 50 km altitude. A poor comparison between lidar temperatures and ECMWF temperatures during winter was discussed previously by *Schöch et al.* (2008). The mean zonal wind is westward, due to the distortion of the polar vortex. This distortion is also visible in meridional wind: Contrary to the normal situation (represented by HWM07) the mean meridional wind is southward with mean wind speed of up to -40 m/s at 42 km altitude.

January 2010, Fig. 6.3(b) Noticeable is the strong variability of zonal wind, particularly around the stratopause altitude, while the temperature variability is quite small. Also meridional wind shows only small variability. The altitude range of enhanced zonal wind variability corresponds to the stratopause altitude. Mean zonal and meridional winds of all data sets match fine with each other. During the second half of this month measurements were performed on two of three days, i.e., the sampling is very good.

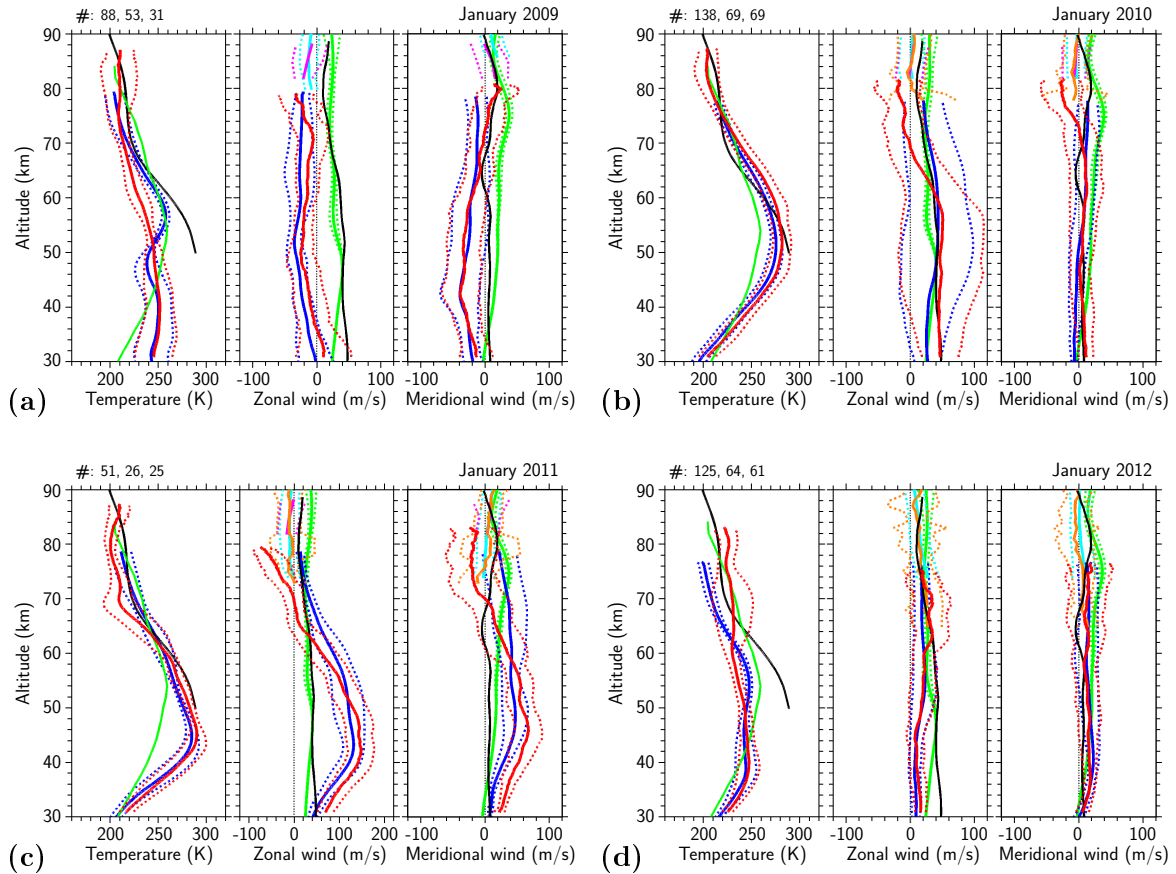


Figure 6.3 January mean temperatures and horizontal winds for the years 2009 to 2012. Red: ALOMAR RMR lidar, orange: Saura MF radar, cyan: Andenes MF radar, magenta: SKIYMET radar, blue: ECMWF, green: HWM07, black: meteorological rockets *Mey87*. Note the different scaling of zonal wind speed in (c).

January 2011, Fig. 6.3(c) Mean profiles of this month show strikingly strong winds and high stratopause temperature. The zonal wind shows a very strong eastward jet at stratopause level (note the different scaling), meridional wind is strong northward. Above 70 km both wind components reverse to westward and southward wind, respectively. The mean stratopause temperature is 290 K. These data were obtained during three days only (10., 12., and 13.01.2011), so they are not representative for whole January. This period was not classified as SSW, but nevertheless the polar vortex was displaced. This resulted in relatively warm air above ALOMAR/northern Scandinavia and the zone of highest wind speeds passing above ALOMAR.

January 2012, Fig. 6.3(d) The mean temperature profile shows a low and cold stratopause, mesospheric temperature around 70 km altitude is relative high and shows large variability. Zonal and meridional wind are quite weak eastward and northward, respectively. On 17.01.2012 a minor SSW occurred (*Chandran et al., 2013; Matthias et al., 2013*). The subsequent temporal evolution of the thermal structure of the middle atmosphere explains the large temperature variability around 38 km altitude and between 62 and 74 km altitude.

6.2 Variability in winds and temperatures in January

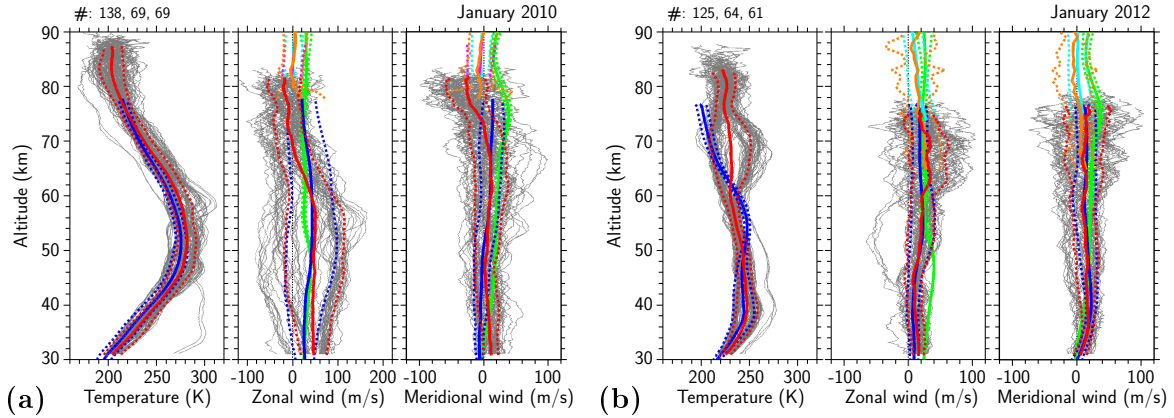


Figure 6.4 Single altitude profiles of temperatures and horizontal winds in January 2010 and 2012. Shown are all profiles with temporal integration of 1 h. Gray: single lidar data, red: mean lidar data, orange: Saura MF radar, cyan: Andenes MF radar, magenta: SKiYMET radar, blue: ECMWF, green: HWM07. Note the different scaling of zonal wind speed in (a).

During the last twelve days of this month data were obtained on eight days, this allows investigating the temporal evolution following the SSW. This will be shown in Sect. 6.2.1.

Summary/Conclusion Considering only these four years, large variability in temperature and wind is observed: Comparing 2009 and 2012, the temperature profiles are similar (compared to 2010 or 2011), but the profiles of zonal and meridional wind differ remarkably; in 2010 the zonal wind shows very large variability while the temperature does not; contrary in 2012 temperature shows large variability while the zonal wind does not. Hence, sounding temperature only does not provide a comprehensive picture of the actual state of the atmosphere, especially regarding its dynamics.

6.2.1 January 2010 and January 2012

We focus now on January of 2010 and 2012. Both are the months with most measurement hours and show some interesting features in the respective mean profiles: While in 2010 there is large variability in zonal wind, but only small in temperature, 2012 exhibits larger variability in mesosphere temperature, but only weak variability in zonal wind.

Single altitude profiles (1 h temporal integration) of temperature and horizontal wind are shown in Fig. 6.4. It is striking that in 2010 (panel (a)) zonal wind shows great variability (note the different scaling) while the temperature does not (except two profiles from 30.01.2010 for which the temperature differs from the other profiles below 45 km altitude and above 60 km altitude), and in 2012 (panel (b)) the temperature shows great variability while the zonal wind does not (except three profiles from 19.01.2012 that show enhanced westward wind).

In 2010 three groups in zonal wind can be distinguished: strong eastward wind (largest group); strong westward wind; and an intermediate state with transition from eastward to westward wind. Contrary, in 2012 three groups in temperature can be distinguished: Three profiles show enhanced temperature below 55 km altitude, a second group shows temperature enhancement between about 62 and 74 km altitude, and the remaining profiles as third group.

Zonal wind variability in January 2010

The measurements shown in Fig. 6.4(a) are now split into three groups, corresponding to zonal wind. This is shown in Fig. 6.5: The left column shows the altitude profiles for each group, corresponding polar maps of horizontal wind are shown in the right column. The polar maps are extracted from ECMWF data at the 1 hPa pressure level (≈ 45 km altitude). In general the comparison of lidar data and ECMWF data and radar data is good for all of the presented cases. There is some difference for the first period between ECMWF and lidar data, but at around 80 km altitude the lidar data and the radar data compare well. For the third period, there is some difference at the meridional wind panel between lidar wind and ECMWF wind, but radar wind and lidar wind match well. Since there were no vertical wind measurements during January 2010, the derived winds rely on internal calibration. On 30.01.2010 a slightly unusual low seeder Doppler ratio was identified, resulting in too small horizontal winds; to take this into account an additional correction factor (see Eq. (4.10)) was applied.

The first group (panel (a)) contains data from 14.–18.01.2010. Zonal wind is strongly eastward up to about 70 km altitude and calm above. Meridional winds are weak, mainly northward. Temperatures reach up to 310 K, the altitude of highest temperature varies between 46 and 60 km. The zonal wind is strongest in the same altitude range. As the vortex map from 15 January (panel (b)) shows, the inner edge of the polar vortex is above ALOMAR (indicated by colored dot). This explains the very strong eastward winds. The second group (panel (c)) contains data from 20.–22.01.2010. As can be seen in panel (d), the polar vortex is deformed and displaced, its center is above ALOMAR. Hence, horizontal winds are weak. The stratopause altitude is constantly 50 km, maximum temperatures are about 290 K. The third group (panel (e)) contains data from 24., 25., and 30.01.2010. On 28.01.2010 a major SSW occurred (*Matthias et al.*, 2013). The zonal wind is westward below 70 km altitude, with strongest winds at about 45 km altitude. Meridional winds are northward above 55 km altitude (the profile with remarkable negative meridional wind is from 30.01., see above). The vortex map (panel (f)) shows that the remains of the polar vortex are displaced further south. Now the opposite inner edge is above ALOMAR, resulting in westward wind. This third group is characterized by homogeneous westward wind, but shows remarkable variability in temperature. Two profiles (30.01.) show the consequence of the SSW: an unusual warm and low stratopause and low temperatures in the mesosphere. The profiles from 24./25.01. show the stratopause at normal altitudes around 50 km and a second temperature maximum at about 64 km altitude.

Temperature variability in January 2012

The measurements from January 2012, shown in Fig. 6.4(b), are now split in three groups, corresponding to temperature. This is shown in Fig. 6.6, and additionally data from early February 2012. Note the exceptional good comparison of winds derived by lidar, radar, and from ECMWF data. Especially in panel (c), where the wind data from Saura MF radar reaches down to 60 km altitude (due to a solar proton event on 27./28.01.2012 (*Space Weather Prediction Center*, 2013)).

On 17.01.2012 a minor SSW occurred. Figure 6.6 depicts the subsequent temporal evolution until 4 February 2012. On 19.01.2012 (panel (a)) the stratopause is just below 40 km altitude, and there is a second temperature maximum ≈ 7 km above; the temperature is 275 K and ≈ 270 K, respectively. Zonal wind is westward and meridional wind is southward, likely due

6.2 Variability in winds and temperatures in January

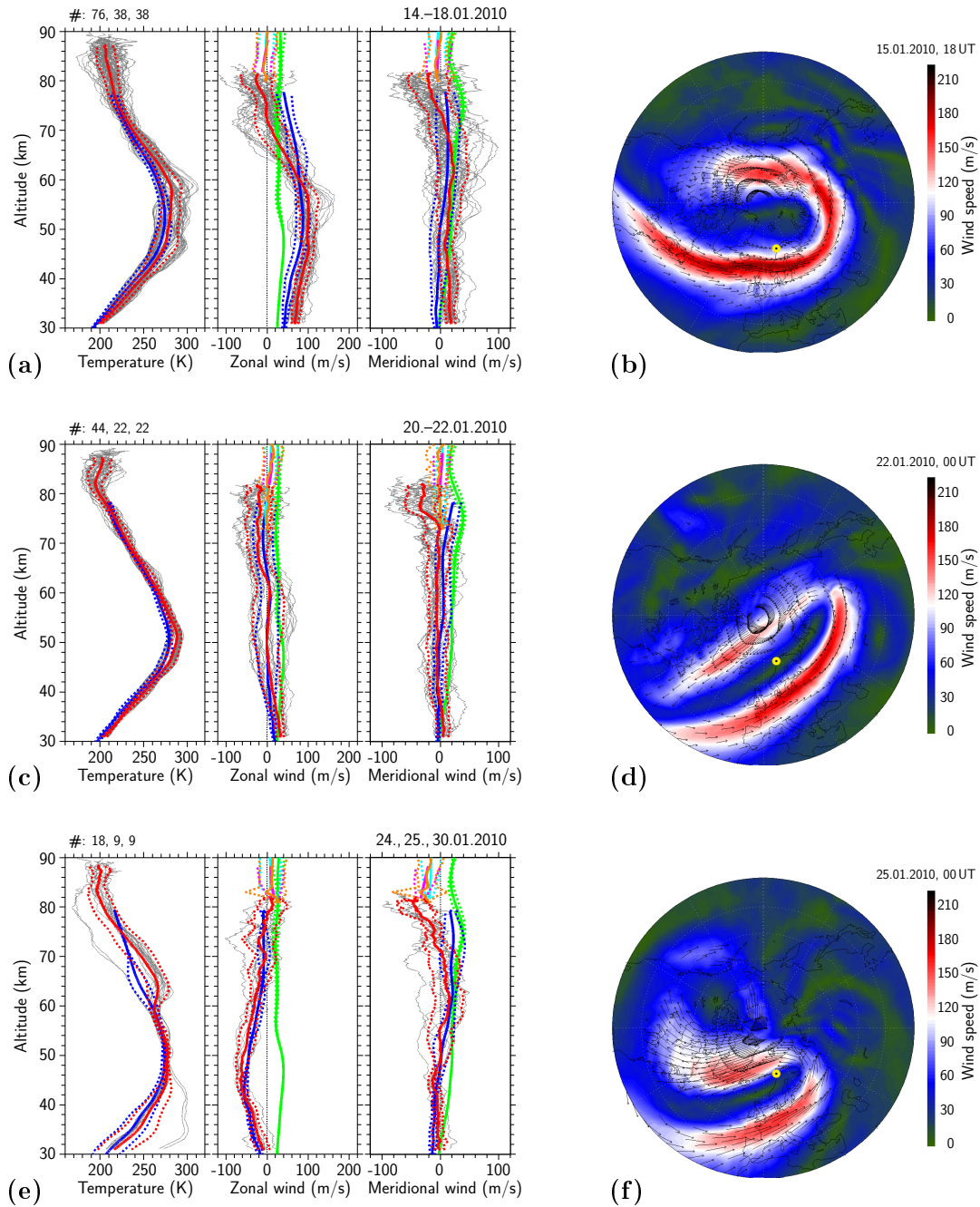


Figure 6.5 Temperatures, horizontal winds, and polar vortex during January 2010. Colored lines like in Fig. 6.4. (a) single lidar profiles from 14.-18.01.2010; (b) polar map of horizontal wind at 1 hPa level from ECMWF data for 15.01.2010, 18 UT; (c) single lidar profiles from 20.-22.01.2010; (d) like (b) but for 22.01.2010, 00 UT; (e) single lidar profiles from 24., 25., and 30.01.2010; (f) like (b) but for 25.01.2010, 00 UT.

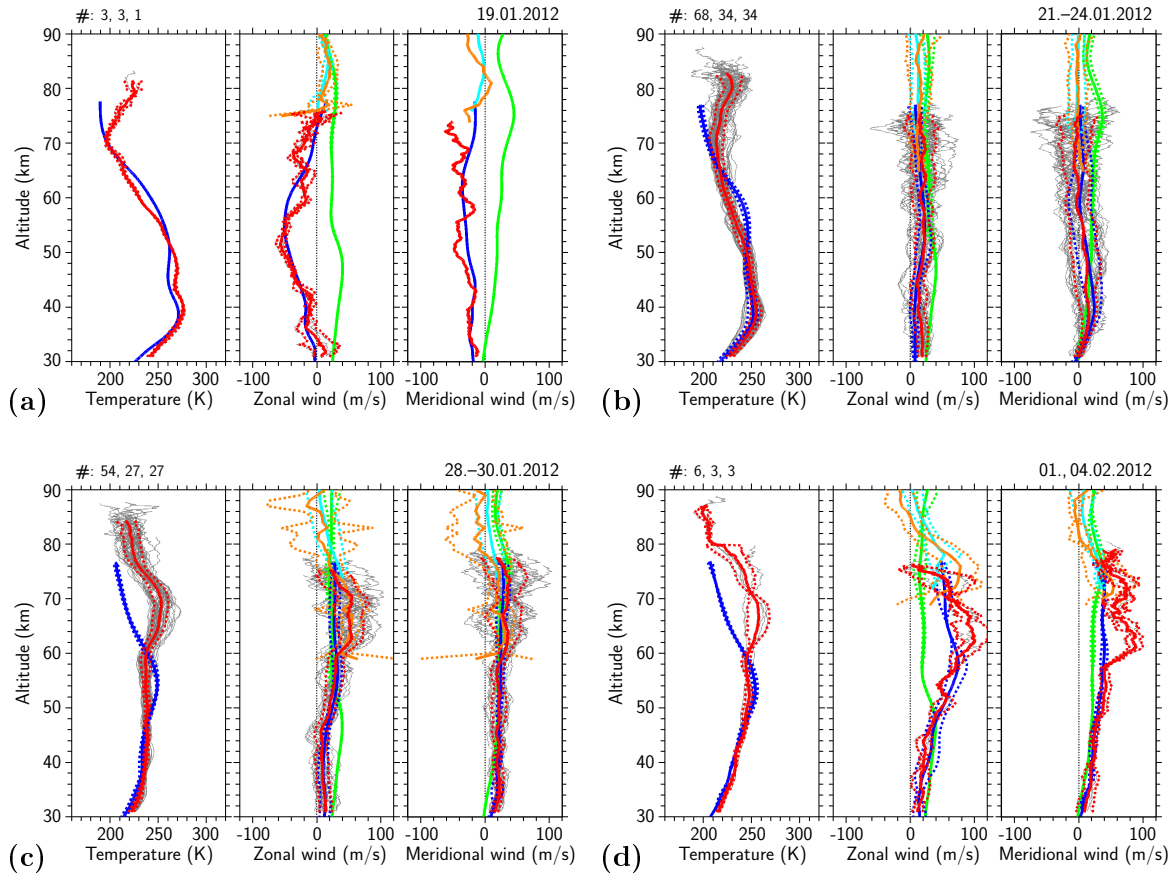


Figure 6.6 Temperatures and horizontal winds during January and February 2012. Colored lines like in Fig. 6.4. (a) single lidar profiles from 19.01.2012; (b) single lidar profiles from 21.-24.01.2012; (c) single lidar profiles from 28.-30.01.2012; (d) single lidar profiles from 01. and 04.02.2012.

to the ssw. The data from 21. to 24.01.2012 (panel (b)) show a cooling of the stratopause: Maximum temperatures are now 260 K. Zonal winds are weakly eastward over the entire altitude range. Meridional winds vary between -40 m/s and $+40$ m/s. Most of these data were obtained during one continuous long measurement which is addressed in a detailed study in Sect. 6.3. On 28.-30.01.2012 (panel (c)) the temperature maximum at 40 km altitude vanished, but highest temperatures of up to 270 K occur at around 70 km altitude. In nearly the same altitude range like the temperature maximum the zonal wind is stronger eastward (between 60 and 74 km altitude) and the meridional wind has enhanced variability (above 60 km altitude), with a node at 70 km altitude. Data from early February 2012 (panel (d)) show the highest temperatures a few kilometers below. The altitude of highest zonal and meridional winds decreases as well.

Summary/Conclusion

Comparison of data from January 2010 and 2012 shows, that variability in temperature and wind are not linked to each other. The data from 2010 were split into three groups based on different zonal wind characteristics. Despite the different zonal wind characteristics temper-

atures looked similar (except the last group which was influenced by an SSW). Contrary, in January 2012 more variability in temperature than in zonal wind was observed (especially when comparing the data from 21.–24.01. and 28.–30.01.).

The data from January 2012 revealed the temporal evolution of the vertical temperature and wind structure subsequent to a minor SSW with the formation of an elevated stratopause and enhanced eastward winds at the same altitude range about ten days after the SSW. During the next days the elevated stratopause and also the zonal and meridional wind maxima decreased in altitude. *Labitzke (1972)* discussed such increased mesospheric temperatures at high altitudes after the breakdown of the polar vortex during a major SSW. *Manney et al. (2009)* denoted the high temperatures and enhanced eastward winds (derived from geopotential heights) as reforming of the stratopause and the polar vortex at these altitudes after a major SSW. On the basis of the SSW in January 2012 as an example, *Chandran et al. (2013)* stated that such an elevated stratopause can also appear after a minor SSW. Above 40 km altitude this SSW behaved like a major SSW; but the wind reversal did not reach the 10 hPa pressure level, hence, it was classified as a minor SSW (*Chandran et al., 2013*).

For a comprehensive understanding of atmospheric dynamics temperature and wind measurements are needed. Taking only temperature or only wind measurements into account would not reveal different dynamic patterns.

6.3 Case study – gravity waves in wind and temperature

As mentioned above the data from 21 to 23 January 2012 were obtained during one long continuous measurement. It is the longest measurement of the whole data set of winter data, it lasts for nearly sixty hours. Not only its long duration is exceptional, but also that it reveals very pronounced wave structures in temperature and wind data. In order to investigate the temporal evolution of the background state of the atmosphere and its disturbances, daylight data is included in the analysis. This shows also the daylight capability of the wind retrieval.

To analyze the data atmospheric calibrations determined during vertical wind measurements are used. During the first night the bypass of the daylight filter was mounted improperly (see Fig. 4.14), which raises some difficulties when analyzing the wind data (see Sect. 4.4.4). To take this into account a correction factor C_E was applied on the measured Doppler ratio (see Eq. (4.10)).

Figure 6.7 shows time-height sections of temperature, zonal, and meridional wind speed, and the respective mean profiles. The data are smoothed with a running mean filter with window size of 1 h and 3 km, respectively. The temperature data are the average of both lasers/telescopes. The reduced top altitude around noon is caused by increased solar background during day. Data is rejected when the measurement uncertainty exceeds 5 K or 20 m/s for temperature and horizontal wind, respectively. The temperature data start 25 min earlier than the horizontal wind data since there was a vertical wind measurement at the beginning. During the first night (21./22.01.) the top altitude is lower than during the second night (22./23.01.). This is caused by the improperly mounted bypass of the daylight filter. During the third day (23.01.) clouds disturbed the measurement, which finally ended in the evening.

Over the three days the stratopause temperature decreased from about 265 K to about 250 K. The stratopause altitude increased slightly from about 38 km to 40 km. The zonal wind is predominantly eastward, its mean value in all altitudes is ≈ 20 m/s. Except the wavy structure, there is no vertical shear in zonal wind. Meridional wind changed from slightly southward winds during the first night to predominant northward winds during the third

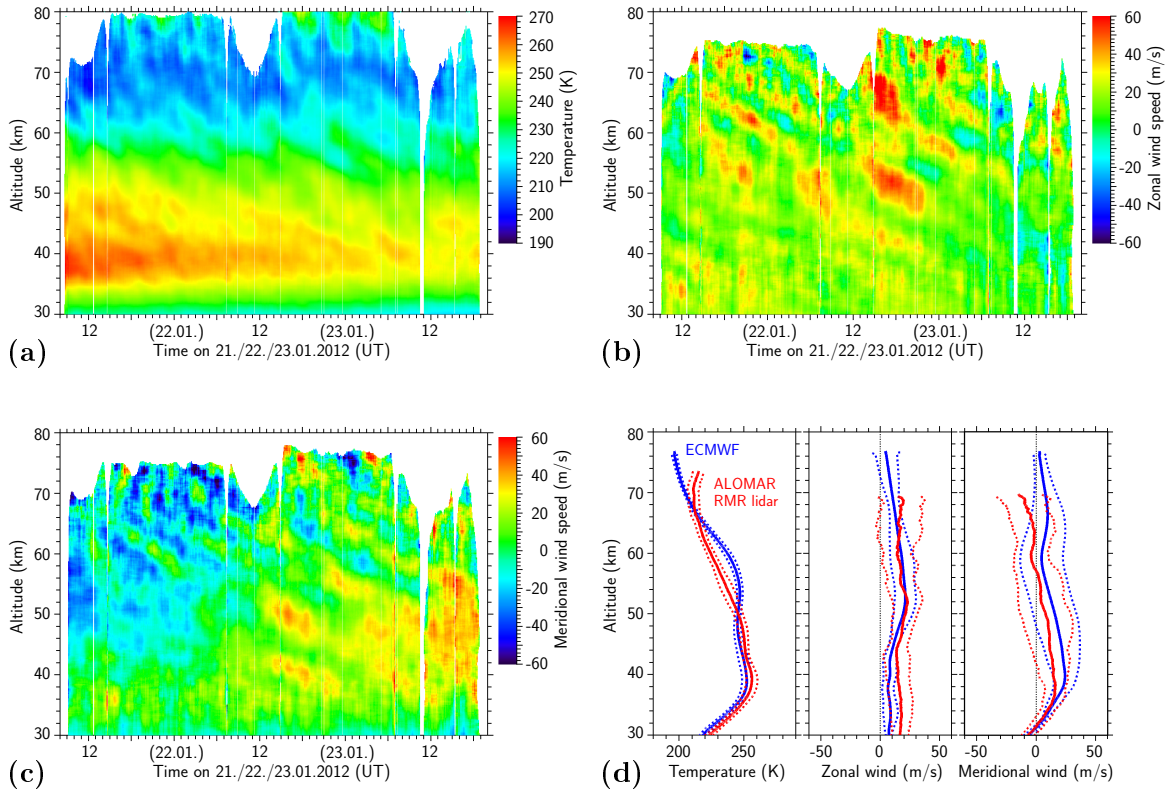


Figure 6.7 Time-height sections of temperature (a), zonal wind (b), and meridional wind (c), and respective mean altitude profiles (d) for 21.–23.01.2012.

day. This results in mean northward wind around the stratopause and weak mean southward wind above about 60 km altitude.

The time-height sections of temperature and wind show some wavy structures, but are dominated by long periodic changes (e.g., the increasing meridional wind) or pronounced vertical variations (e.g., dominant stratopause in temperature). To emphasize the wavy structures, Figure 6.8 shows deviation of temperature, zonal, and meridional wind.

Various approaches to construct time-height sections of deviations or perturbations exist; three are discussed in App. C.2. For this case study we want to suppress long-term changes and emphasize short periodic waves. Hence, at each altitude level the respective linear trend is subtracted (see App. C.2 for details).

The black lines in Fig. 6.8 are used to highlight dominant phases. Phases show various slopes and vertical distances. All of them descent, indicating upward propagating wave energy (e.g., *Fritts and Alexander, 2003*). Some phases change their slope during the measurement (e.g., in temperature on third day from 2 UT to 15 UT between 48 and 36 km altitude), others became weaker (e.g., in zonal wind on second day and third night, between 52 and 37 km altitude). Phases in temperature appear to be steeper than in wind speed. Temperature deviations show also converging phases (during first evening at ≈ 48 km altitude, during second day at ≈ 50 km altitude, and during second night at ≈ 66 km altitude), and intersection of phases (during first night at ≈ 73 km altitude). Some of the wavy structures occur

6.3 Case study – gravity waves in wind and temperature

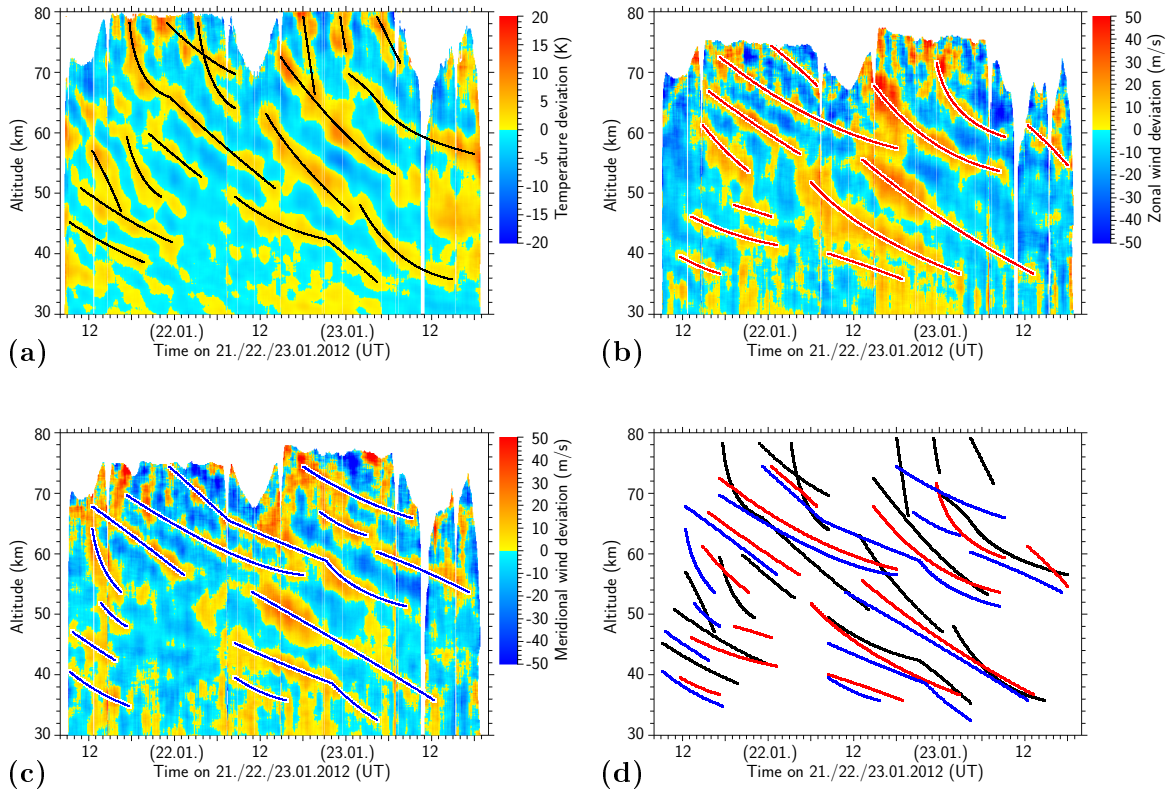


Figure 6.8 Time-height sections of temperature deviation (a), zonal wind deviation (b), and meridional wind deviation (c) for 21.–23.01.2012. Solid lines highlight dominant phases, i.e., dominant maxima of the perturbations. In (d) only these dominant maxima are depicted; black: temperature, red: zonal wind, blue: meridional wind.

similarly in all three quantities. To emphasize this, phases of zonal and meridional wind are superposed to temperature deviation in Fig. 6.8(d) with red and blue lines, respectively. For instance, during the whole second night between about 45 and 60 km altitude, a phase appears first in meridional wind, then in zonal wind, and finally in temperature, one upon the other, its slope increases. Another interesting example occurs during the first evening: Just below 50 km altitude there is a zonal phase nearly parallel to a phase in temperature, and a more steeper phase in meridional wind is nearly parallel to a phase in temperature just above 50 km altitude. There are some examples of paired phases (i.e., lying on top of each other) in zonal and meridional wind: during the first evening between 67 and 56 km altitude, during the first night until the second evening between 70 and 59 km altitude, and during the second day just below 40 km altitude; in all these examples, the meridional wind disturbance occurs earlier and at lower altitudes than the zonal wind disturbance.

Regarding examples of paired phases of zonal and meridional wind disturbance, and steeper slopes of temperature deviations, the deviations in both wind components show more similarity to each other than temperature deviation to one of the wind deviations.

A more sophisticated impression of a possible connection between deviations of different quantities is given in Fig. 6.9: It shows color-coded the meridional wind deviation, super-

imposed with zero-crossings of either zonal wind deviation (panel (a)) or temperature deviation (panel (b)) as contour lines. On first view, both wind deviations appear to be more similar to each other, than temperature deviation to meridional wind deviation. In panel (a) contour lines show in general similar orientation as the color coded data. In some cases, the contour lines just match with minima and maxima of meridional wind deviation: e.g., during the first night above 55 km altitude, and during the second night above 45 km altitude. This indicates some relation between the phases of zonal and meridional wind deviation. The relation between temperature deviation and meridional wind deviation is somewhat ambiguous, see panel (b). There are examples showing similar orientation of phases (e.g., second night between 64 and 48 km altitude), but also counterexamples (during the first night the phases do not match).

The complex behavior of temperature deviation that was discussed above (with converging and intersecting phases) is also obvious regarding altitude profiles of temperature deviation at distinct times. Figure 6.10 shows the temporal evolution of temperature deviation with the help of three altitude profiles. All of them show wavy structures, but with varying amplitude and wavelengths. At the left panel a part of the wavy structure seems to be missing: At 39 and 51 km altitude there are no distinct minima, although the remaining parts of the profile show a more or less regular wave structure. This might be caused by superposition of waves, this profile is temporally close to the converging of two phases discussed above. The middle panel, as counterexample, shows very regular wave structure with a wavelength of ≈ 8.5 km, its amplitude varies only weakly with altitude. At the right panel the wavy structure has a wavelength of ≈ 11 km, but the shape is irregular: The distance between consecutive maxima and minima is ≈ 7 km, while the distance between consecutive minima and maxima is only ≈ 4 km. Again, this might be caused by superposition of waves.

6.3.1 Hodograph analysis

A widely used technique to analyze internal gravity waves from wind measurements is the hodograph analysis (e.g., *Cot and Barat, 1986; Hamilton, 1991; Sato, 1994*). Strictly speaking, the hodograph analysis provides only accurate estimates when the wind fluctuations are

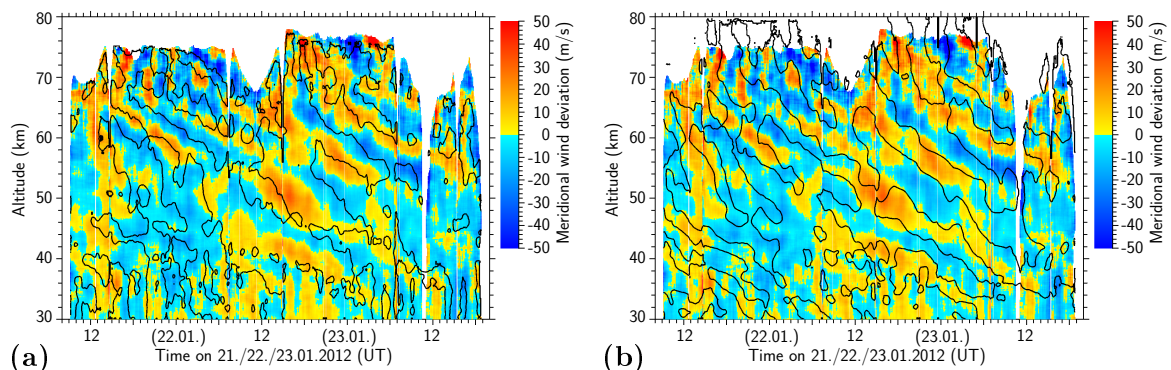


Figure 6.9 Combination of temperature and wind deviations: (a) deviation of meridional wind and zero-crossing of zonal wind deviation. (b) deviation of meridional wind and zero-crossing of temperature deviation.

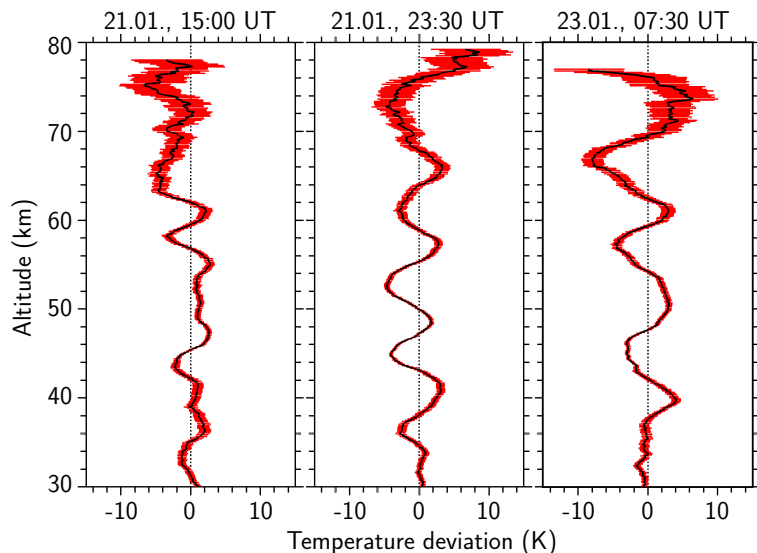


Figure 6.10 Exemplary altitude profiles of temperature deviation on 21.01., 15:00 UT; 21.01., 23:30 UT; and 23.01., 7:30 UT.

caused by a single monochromatic wave (e.g., *Hamilton, 1991; Sato, 1994*). The idea is to couple for a distinct time and in a certain altitude range the zonal and meridional wind deviations. From this one can obtain some information about vertical and horizontal propagation direction of the wave, its intrinsic period and vertical wavelength.

A hodograph is constructed in that way, that for a given time and a given start altitude the values of meridional and zonal wind deviation are plotted against each other, increasing the altitude until the resulting curve encloses an angle of 360° . If both deviations are affected by a wavy structure, the resulting plot has approximately the shape of an ellipse. The vertical distance between the start altitude and the altitude at which the ellipse gets closed corresponds to the vertical wavelength of the wavy structure. The sense of rotation of the ellipse indicates if the wave propagates upward (clockwise rotation) or downward (counterclockwise rotation) (*Sato, 1994*). The major axis of the ellipse indicates the horizontal direction of phase propagation, but with ambiguity of 180° (*Hamilton, 1991*). The ratio of major axis to minor axis equals the ratio of intrinsic frequency of the wave to Coriolis parameter¹ (*Hamilton, 1991*). This allows to estimate the intrinsic frequency of the wave, which otherwise would be inaccessible for an observer at a fixed point from a single snapshot measurement.

Three examples of the hodograph analysis, together with respective altitude profiles of temperature deviation, and zonal and meridional wind speed deviation, are shown in Fig. 6.11. The first example is from the first night: 3:30 UT on 22.01.2012 (Figs. 6.11(a) and 6.11(b)). Below 55 km altitude there is nearly no temperature disturbance, then the amplitude increases to about 5 K. Deviations of both wind components show wavy structures in the whole altitude range, but their amplitudes increase at around 55 km. Above, the amplitude of the zonal wind deviation stays constant at ≈ 20 m/s, while the amplitude of meridional wind deviation further increases with altitude. The hodograph for the altitude range 57–63 km is shown in the left panel of Fig. 6.11(b). In that altitude range the zonal wind deviation is larger than the meridional wind deviation. This yields an elliptic hodograph whose major axis is inclined 20° against the abscissa, which denotes zonal wind deviation. Hence, the horizontal direction of

¹For the latitude of ALOMAR the Coriolis parameter corresponds to $\approx 1.36 \cdot 10^{-4} \text{ s}^{-1}$ or $\approx 12.82 \text{ h}$.

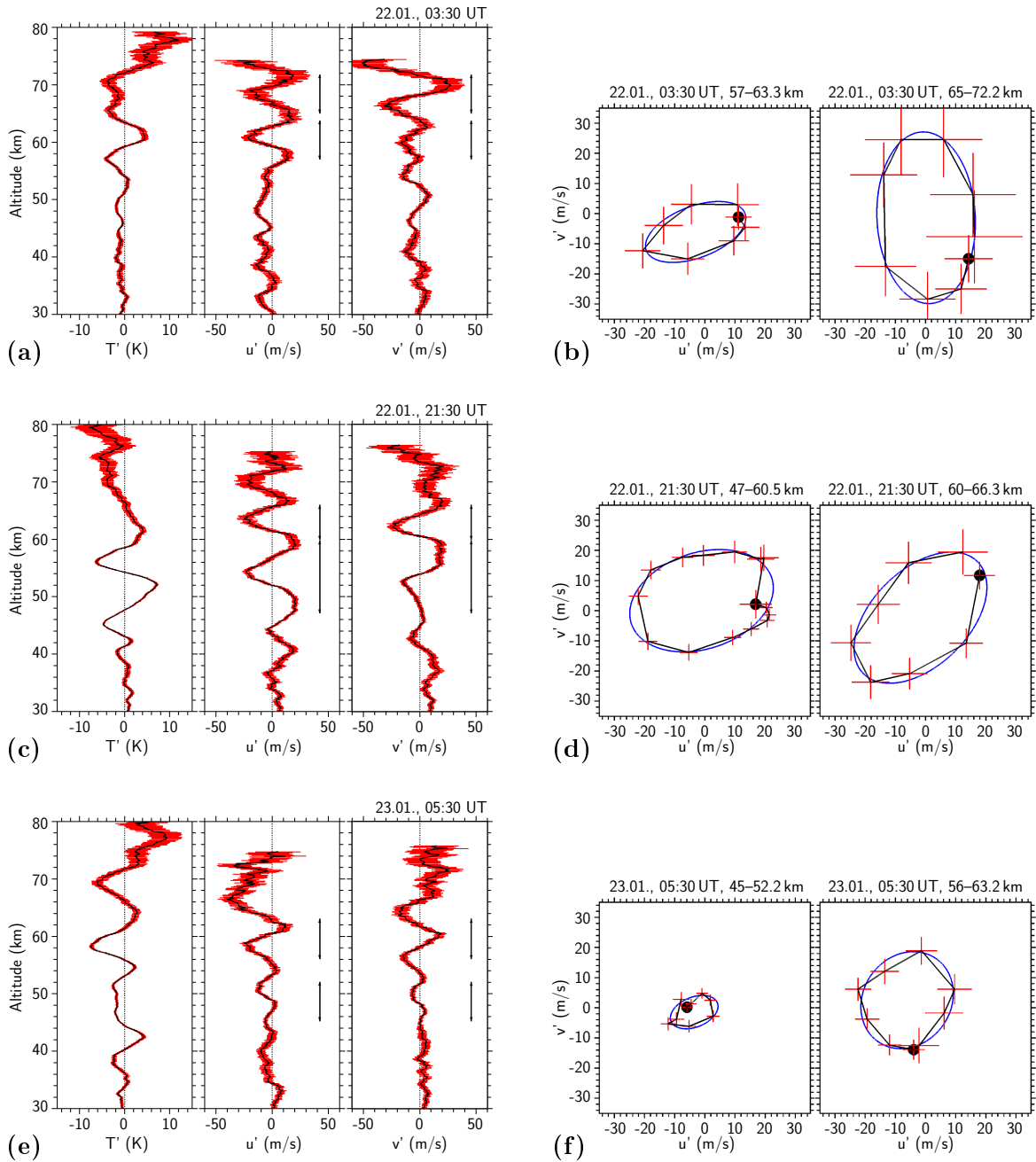


Figure 6.11 Altitude profiles of temperature deviation, and zonal and meridional wind deviation for various times and respective hodographs for various altitude ranges: (a) altitude profiles of T' , u' , and v' for 22.01., 3:30 UT, (b) respective hodographs for 57–63 km (left) and 65–72 km (right); (c) altitude profiles of T' , u' , and v' for 22.01., 21:30 UT, (d) respective hodographs for 47–61 km (left) and 60–66 km (right); (e) altitude profiles of T' , u' , and v' for 23.01., 5:30 UT, (f) respective hodographs for 45–52 km (left) and 56–63 km (right). Vertical arrows in (a), (c), and (e) indicate altitude ranges for hodographs. The big black dots in (b), (d), and (f) mark the wind deviations at the respective start altitudes.

wave propagation is nearly east- or westward. The sense of orientation of the hodograph is clockwise; hence, the wave propagates upward. This is consistent with the descending wave phases in the time-height sections (cf. Fig. 6.8). The vertical wavelength is ≈ 6.3 km. The ratio of major to minor axis is 2.03, yielding an intrinsic period of 6.30 h. The right panel of Fig. 6.11(b) shows the hodograph for the altitude range 65–72 km. Since the meridional wind deviation increased, the major axis of the hodograph is now orientated nearly parallel to the ordinate, which denotes meridional wind deviation. Hence, the horizontal direction of phase propagation is now north- or southward. Again, the hodograph has clockwise sense of rotation. The vertical wavelength and the intrinsic period are larger than in the previous example: ≈ 7 km and 7.33 h, respectively.

The second example is from the second night: 21:30 UT on 22.01.2012. Figure 6.11(c) shows altitude profiles of temperature deviation, and zonal and meridional wind deviation. Temperature shows weak wave activity below 42 km altitude. A dominant wave occurs with amplitude up to 7 K at 52 km altitude, which fades away above 65 km altitude. Zonal wind deviation shows a more regular wavy structure, above 44 km altitude the amplitude is constantly ≈ 20 m/s. The wavy structure in meridional wind speed is less regular, and not eminent below 50 km altitude. Hodographs for the altitude ranges 47–60 km and 60–66 km are shown in Fig. 6.11(d). For both the sense of rotation is clockwise. Ratios of major to minor axis are similar (1.53 and 1.65), resulting in intrinsic periods of 8.4 h and 7.8 h, respectively. The major axis of the lower hodograph (left panel of Fig. 6.11(d)) is inclined by 18° against the zonal wind deviation axis, while for the upper hodograph (right panel of Fig. 6.11(d)) the major axis is inclined almost 45° against zonal axis and meridional axis as well: The horizontal direction of phase propagation is northeast- or southwestward. The vertical wavelength is ≈ 13 km in the lower part and only 6 km in the upper part.

The third example is from early morning of the third day: 5:30 UT on 23.01.2012. Altitude profiles of temperature, zonal and meridional wind deviation are shown in Fig. 6.11(e). The temperature perturbation is somewhat irregular around 50 km altitude. The wind perturbations show only small amplitudes below about 55 km altitude. Hodographs for the altitude ranges 45–52 km and 56–63 km are shown in Fig. 6.11(f). Remarkable is the hodograph for the upper altitude: It has a nearly circular shape. Hence, there is no information about the horizontal propagation direction as the intrinsic period (11.1 h) approaches the Coriolis period. As mentioned in Sect. 2.2 this would lead to wave filtering.

Using the dispersion relation Eq. (2.4) and the intrinsic frequency $\hat{\omega}$, the vertical wavelength $\frac{2\pi}{m}$, and the buoyancy frequency N , it is possible to derive the horizontal wave number k_h . This can also be achieved using the Doppler relation Eq. (2.1) and the intrinsic frequency $\hat{\omega}$, the observed period $\frac{2\pi}{\omega}$, and the background wind \bar{u}_h in the direction of wave propagation.

The buoyancy frequency is calculated from the background temperature using Eq. (2.3). The observed period is estimated from the highlighted maxima of the wind perturbations shown in Fig. 6.8. The intrinsic period and the vertical wave number follow from the hodograph analysis. The calculation of the background wind in the direction of wave propagation uses the inclination of the major axis of the hodograph (i.e., $\varphi_{\text{hodograph}}$). Respective directly derived and calculated values are listed in Tab. 6.1. As long as the direction of wave propagation is not determined, both, the dispersion relation and the Doppler relation, yield horizontal wave numbers whose sign is ambiguous. Despite that, the values of k_h are comparable. In most cases $k_{h,\text{dispersion}}$ is 1.8–3.6 times larger than $k_{h,\text{Doppler}}$, for one case (22.01., 21:30 UT, 47–60.5 km) both values are nearly identical. The derived horizontal wave numbers

Table 6.1 Deduced background and wave parameters

| date, time altitude range (km) | 22.01., 03:30 | | 22.01., 21:30 | | 23.01., 05:30 | |
|---|---------------|---------|---------------|---------|---------------|---------|
| | 57–63.3 | 65–72.2 | 47–60.5 | 60–66.3 | 45–52.2 | 56–63.2 |
| \bar{u}_h (m/s) | ±13.9 | ±12.4 | ±22.4 | ±15.7 | ±29.3 | ±18.0 |
| N (10^{-2} s^{-1}) | 1.78 | 2.03 | 1.79 | 1.89 | 1.80 | 1.88 |
| m (10^{-4} m^{-1}) | 9.97 | 8.73 | 4.65 | 9.97 | 8.73 | 8.73 |
| observed period $\frac{2\pi}{\hat{\omega}}$ (h) | 10 | 9 | 17 | 9.5 | 17 | 9 |
| intrinsic period $\frac{2\pi}{\hat{\omega}}$ (h) | 6.26 | 7.35 | 8.36 | 7.74 | 7.72 | 11.09 |
| $\varphi_{\text{hodograph}}$ ($^\circ$) | 20.73 | 92.74 | 18.01 | 44.20 | 21.76 | 54.74 |
| $k_{h, \text{dispersion}}$ (10^{-6} m^{-1}) | ±13.62 | ±8.36 | ±4.11 | ±9.47 | ±8.77 | ±3.68 |
| $k_{h, \text{Doppler}}$ (10^{-6} m^{-1}) | ±7.53 | ±3.53 | ±4.73 | ±2.65 | ±4.21 | ±2.03 |
| $k_{h, \text{dispersion}}/k_{h, \text{Doppler}}$ | 1.81 | 2.37 | 0.87 | 3.57 | 2.08 | 1.81 |

correspond to horizontal wavelengths of 500 to 3100 km.

The intrinsic frequency, the vertical wavelength and the horizontal wave number show large variability at different altitudes and different times. Therefore, the observed wave structures are certainly not caused by one single monochromatic wave, but result from the superposition of various waves. The overall picture is dominated at different altitudes and times by different waves.

6.3.2 Gravity wave energy density

The potential and kinetic energy density (per unit mass) of a gravity wave are given by (e.g., *Geller and Gong, 2010*):

$$E_{\text{pot}} = \frac{1}{2} \frac{g^2}{N^2} \left(\frac{T'}{\bar{T}} \right)^2 \quad (6.1a)$$

and

$$E_{\text{kin}} = \frac{1}{2} \left(u'^2 + v'^2 \right). \quad (6.1b)$$

Following *Geller and Gong (2010)*, the ratio of kinetic and potential energy density is:

$$\frac{E_{\text{kin}}}{E_{\text{pot}}} = \frac{1 + f^2 \cdot \hat{\omega}^{-2}}{1 - f^2 \cdot \hat{\omega}^{-2}}, \quad (6.2)$$

which can be transformed to

$$\hat{\omega} = \pm f \sqrt{\frac{E_{\text{kin}}/E_{\text{pot}} + 1}{E_{\text{kin}}/E_{\text{pot}} - 1}}, \quad (6.3)$$

to estimate the ensemble average intrinsic frequency.

Figure 6.12 shows altitude profiles of potential and kinetic energy density (left panel), total energy density (middle panel), and the ratio of kinetic and potential energy density (right panel) for different time segments of the measurement. The order of magnitude of the potential energy density is comparable to that derived by *Schöch (2007)*, but notable smaller than

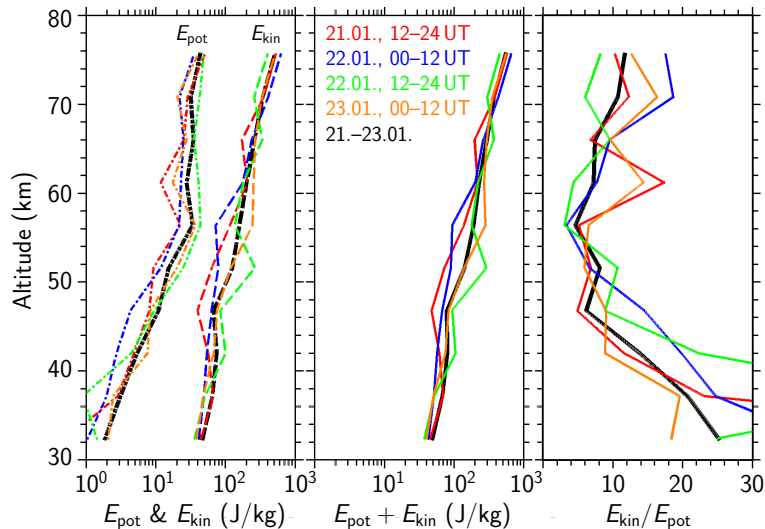


Figure 6.12 Altitude profiles of gravity wave potential, kinetic, and total energy density, and the ratio of kinetic to potential energy density. See text for details.

that derived by *Placke et al. (2013)*. The growth of the potential, kinetic, and total energy density with altitude is exponential, as expected. Below 46 km altitude the ratio $E_{\text{kin}}/E_{\text{pot}}$ decreases with altitude, above 56 km altitude it increases; between 46 km and 56 km altitude the mean value is ≈ 7 . Using Eq. (6.3) this value yields an intrinsic period of ≈ 11.1 h. The larger energy ratio of 25 at 32 km altitude yields an intrinsic period of 12.3 h. Hence, there is more energy on perturbations with smaller scales at higher altitudes. *Nastrom et al. (1997)* derived from balloon measurements in the stratosphere below 20 km altitude a kinetic-to-potential energy ratio of 5, *Placke et al. (2013)* derived from combined radar and lidar measurements in the mesosphere between 80 and 95 km altitude a value of ≈ 0.7 . The fact that different instruments resolve different parts of the gravity wave spectrum might be an explanation for these differences, since kinetic and potential energy density are sensitive to different parts of the gravity wave spectrum (*Geller and Gong, 2010*). This case study is the first study that investigates during multiple days the potential and kinetic energy density with the same instrument and therefore the same spectral sensitivity.

Summary

This case study is outstanding in different aspects. First, these are the first data of this kind: wind and temperature measurements in the middle atmosphere by a single instrument, from 30 to 80 km altitude with a vertical resolution of 3 km, covering 60 h with a temporal resolution of 1 h. But this measurement is not only very long, it also shows persistent wave structures during the whole measurement in temperature and wind data. These perturbations are connected to each other: From Fig. 6.9 it appeared, that there is some phase relation; but this phase relation is not constant in time. The wave structures show variability, regarding in time and altitude. This suggests that the wavy structure is the result of the superposition of various waves. This is also backed by the hodograph analysis. The energy density of the wave structure consists of potential and kinetic energy, both increase with altitude. The ratio of kinetic to potential energy density allows estimating the ensemble average intrinsic frequency. In this case study daylight data were included successfully in the wind analysis for the first time.

Chapter 7 Summary and outlook

After the experimental setup and the wind retrieval algorithm of the ALOMAR RMR lidar were introduced in Chap. 4, the data set, which spans four winter seasons, was presented in Chap. 5. The lidar wind data were validated using three different methods: vertical and coplanar wind measurements, and comparison to sodium lidar wind data. Geophysical results were shown in Chap. 6, this included mean winds and temperatures during winter and a comparison with temperatures and winds from models, radars, and meteorological rockets. Variability from year to year and within single months, and a case study of a long measurement spanning three days, which showed pronounced wave structures were discussed.

7.1 Summary and conclusions

Data set

The data set used in this thesis spans the years 2009 to 2012. The analysis was restricted to nighttime measurements during the months November to March. Even this restricted data set contains nearly 700 h. This is the most extensive data set of wind measurements in the Arctic middle atmosphere, ranging from the upper stratosphere up to the mesosphere (i.e, from 30 to ≈ 80 km altitude). Since the ALOMAR RMR lidar is operated whenever permitted by weather conditions and available manpower, the seasonal and daily coverage is good; especially in January and February, when enhanced effort to perform measurements is applied in order to capture SSW. Therefore, January is the month with the most measurement hours (40 % of all measurements). During these four years five measurements lasted longer than one day. Such long measurements are particularly favorable for studying gravity waves with periods of several hours. But also shorter measurements are valuable for climatological studies.

Validation

Vertical wind measurements have been used to test the retrieved wind speeds and to apply an atmospheric calibration when the internal calibration was not sufficient. In Sect. 5.2.1 two exemplary measurements of vertical wind speed from December 2011 and December 2012 were presented. The measurement in 2012 showed an altitude profile that was straight and close to zero. This demonstrates the ability of DORIS to measure wind speeds. However, the measurement in 2011 showed large deviation from zero and the altitude profile of vertical wind speed was bent. A technical reason for this was identified. By variation of the entrance ratio it was possible to take this into account and to obtain an altitude profile of vertical wind speed that is straight and whose mean wind is close to zero. This is called atmospheric calibration.

Simultaneous measurements of zonal winds with both lasers/telescopes of the ALOMAR

RMR lidar provide the possibility to compare two independently derived zonal winds with each other. In Sect. 5.2.2 two exemplary measurements were presented. For the measurement in January 2012 the agreement of both zonal wind speed profiles was good: in the altitude range 40–50 km both profiles differ by ≈ 6 m/s, in the altitude range 40–70 km the difference of zonal wind speeds is ≈ 9 m/s. The horizontal distance of the sounding volumes is ≈ 36 km at 50 km altitude and ≈ 51 km at 70 km altitude. For the measurement in November 2010 the difference of both zonal winds is 20 m/s in the altitude range 40–50 km and even 31 m/s in the altitude range 40–70 km. However, during this measurement the altitude profiles of temperature and zonal wind speed showed pronounced wave-like structures.

Since the ALOMAR observatory hosts a second lidar which is capable to perform wind measurements it is self-evident to compare the winds measured independently by both instruments. This was done in a joint campaign in January 2009 (*Hildebrand et al.*, 2012). Since the ALOMAR sodium lidar covers the height range 80–110 km, the comparison of both lidars is limited to the altitude range 80–85 km, which is the signal range limit for both instruments. Both instruments share the same receiving telescopes, hence, they have the same line-of-sight and probe the same volume in the height range of overlap. A comparison on long and short time scales was presented in Sect. 5.2.3. The agreement of altitude profiles of zonal wind integrated over nearly ten and a half hour is very good, except for the topmost kilometer: Mean winds in the altitude range of overlap (79–83 km) are (-1 ± 8) m/s and (-5 ± 1) m/s for RMR and Na lidar, respectively. Also single profiles with 1 h integration agree well within the respective error bars. The combination of both instruments allows measuring wind speeds in the middle atmosphere from 30 km to 110 km altitude.

Winds and temperatures in Arctic winter

The derived winds in the months November to March were compared to winds derived by co-located radar systems and winds extracted from models in Sect. 6.1. For that monthly mean winds were computed from the cumulated data of the years 2009 to 2012. In general these monthly mean winds match to winds from models and radars. Occasionally some differences were noted, which can be attributed to different technical problems. Most of these problems are now solved.

The presented winds and temperatures show large variability, especially in January and February. This was analyzed in more detail in a year-to-year comparison of mean winds and temperatures in January. The large year-to-year variability can be quite different: While the mean temperatures of two years might look similar, the mean winds might differ remarkably, and vice versa. There is also a notable variability within single months. The comparison of January 2010 and January 2012 showed a somewhat different development during these months. In 2010 zonal wind shows large variability while temperature shows a significant change only during the last day. In 2012 the temporal evolution after a minor SSW was captured. The temperature shows large variability, including the reformation of the stratopause at about 70 km altitude. In general, the variability in temperature and wind in January and February is primarily caused by SSW.

The comparison to models shows that this variability is not captured in climatological data sets like HWM07, but is captured partly in ECMWF. Differences of, e.g., 20 K (January 2009, 60 km altitude) and 30 m/s (November 2010, 60 km altitude), respectively, are found for special cases. These differences could be caused by wave events that are not completely described in the different reference data sets.

Wave studies

In Sect. 6.3 a detailed case study was presented. Data were obtained during a continuous measurement that lasted for nearly sixty hours. Similar wave structures were obvious and persistent in time-height sections of temperature, and zonal and meridional wind speed. Some of these wave structures appear similarly in temperature and wind, most of the wave structures in zonal wind have a counterpart in meridional wind. No fix relationship between wave structures in temperature and wind was found. This indicates that the even well pronounced wave structure results from the superposition of various different waves. To investigate the wave structure the hodograph technique was used. This allowed deriving the intrinsic period, the propagation direction, and the vertical wavelength of the wave-like structures at selected times and altitudes. The horizontal wave number was derived at these times and altitudes from the dispersion relation for inertia-gravity waves and from the Doppler relation by including the background wind in direction of wave propagation; values are of comparable size ($k_{h, \text{dispersion}} \approx 3.5\text{--}13.5 \cdot 10^{-6} \text{ m}^{-1}$ and $k_{h, \text{Doppler}} \approx 2.0\text{--}7.5 \cdot 10^{-6} \text{ m}^{-1}$). Gravity wave kinetic and potential energy grow exponential with altitude, the total energy density is dominated by the kinetic energy density. From the ratio of kinetic and potential energy density the ensemble average intrinsic frequency was derived. It is close to the Coriolis parameter. For these inertia-gravity waves the kinetic energy is about 10 times larger than the potential energy. The variation of the wave parameters with altitude and time shows that the wave structures were not caused by one single monochromatic wave but by superposition of various waves. In this case study also daylight data were used, showing for the first time the daylight capability of DORIS.

7.2 Outlook

This thesis demonstrated the general capability of the ALOMAR RMR lidar to measure winds in the middle atmosphere. Of course, there is still some potential for further minor improvements. But in principle the DORIS setup already provides opportunities for extensive studies of middle atmosphere winds.

Since summer 2013 an enhanced laser pulse spectrometer is in operation. Its higher sensitivity and capability to measure every single laser pulse allows determining the frequency offset of the transmitting lasers more precisely. In March 2013 the focal optics of the receiving telescopes were improved for a smaller the field of view of the telescopes. This, in turn, reduces the solar background and, even more important, makes the wind retrieval less sensitive to the alignment of the detection system. In September 2010 a new daylight filter for the 532 nm branch was installed. Its transmittance is 4 times higher compared to the old daylight filter and its spectral filter characteristic is more stable. This is a major improvement for wind measurements under daylight conditions.

The enhanced daylight capability allows analyzing long continuous measurements and consequently investigating variations in winds and temperatures on time scales of several hours (i.e., gravity waves). Furthermore the daylight capability provides wind measurements also in summer and around the equinoxes. This will yield a full seasonal cycle of horizontal winds in the middle atmosphere. Of special interest is the temporal evolution of the transition from the winter state with predominant eastward winds to the summer state with predominant westward winds and vice versa.

The altitude coverage of DORIS can be extended by including the contribution of aerosol scattering in the wind retrieval. This will allow measuring winds in the lower stratosphere

Chapter 7 Summary and outlook

and upper troposphere. The ice particles of noctilucent clouds in about 83 km altitude, which are advected by the background wind, provide a high backscatter signal and will therefore enable wind measurements in that altitude region.

As stated above, the propagation of atmospheric waves strongly depends on the background wind field. Sudden stratospheric warmings and mesospheric inversion layers are events which are coupled tightly to dynamical processes in the entire middle atmosphere, including the propagation of waves and their interaction with the background wind field. DORIS now provides the possibility to measure winds (and temperatures) with high vertical and temporal resolution in the altitude range from 30 to 80 km, as recommended by *Meriwether and Gerard (2004)*. This will contribute to a better insight of the dynamical processes in the middle atmosphere.

Appendix

Appendix A Data processing

A.1 Database

During measurements the atmospheric raw data are stored in records containing the backscatter signal of all individual detectors from 1000 laser pulses (≈ 33 s) for each laser/telescope. The backscatter signal is sorted to range bins of 50 m.

Data from other instruments that describe the performance of the instrument are stored in various ways. For example, data from the LPS is stored with a temporal resolution of few milliseconds, alternately for laser 1 and laser 2.

The data used in this thesis were preprocessed to a level which is called “Level 1a”. This preprocessing includes correction of detector dead time, subtraction of background (atmospheric and electronic), taking the Rayleigh extinction into account, and determining the seeder signals $S_0|_{\text{seeder}}$ and $S_{I_2}|_{\text{seeder}}$ that are used to derive D_{seeder} . The backscatter signal are sorted to matrices with a fixed time-altitude grid (5 min \times 150 m). Altitude independent data (e.g., $S_0|_{\text{seeder}}$ and $S_{I_2}|_{\text{seeder}}$) are sorted to vectors with the same time grid. The “Level 1a” data include additional instrument-performance data from secondary instruments (e.g., laser frequency offset from LPS), which are also sorted to the same time grid.

A.2 Basic processing

The top altitude of each single record is determined as the altitude where the uncertainty of the backscatter signal exceeds half the signal. The backscatter profiles of the three detectors of a channel (e.g., detectors VDH, VDM, and VDL of the Doppler channel 532 l2 in Fig. 4.6) are combined to a single composite profile. The signal ratio for concatenation is determined for each single record in the lowest 5 km of the altitude range of the more sensitive detector. If the gating altitude of this detector is too high, the signal of the less sensitive detector might be very weak in the altitude range of overlap. In this case the lower part of the concatenated profile might be bent very slightly. But even very small uncertainties during concatenation might become relevant when dividing the Doppler channel and the reference channel, resulting in slightly biased wind speeds.

After concatenation the composite profiles are smoothed in height, typically with a running mean filter with a window size of 3 km.

A.3 Temperature retrieval

For the temperature retrieval the reference channel (532 Cab. in Fig. 4.6) is used. Atmospheric temperature is calculated by hydrostatic integration of atmospheric density. To derive a density profile from a backscatter profile the quadratic range dependency has to be

Appendix A Data processing

taken into account. The transformation from backscatter profile to density profile is more complicated in the presence of aerosols (as they alter the backscatter signal). Hence, the following calculations are limited to altitudes above 30 km. The start altitude for the downward integration is given by the top altitude of each record. The start temperature is taken from the reference atmosphere NRLMSISE-00 (Picone *et al.*, 2002).

Before the temperature matrix is smoothed in time, records whose temperature profile differ remarkably from neighboring records are rejected. The temperature matrix is then smoothed in time, typically with a running mean filter with a window size of 1 h.

A.4 Wind retrieval

The composite matrices of reference signal S_0 and Doppler signal S_{I_2} are divided, yielding the Doppler ratio D_{meas} . Again, records whose Doppler ratio profile differs remarkably from neighboring records are rejected. Afterward the Doppler ratio is smoothed in time. Also the frequency offset $d\nu$ and the seeder Doppler ratio D_{seeder} (both are vectors along time axis) are smoothed in time. Then the Doppler ratio is divided by seeder Doppler ratio, by the entrance ratio E_{tel} , and by the iodine transmittance $T_{I_2|\nu_0}$ (see Eq. (4.7)).

The following procedure to derive wind speed is applied to each element of the matrix of measured Doppler ratio: A column of the lookup table of modeled Doppler ratio D_{model} is selected using the measured temperature T . Line-of-sight wind speed $v_{\text{l.o.s.}}$ is derived by finding the measured Doppler ratio in that column. The laser frequency offset is transferred into a wind speed offset $dv_{\text{l.o.s.}}$ (see Eq. (4.12b)), which is subtracted from the derived line-of-sight wind speed. Finally, the line-of-sight wind speed is projected to zonal or meridional wind (for tilted telescope measurement).

A.5 Laser frequency offset

The LPS measures light from different sources which different characteristics. While the light from the power lasers is pulsed, with short pulse lengths (~ 10 ns) and high intensities, the light from the seed laser has lower intensity and is continuously. Hence, the LPS is operated in two modes, which differ in acquisition mode: one mode for the power lasers, the other mode for seed laser and dark fiber. The LPS stores data in two different data types: simply the maximum value of a laser pulse (or seed laser measurement), temporally resolved pulse forms. The data acquisition rate of the LPS is limited: During 1 h (i.e., for about 108 000 laser pulses) it stores about 10 000 maximum values (which are averages over four laser pulses) and about 2 000 pulse forms (which are also averaged over four laser pulses).

The pulse form data is sufficient to determine the frequency offset, since it contains background information for power lasers as well as for seed laser. Contrary, the single value data is not sufficient, since it does not contain information about the background for the power laser mode. But the single value data has a better temporal resolution than the pulse form data. Hence, it is necessary to couple both data sets to benefit from high temporal resolution (single value data) and background information (pulse form data).

First, we analyze the pulse form data. Figure A.1 shows an exemplary pulse form measured by the detector in front of the iodine cell. The first 60 ns are used to determine the background signal. Its uncertainty is calculated as the standard error of the mean. The pulse height is determined as maximum value of the pulse form. Its uncertainty corresponds to the random noise of the background (its standard deviation). When subtracting the background

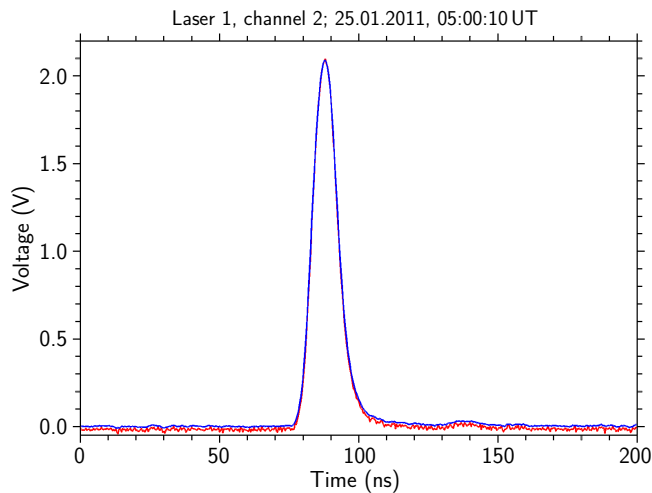


Figure A.1 Exemplary laser pulse form. Data of power laser 1 in front of the iodine cell, from 25.01.2011, 05:00:10 UT. The red line is the original data, which is affected by the random noise and the (slightly negative) offset voltage. The blue line is smoothed over five points and the offset voltage is taken into account.

signal from the pulse height, the uncertainty of the latter is raised by the uncertainty of the background signal. Actually, we are interested only in the background signal and the error of the pulse height. We do not use the pulse height, since we get this from the single value data (which have better temporal resolution). For the seed laser and the dark fiber we can use the pulse form data to determine the measurement uncertainty as standard error of the mean.

Second, we analyze the single value data. This is straight forward: We simply take the stored values, they correspond to the pulse heights.

Now we couple both data sets: subtracting the background (pulse form data) from the pulse height (single value data) and assigning the measurement uncertainty (pulse form data). Both data sets have different temporal resolutions. To take this into account, we look for the nearest data point in the pulse form data for each data point in the single value data and assign it. The resultant pulse height data (high temporal resolution, background corrected, appropriate measurement uncertainty) can then be used to calculate the frequency offset.

A.6 Used software

Main part of the analysis was written in the programming language *C*. An extensive library of basic and advanced mathematical and physical functions written and maintained by Gerd Baumgarten was used. For fitting the *GNU Scientific Library* (Galassi *et al.*, 2003) and the library *MPFIT* (Markwardt, 2009) were used. Some tasks were handled using *Bash* scripts, including the interpreted programming language *GNU awk*.

Data were visualized using either the plotting library *DISLIN* (Michels, 2010) from within *C* or the command-line program *gnuplot* from within *Bash*. In few cases *gnuplot* was also used as fitting tool.

This manuscript was typeset in $\text{\LaTeX}2_{\epsilon}$ with the help of several extensions and packages,

Appendix A Data processing

including the *KOMA-Script* bundle, $\mathcal{A}\mathcal{M}\mathcal{S}$ - $\mathcal{L}\mathcal{A}\mathcal{T}\mathcal{E}\mathcal{X}$, the *natbib* bundle, and the *hyperref* package.

Appendix B Calibration – instrumental modifications and calibration measurements

This appendix first gives an overview of instrumental modifications during the years 2009 to 2012 that might affect the wind retrieval. Afterward it lists the calibrations measurements that were performed during the years 2009 to 2012.

B.1 Instrumental modifications

Iodine cell for absorption spectroscopy at seed laser

On 8 March 2011 the iodine-vapor cell which is used for the absorption spectroscopy to stabilize the seed laser (Sect. 4.2.2) was changed. This results in a change of the seed laser frequency ν_0 of about -0.1 GHz and to a change of the corresponding transmittance $T_{I_2}|\nu_0$ of the iodine-vapor cell at the detection system from ≈ 0.61 to ≈ 0.37 (see Tab. B.2).

Telescope fibers

In winter 2010/2011 different telescope fibers with different diameters were used for the NWT. This caused variations of the entrance ratio E_{NWT} . The fiber for the SET had always a diameter of 1.5 mm.

During the years 2009 to 2012 the following telescope fibers were used for the NWT:

- until 20 December 2010: 1.5 mm
- 20.12.2010 – 25.01.2011 (~ 21 UT): 1 mm
- 25.01.2011 (~ 21 UT) – 16.02.2011 (~ 0 UT): 0.5 mm
- 16.02.2011 (~ 0 UT) – May 2011: 0.8 mm
- since May 2011: 1.5 mm

Particular modifications of the detection system

From time to time some detectors are exchanged by new ones. In September 2010 a new daylight filter for the 532 nm branch was installed, afterward the 532 nm branch was realigned on 23.09.2010. To enhance the signal quality of the seed laser light a polarizer was inserted in the seed laser branch on 20.05.2011 (labelled LP in Fig. 4.6). On 30.01.2012 additionally

Appendix B Calibration in details

an attenuator was installed in the seed laser branche (labelled A in Fig. 4.6). It is expected that all these changes affect the entrance ratio E_{tel} .

During the years 2009 to 2012 the detection system was modified as follows:

- 23.09.2010: new etalon for 532 nm branch, 532 nm branch realigned
- $\sim 10./14.12.2010$: two shutters (S1 and S2) implemented
- 13.05.2011: detectors for VH and VDH exchanged
- 20.05.2011: polarizer (LP) at seed laser branch installed
- 30.01.2012 ($\sim 17:50$ UT): attenuator (A, 51.5 %) installed between L17 and LP

Summer and winter configuration

During summer the detectors for rotational Raman scattering (VRR1 and VRR2 in Fig. 4.6, 529 nm and 530 nm) are deactivated since they are not equipped with a daylight filter. To not unnecessarily degrade the signal for the other detection branches the dichroic mirror D3 is removed in spring and re-installed in autumn. This might affect the entrance ratio E_{tel} .

During the years 2009 to 2012 the dichroic mirror D3 was installed or removed on the following dates:

- until 11.03.2009: D3 installed
- 11.03.2009 – 21.10.2009: D3 removed
- 21.10.2009 – 03.05.2010: D3 installed
- 03.05.2010 – 07.12.2010 (~ 14 UT): D3 removed
- 07.12.2010 (~ 14 UT) – 10.05.2011: D3 installed
- 10.05.2011 – 08.11.2011: D3 removed
- 08.11.2011 – 21.05.2012: D3 installed
- 21.05.2012 – 23.08.2012: D3 removed
- since 23.08.2012: D3 installed

Daylight and nighttime configuration

During day stray light from the sun disturbs lidar measurements. To suppress part of the sunlight, the detection system is equipped with a Fabry-Pérot interferometer, also known as etalon. Due to its spectral filter characteristic has to be taken into account in the wind retrieval. For that the transmittance spectrum $T_{I_2}(\nu)$ of the iodine-vapor cell is measured for daylight and nighttime conditions separately, $T_{I_2}|\nu_0$ and E_{tel} are affected too. Additionally all these quantities are effected (slightly) by the etalon's transmittance spectrum (i.e., the distance of the coplanar plates or the refractive index inside the etalon).

As mentioned in Sect. 4.4.4, improper installation of the mirrors on the kinematic bases yields signal variations at the reference channel and the Doppler channel, which are different for the different ports of the detection system. This leads to variations of measured Doppler

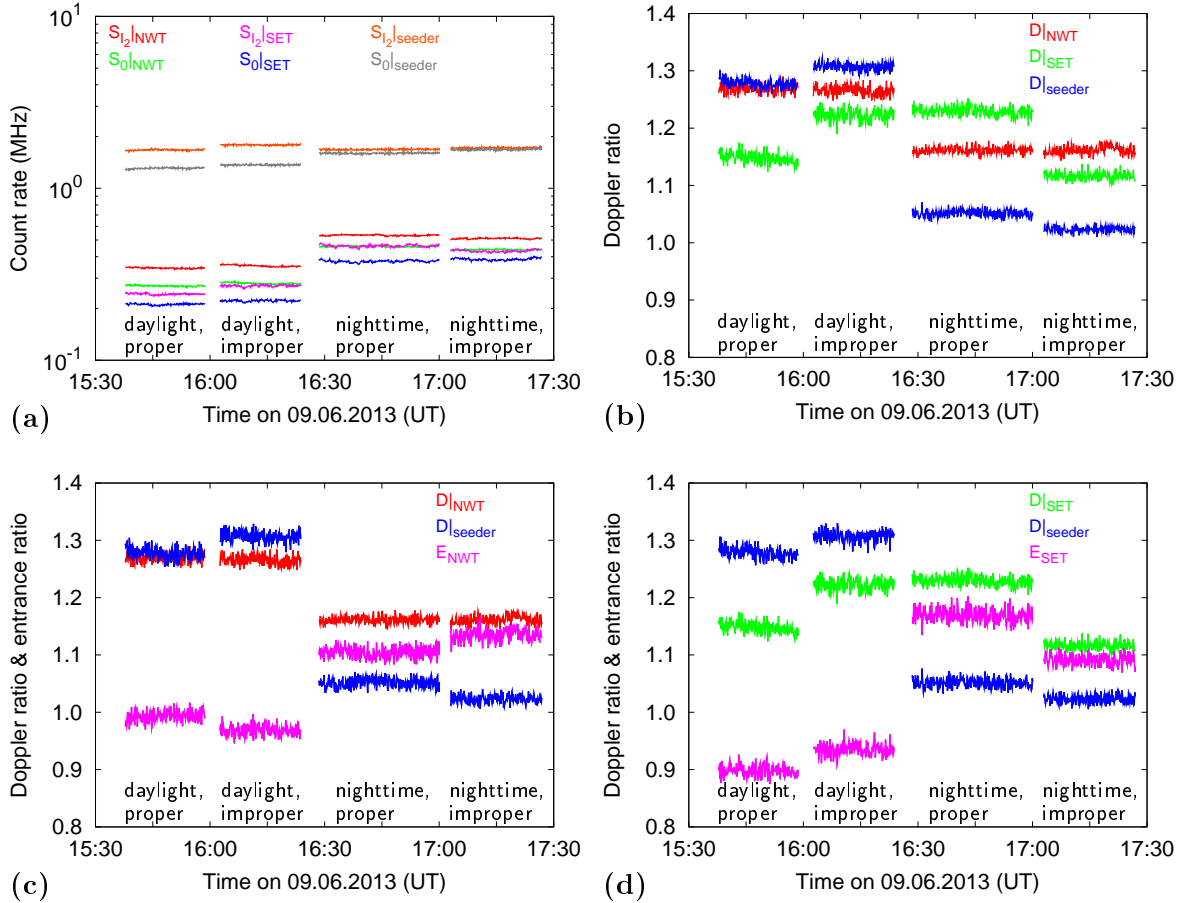


Figure B.1 Effect of improperly mounted mirrors for etalon bypass for daylight and nighttime configuration on entrance ratio. First part: daylight, proper mounting; second part: daylight, improper mounting; third part: nighttime, proper mounting; fourth part: nighttime, improper mounting. (a) count rate for different ports and detectors; (b) Doppler ratio for different ports ($D|_{\text{NWT}}$, $D|_{\text{SET}}$, and $D|_{\text{seeder}}$); (c) Doppler ratio for NWT and seed laser port and resulting entrance ratio $E|_{\text{NWT}} = \frac{D|_{\text{NWT}}}{D|_{\text{seeder}}}$; (d) same as (c) but for SET.

ratio $D|_{\text{meas}}$, seeder Doppler ratio $D|_{\text{seeder}}$, and entrance ratio $E|_{\text{tel}}$. For a test measurement the mirrors were mounted deliberately improper to study the impact. Figure B.1 shows the resulting time series of count rates, Doppler ratios, and entrance ratios. Focus on the third and fourth part, which are for nighttime configuration. As is shown in Fig. B.1(a), improper mounting yields only small variations of the count rates. But these small changes result in quite big variations of the Doppler ratio, as is shown in Fig. B.1(b). The $D|_{\text{NWT}}$ and $D|_{\text{SET}}$ in this figure corresponds to $D|_{\text{meas}}$ during atmospheric measurement, and $D|_{\text{seeder}}$ corresponds to $D|_{\text{seeder}}$. Apparently, $D|_{\text{NWT}}$, $D|_{\text{SET}}$, and $D|_{\text{seeder}}$ are affected differently. Figs. B.1(c) and B.1(d) show the resulting impact on the entrance ratio: While $E|_{\text{NWT}}$ increases for improper mounting, $E|_{\text{SET}}$ decreases.

As mentioned in Sect. 4.5.1 it is possible to notice such improper mounting of the etalon bypass during data analysis. The fact that three quantities ($D|_{\text{meas}}$, $D|_{\text{seeder}}$, and $E|_{\text{tel}}$) are affected by the improper mounting, and that both telescopes are affected differently prevents

Appendix B Calibration in details

currently an automated correction which would be valid in all cases. But a correction by estimating a correction factor is possible (see Eq. (4.10)). The correction can be verified by analysing vertical wind speed measurements or comparison to other data.

Phase lag of the rotary fiber selector

The mirror of the RFS couples the backscattered light from the SET into the detection system (see scheme of the detection system in Fig. 4.6). The backscattered light from the NWT passes through a hole in the RFS. A small deviation between the mirror plane and the plane of rotation of the RFS might cause angular deviations of the beam toward the detectors (*Hildebrand et al., 2012*). In February 2009 some jitter of the RFS became apparent, the complete RFS was then replaced in summer 2011. The new setup allows monitoring of the behavior of the RFS, including the angular position of reflection on the mirror surface. To study the impact of such jitter and variable position of reflection on the entrance ratio a test measurement was performed in July 2013. During that measurement the phase of the RFS was varied. The results are shown in Fig. B.2. For some reason a phase of 70° and 80° is unfavorable, the RFS cannot stabilize on these phases. Despite that, there is no impact of the RFS phase on the entrance ratio for the NWT apparent (see Fig. B.2(c)). For the SET the entrance ratio depends on the phase of the RFS (see Fig. B.2(d)). This influence is less pronounced for daylight configuration (after 13:30 UT). Probably the lenses of in front and behind the daylight filter realign the beam and compensate some angular deviation of the beam.

The wind retrieval is very sensitive to such small variations of E_{tel} . Depending on atmospheric temperature a change of E_{tel} of 1% causes a change of line-of-sight wind of about 5 m/s.

B.2 Lists of calibration measurements

The following tables list all calibration measurements that were performed during the years 2009 to 2012. As stated above various changes of the instrumental setup affect a calibration. Hence, the tables include information about daylight and nighttime configuration, and summer and winter configuration (dichroic mirror D3). Indicating the value of $D_{\text{seeder}}|_{\nu_0}$ allows to detect if the mirrors of the daylight filter bypass are installed properly. The calibration procedure is described in Sect. 4.4.

Iodine cell at detection system

A scan of the iodine cell at the detection system can be performed with light entering through various ports. Depending on the alignment of the detection system the transmittance spectrum might slightly differ for different ports. This is apparent when the spectrum is obtained in daylight configuration. A complete calibration, which also allows to determine the transmittance $T_{\text{I}_2}|_{\nu_0}$ at the stabilization frequency, requires normalization (i.e., the iodine cell needs to be removed from the optical path). If the chopper is not active during calibration, it is not possible to determine the background count rates of the detectors.

Tables B.1 and B.2 list all calibration measurements to determine the transmittance spectrum of the iodine-vapor cell and its transmittance at the stabilization frequency.

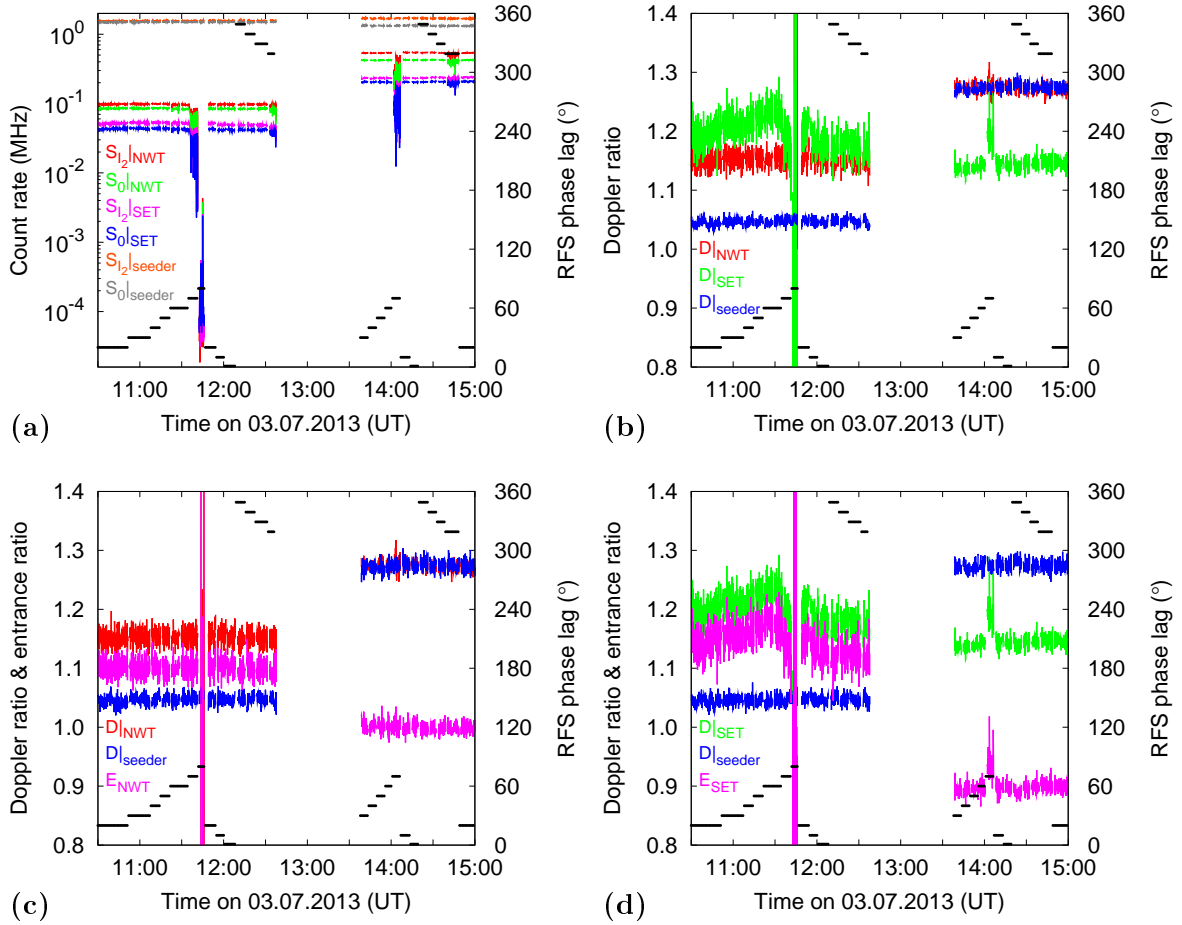


Figure B.2 Effect of RFS phase lag on entrance ratio. The RFS phase lag is indicated by black lines. First part until $\sim 12:45$ UT: nighttime configuration; second part after $\sim 13:30$ UT: daylight configuration. (a) count rate for different ports and detectors; (b) Doppler ratio for different ports ($D|_{\text{NWT}}$, $D|_{\text{SET}}$, and $D|_{\text{seeder}}$); (c) Doppler ratio for NWT and seed laser port and resulting entrance ratio $E_{\text{NWT}} = \frac{D|_{\text{NWT}}}{D|_{\text{seeder}}}$; (d) same as (c) but for SET.

The remarkable change of $T_{I_2}|_{\nu_0}$ between September 2010 and February 2012 is due to the replacement of the iodine-vapor cell that is used for the absorption spectroscopy to stabilize the frequency of the seed laser (see Sect. 4.2.2). This cell was replaced on 8 March 2011. Therefore the seed laser frequency ν_0 changed by about -0.1 GHz, which in turn led to a change of $T_{I_2}|_{\nu_0}$.

Appendix B Calibration in details

Table B.1 List of scans of the iodine-vapor cell at the detection system

| date | ports | day/night | comments |
|----------------|---------------|-----------|--|
| 21.01.2009 | sdr | night | w/o normalization; w/o chopper |
| 11.02.2009 | sdr | night | w/o normalization; w/o chopper |
| 12.02.2009 | sdr | night | w/o normalization; w/o chopper |
| 25./26.02.2009 | NWT, SET, sdr | night | RFS jitters; w/o normalization |
| 09./10.03.2009 | NWT, SET, sdr | day | w/o normalization |
| 18./19.03.2009 | NWT, SET, sdr | both | incl. normalization |
| 03.–09.09.2009 | NWT, sdr | both | various alignments of daylight filter; incl. normalization; seeder port only on 09.09. |
| 18.09.2009 | NWT, SET, sdr | night | w/o normalization |
| 06.09.2010 | NWT, SET, sdr | day | incl. normalization |
| 07.09.2010 | NWT, SET, sdr | night | incl. normalization |
| 24.–30.09.2010 | NWT | day | stability test with new daylight filter; w/o normalization |
| 13.–19.10.2010 | NWT | day | stability test with new daylight filter; w/o normalization |
| 08.08.2011 | sdr | day | w/o normalization |
| 07.02.2012 | NWT, SET, sdr | day | incl. normalization |
| 08.02.2012 | NWT, SET, sdr | night | incl. normalization |
| 01.09.2012 | NWT, SET, sdr | day | w/o normalization; daylight filter not aligned |
| 16.09.2012 | NWT, SET, sdr | night | incl. normalization |

Table B.2 Determination of iodine cell transmittance $T_{I_2}|_{\nu_0}$ at stabilization frequency.

| date | day/night | $D_{\text{seeder}} _{\nu_0}$ | $T_{I_2} _{\nu_0}$ | comments |
|------------|-----------|------------------------------|--------------------|--|
| 18.03.2009 | night | 1.0091 | 0.6136 | – |
| | day | 1.0805 | 0.6030 | – |
| 06.09.2010 | day | 1.0505 | 0.6056 | – |
| 07.09.2010 | night | 1.0176 | 0.6112 | – |
| 07.02.2012 | day | 0.6713 | 0.3677 | – |
| 08.02.2012 | night | 0.5825 | 0.3727 | – |
| 16.09.2012 | night | 0.6326 | 0.3690 | bypass of daylight filter probably wrong |

Entrance ratio

As mentioned in Sect. 4.4.3 the entrance ratio can be derived from seed laser scans or shorter measurements with stabilized seed laser frequency. The only requirements are: Seed laser light is coupled into the detection system through telescope ports and seed laser port, the iodine-vapor cell is not removed from optical path, and the chopper is on.

Table B.3 lists all calibration measurements to determine the entrance ratio.

Analyzing this table in detail shows: The dichroic mirror D3 affects the entrance ratio slightly (e.g., on 03.05.2010); listing $D_{\text{seeder}}|_{\nu_0}$ allows judging, if the mirrors M1 and M1.c, which steer the light either through the daylight filter or its bypass, are mounted properly (e.g., compare 18.08.2010 to 21.06.2010).

Instrumental modification which led to changes of $D_{\text{seeder}}|_{\nu_0}$, E_{NWT} and E_{SET} are itemized in Sect. B.1.

As mentioned above, the impact of variations of E_{tel} on derived line-of-sight wind speed is considerable: A change of 1% causes a change of line-of-sight wind of about 5 m/s.

Appendix B Calibration in details

Table B.3 List of calibration measurements to determine entrance ratio

| date | day/night | D3 | $D_{\text{seeder}} _{\nu_0}$ | E_{NWT} | E_{SET} | comments |
|----------------|-----------|-----|------------------------------|------------------|------------------|---|
| 25.02.2009 | night | in | 0.8930 | 1.0055 | 1.1280 | restricted to stable RFS |
| 09./10.03.2009 | day | in | – | 1.1582 | 1.1585 | – |
| 18./19.03.2009 | night | out | 1.0091 | 0.9741 | 1.0259 | – |
| 09.09.2009 | night | out | – | 0.9257 | – | – |
| 18.09.2009 | night | out | 1.0055 | 0.9414 | 0.9391 | – |
| 03.11.2009 | night | in | 1.0005 | 0.9487 | 0.9750 | – |
| | day | in | 1.1051 | 0.8612 | 0.8750 | – |
| 11.01.2010 | night | in | 1.0068 | 0.9953 | 0.9973 | – |
| | day | in | 1.0398 | 0.9190 | 0.9415 | restricted to aligned daylight filter |
| 03.05.2010 | night | in | 0.9968 | 0.9805 | 0.9894 | 2nd test on that day |
| | | out | 0.9946 | 0.9775 | 0.9758 | 3rd test on that day |
| | day | in | 1.0388 | 0.9220 | 0.9520 | 1st test on that day |
| | | out | 1.0413 | 0.9175 | 0.9410 | 4th test on that day |
| 19.06.2010 | night | out | 0.9975 | 0.9674 | 0.9754 | – |
| | day | out | 1.0439 | 0.9185 | 0.9450 | – |
| 21.06.2010 | night | out | 1.0031 | 0.9706 | 0.9748 | – |
| | day | out | 1.0450 | 0.9148 | 0.9337 | – |
| 18.08.2010 | night | out | 1.0813 | 0.7290 | 0.9732 | bypass of daylight filter probably wrong |
| | day | out | 0.8055 | 1.1299 | – | bypass of daylight filter probably wrong |
| 06.09.2010 | day | out | 1.0505 | 0.9246 | 0.9516 | – |
| 07.09.2010 | night | out | 1.0176 | 0.9562 | 0.9698 | – |
| 03.12.2010 | night | out | 0.9296 | 0.9617 | 1.0004 | – |
| | day | out | 1.1305 | 0.8469 | 0.8574 | – |
| 18.01.2011 | night | in | 0.9356 | 1.0805 | 0.9984 | NWT fiber 1 mm |
| | day | in | 0.5585 | – | – | NWT fiber 1 mm; bypass of daylight filter probably wrong |
| 27.01.2011 | night | in | 0.9402 | 1.2132 | 0.9877 | NWT fiber 0.5 mm |
| | day | in | 1.1632 | 1.0480 | 0.8566 | NWT fiber 0.5 mm |
| 15.02.2011 | night | in | 0.9458 | 1.0677 | 0.9932 | NWT fiber 0.8 mm |
| | day | in | 1.1631 | 0.8623 | 0.8559 | NWT fiber 0.8 mm |
| 22.06.2011 | night | out | 0.5707 | – | 1.0090 | |
| | day | out | 0.6739 | – | 0.9537 | |
| 31.01.2012 | night | in | 0.5788 | 1.0078 | 1.0281 | – |
| | day | in | 0.6687 | 0.9667 | 0.9543 | – |
| 07.02.2012 | day | in | 0.6713 | 0.9562 | 0.9513 | |
| 08.02.2012 | night | in | 0.5825 | 1.0044 | 1.0284 | – |
| 01.09.2012 | day | in | – | 0.9559 | 0.9352 | daylight filter not aligned |
| 16.09.2012 | night | in | 0.6326 | 1.0053 | 1.0050 | low SET value; bypass of daylight filter probably wrong |

Laser pulse spectrometer

The transmittance spectrum of the iodine-vapor cell of the LPS is measured by varying the seed laser frequency. It is possible to measure the spectrum also with light from the power lasers. Unfortunately, the setup of the LPS does not allow to measure both power lasers and the seed laser simultaneously; this would result in data gaps in each time series. As mentioned in Sect. A.5, the dark fiber (fiber 4) is required to derive the voltage offset of the detectors; it might change during operation as the detectors are getting warmer. For the power laser data the voltage offset can be derived from the pulse form data, fiber 4 is then not needed.

Table B.4 lists all test measurements with the LPS during the years 2009 to 2012.

The data from 18.09.2009 were used to calculate the lookup table which is used to derive the frequency offset during atmospheric measurements (see Sect. 4.5.2).

Table B.4 List of test measurements with the LPS. The labeling of the fibers is: 1: laser 1, 2: laser 2, 3: seed laser, 4: dark.

| date | fibers | comments |
|----------------|--------------|---|
| 21.01.2009 | 1, 2, 3, 4 | all fibers at once; high seed laser signal; no trigger within absorption line |
| 11.02.2009 | 1 | no signal within absorption line |
| 12.02.2009 | 2, 3 | fibers consecutively; high seed laser signal |
| 09.09.2009 | 1, 3 | fibers consecutively; low seed laser signal |
| 18.09.2009 | 1, 2, 3, (4) | fibers consecutively, fiber 4 at beginning and end; low seed laser signal |
| 06.09.2010 | 3, 4 | both fibers at once; poor signal |
| 07.09.2010 | 3, 4 | both fibers at once; poor signal |
| 14.09.2010 | 3, 4 | both fibers at once; poor signal |
| 24.–30.09.2010 | 3, 4 | both fibers at once; poor signal |
| 13.–19.09.2010 | 3, 4 | both fibers at once; poor signal |
| 08.08.2011 | 2 | – |
| 16.11.2012 | 2, 3, 4 | fibers consecutively |

Appendix C Estimates

C.1 Projecting line-of-sight wind to horizontal wind

In Sect. 4.3 two approaches how to calculate horizontal wind from line-of-sight wind and how to include the vertical wind were shortly presented. This section backs the above mentioned conclusions by calculating the horizontal wind and its measurement uncertainty for three different estimates.

To estimate the contribution of vertical wind to line-of-sight wind, it is needed to have a rough idea of how large it actually is. *Widdel* (1987) derived vertical wind speeds between 70 and 90 km altitude using chaff. For a winter campaign at Andenes he stated typical vertical wind speeds of 4–6 m/s. Using Doppler radar with a very narrow beam (0.6° by 1.7°) *Hoppe and Fritts* (1995) derived vertical wind speeds of 2–3 m/s in the altitude range 80–92 km during Arctic summer. *Yuan et al.* (2009) show vertical winds measured by sodium resonance lidar: For an integration time of 2.5 h the mean value in the height range 85–100 km is less than 1 m/s; the discussed observation shows a wavy structure with an amplitude of 2 m/s.

For the following estimates we assume vertical wind speed to be less or similar 2 m/s, its spatial and temporal variability are of the same order. The measurement uncertainty for line-of-sight wind is 2–5 m/s (for calculations we use 3.5 m/s). For off-zenith measurements the zenith-distance angle θ is 20°.

$$w = w_{\text{variability}} \lesssim 2 \text{ m/s} \quad (\text{C.1a})$$

$$\Delta v_{\text{l.o.s.}} \approx 3.5 \text{ m/s} \quad (\text{C.1b})$$

$$\theta = 20^\circ \quad (\text{C.1c})$$

Now we first simply assume the vertical wind to be zero ($w = 0$). Horizontal wind u and its measurement uncertainty Δu are then given by:

$$u = \frac{1}{\sin \theta} \cdot v_{\text{l.o.s.}}, \quad (\text{C.2a})$$

$$\Delta u = \frac{1}{\sin \theta} \cdot \Delta v_{\text{l.o.s.}} \quad (\text{C.2b})$$

$$\approx 10 \text{ m/s}. \quad (\text{C.2c})$$

Projecting the off-zenith measurement onto the horizontal plane leads to a measurement uncertainty of horizontal wind of 10 m/s.

In the second estimate we take the vertical wind into account when projecting line-of-sight

Appendix c Estimates

wind onto the horizontal plane. For estimation of measurement uncertainty we also regard the variability of vertical wind, since it is measured in a different air volume (and maybe also at a different time). The horizontal wind follows from:

$$v_{l.o.s.} = u \cdot \sin \theta + w \cdot \cos \theta, \quad (C.3a)$$

$$u = \frac{1}{\sin \theta} \cdot v_{l.o.s.} - \frac{\cos \theta}{\sin \theta} \cdot w \quad (C.3b)$$

$$\approx \frac{1}{\sin \theta} \cdot v_{l.o.s.} - 5.5 \text{ m/s}. \quad (C.3c)$$

We see that the previous estimate over- or underestimates the horizontal wind by $\approx 5.5 \text{ m/s}$, this is half as much as the previously estimated measurement uncertainty. The measurement uncertainty for the second approach is calculated as follows:

$$\Delta u = \sqrt{\left(\frac{1}{\sin \theta} \cdot \Delta v_{l.o.s.}\right)^2 + \left(\frac{\cos \theta}{\sin \theta} \cdot \Delta w\right)^2} \quad (C.4a)$$

$$= \sqrt{\left(\frac{1}{\sin \theta} \cdot \Delta v_{l.o.s.}\right)^2 + \left(\frac{\cos \theta}{\sin \theta}\right)^2 \left((\Delta v_{l.o.s.})^2 + w_{\text{variability}}^2\right)} \quad (C.4b)$$

$$= \sqrt{\frac{1 + \cos^2 \theta}{\sin^2 \theta} \cdot (\Delta v_{l.o.s.})^2 + \frac{\cos^2 \theta}{\sin^2 \theta} \cdot w_{\text{variability}}^2} \quad (C.4c)$$

$$\approx \sqrt{16 \cdot 12 \text{ (m/s)}^2 + 7.5 \cdot 4 \text{ (m/s)}^2} \quad (C.4d)$$

$$\approx 15 \text{ m/s}. \quad (C.4e)$$

By strictly taking vertical wind and its variability into account the measurement uncertainty for horizontal wind gets 1.5 times larger than when neglecting the vertical wind and its variability.

The third estimate corresponds to the approach by *Liu et al. (2002)*: neglecting vertical wind for projection of line-of-sight wind onto the horizontal plane, but regard its variability for estimation of measurement uncertainty of horizontal wind. The horizontal wind is the same like for the first estimate, see Eq. (C.2a), but its measurement uncertainty is somewhat different:

$$\Delta u = \sqrt{\left(\frac{1}{\sin \theta} \cdot \Delta v_{l.o.s.}\right)^2 + \left(\frac{\cos \theta}{\sin \theta} \cdot \Delta w_{\text{variability}}\right)^2} \quad (C.5a)$$

$$\approx \sqrt{8.5 \cdot 12 \text{ (m/s)}^2 + 7.5 \cdot 4 \text{ (m/s)}^2} \quad (C.5b)$$

$$\approx 12 \text{ m/s}. \quad (C.5c)$$

As expected, the measurement uncertainty for this estimate is smaller than for the second estimate but larger than for the first one.

Summary

Taking the vertical wind not into account results in slightly over- or underestimated horizontal winds ($\approx 5.5 \text{ m/s}$, for off-zenith angle of 20°). Since the measurement uncertainty for horizontal wind is $\approx 10 \text{ m/s}$, this overestimation does not really matter; especially since horizontal winds can reach wind speeds of many 10 m/s . Taking the vertical wind into account

c.2 Different approaches to derive temperature deviations

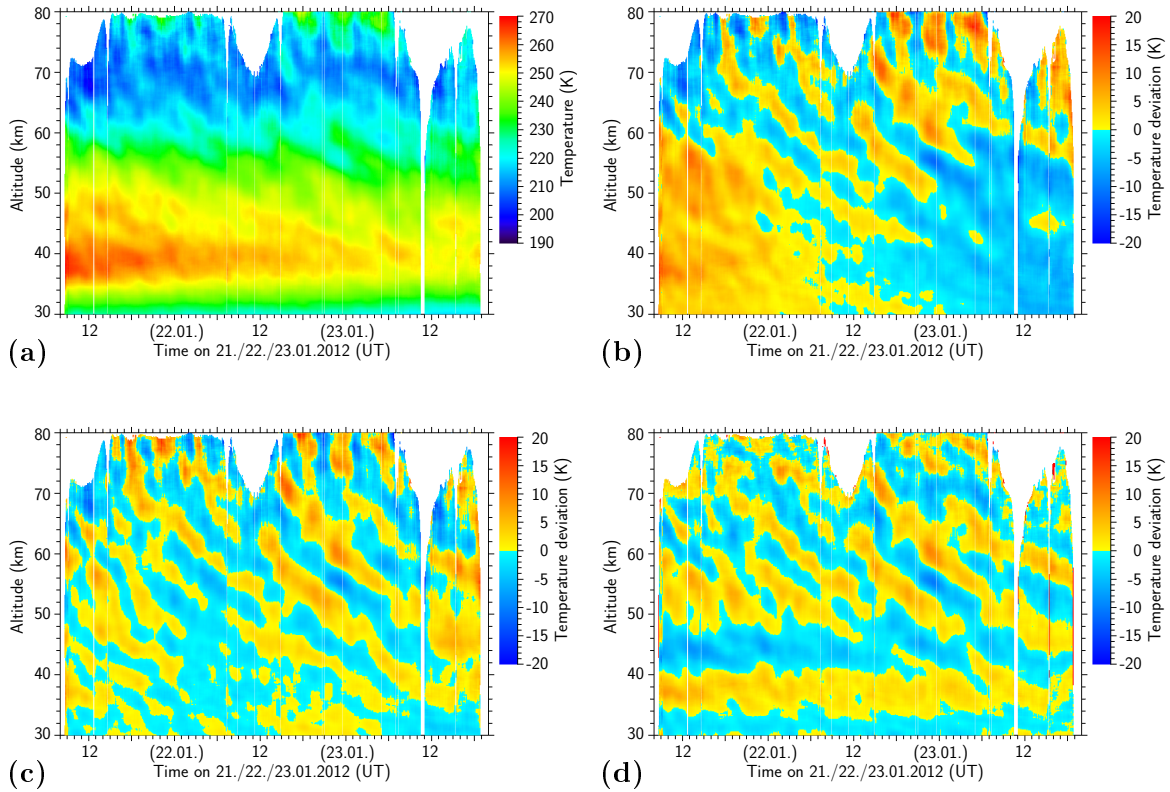


Figure C.1 Different methods to derive temperature deviations: (a) absolute temperature; (b) mean altitude profile subtracted; (c) linear approximation at each altitude level subtracted; (d) polynomial approximation at each time step subtracted.

increases the uncertainty of horizontal wind speed by a factor of ≈ 1.5 . This is due to the measurement uncertainty of the additional wind measurement and due to the temporal and spatial variability of the vertical wind (it is not possible to measure vertical wind at same time and place as horizontal wind). The uncertainty due to the additional wind measurement is a little bit higher than the uncertainty due to the wind variability.

C.2 Different approaches to derive temperature deviations

This section presents three approaches to calculate deviation, with temperature measurement during long measurement on 21.–23.01.2012 as example. Figure C.1 shows time-height sections of absolute temperature and its deviation. Some wavy structures become slightly apparent already in absolute temperature (panel (a)); e.g., during the second night around 60 km altitude.

Panel (b) shows the simplest approach to emphasize wavy structures: subtracting the mean altitude profile of temperature. But since there is a long periodic change of temperature (especially around the stratopause temperature decreases remarkably), the deviation is dominated by positive deviation at the beginning and negative deviation at the end. Hence, wavy structures are hardly noticeable during these periods.

Next idea is to mask the long periodic change. For this we separate the matrix of absolute

Appendix C Estimates

temperature over time and altitude into altitude slices of temperature over time. For each slice we approximate the temporal evolution with a straight line, i.e., a linear fit. Then we subtract for each point along the time axis the fitted temperature from the actual measured temperature, i.e., calculate the temperature residual. Finally we stack all the slices of temperature residuals and obtain a time-height section of temperature deviation. The result is shown in Fig. C.1(c). In the middle of the measurement the wavy structures look similar to the ones obtain by previous approach (cf. panel (b)); additionally wavy structures are clearly visible at the beginning and end of the measurement.

A third approach takes up the idea presented in Sect. 5.2.2 for single altitude profiles. It is in some way similar to the previous one, but acts in altitude dimension of the time-height section instead of the time dimension. We separate the matrix into time slices of temperature against altitude. For each slice we approximate the undisturbed altitude profile by a fourth order polynomial. Then we subtract this polynomial from the actually measured temperature profile, building the temperature residual. Finally we append all the slices and obtain again a time-height section of temperature deviation. The result is shown in Fig. C.1(d). Again we identify similar wavy structures in the middle of the measurement. But one thing is striking, and counterintuitive: There is a persistent positive deviation at the stratopause altitude and negative deviation above. This is not consistent with propagating gravity waves, but an artefact of deriving deviation by using a fourth order polynomial.

To summarize, the second approach (subtracting for each altitude the linearly approximated temporal evolution) yields best results: signatures of waves are clearly visible in the whole time and altitude range.

Appendix D Detailed wind results

D.1 Vertical wind measurements

In Tabs. D.1 and D.2 all vertical wind measurements that were performed during the years 2009 to 2012 which last for at least 1 h.

The tables include for internal and atmospheric calibration the entrance ratio E_{tel} , the mean vertical wind $\langle w \rangle$ in the altitude range 45–65 km and the standard deviation σ_w (typical measurement uncertainties of the vertical wind speeds are on the order of 0.5–3 m/s, depending on altitude range and integration time). Additionally, the averaged seeder Doppler ratio D_{seeder} is denoted; it can be used to judge if the mirrors of the daylight filter bypass were mounted properly (note that the significant decrease between February and April 2011 is caused by change of stabilization frequency ν_0).

Table D.1 Nighttime measurements of vertical pointing NWT which last for 1 h or longer. See text for details.

| date | D_{seeder} | $E_{\text{tel, int}}$ | $E_{\text{tel, atm}}$ | $\langle w_{\text{int}} \rangle$ (m/s) | $\sigma_{w, \text{int}}$ (m/s) | $\langle w_{\text{atm}} \rangle$ (m/s) | $\sigma_{w, \text{atm}}$ (m/s) |
|------------|---------------------|-----------------------|-----------------------|---|-----------------------------------|---|-----------------------------------|
| 04.03.2009 | 0.9204 | 1.0055 | 1.0136 | -4.04 | 2.83 | -0.02 | 2.84 |
| 26.11.2010 | 0.9485 | 0.9617 | 1.0097 | -26.62 | 1.61 | -0.02 | 1.02 |
| 28.11.2010 | 0.9466 | 0.9617 | 1.0173 | -30.65 | 3.32 | -0.01 | 3.83 |
| 05.12.2010 | 0.9445 | 0.9617 | 1.0335 | -39.29 | 5.56 | 0.02 | 5.18 |
| 07.12.2010 | 0.9434 | 0.9617 | 1.0239 | -34.99 | 2.12 | -0.01 | 2.36 |
| 09.12.2010 | 0.9389 | 0.9617 | 1.0151 | -29.71 | 2.90 | 0.00 | 3.07 |
| 11.01.2011 | 0.9409 | 1.0805 | 1.1136 | -17.06 | 2.47 | 0.02 | 2.91 |
| 25.01.2011 | 0.9361 | 1.0805 | 1.1116 | -14.28 | 1.81 | -0.02 | 1.84 |
| 09.02.2011 | 0.9479 | 1.2132 | 1.2417 | -12.02 | 3.11 | -0.01 | 3.14 |
| 14.02.2011 | 0.9446 | 1.2132 | 1.2343 | -8.85 | 1.48 | 0.01 | 1.79 |
| 20.02.2011 | 0.9530 | 1.0677 | 1.0842 | -8.05 | 2.22 | 0.03 | 2.31 |
| 23.02.2011 | 0.9468 | 1.0677 | 1.0880 | -10.09 | 2.34 | -0.01 | 2.47 |
| 04.11.2011 | 0.5798 | 1.0061 | 1.0492 | -22.18 | 2.02 | 0.00 | 2.12 |
| 24.01.2012 | 0.5882 | 1.0061 | 1.0293 | -10.81 | 1.49 | 0.02 | 1.29 |
| 28.01.2012 | 0.5876 | 1.0061 | 1.0290 | -10.96 | 1.10 | 0.00 | 1.11 |
| 01.02.2012 | 0.5776 | 1.0061 | 1.0397 | -16.41 | 2.24 | 0.01 | 2.17 |
| 03.02.2012 | 0.5769 | 1.0061 | 1.0383 | -15.97 | 1.09 | -0.02 | 1.10 |
| 05.02.2012 | 0.5774 | 1.0061 | 1.0407 | -16.80 | 1.83 | 0.00 | 1.56 |
| 06.12.2012 | 0.6678 | 1.0053 | 1.0094 | -2.29 | 0.97 | -0.02 | 0.89 |

Appendix D Detailed wind results

Table D.2 Nighttime measurements of vertical pointing SET which last for 1 h or longer. See text for details.

| date | D_{seeder} | $E_{\text{tel, int}}$ | $E_{\text{tel, atm}}$ | $\langle w_{\text{int}} \rangle$ (m/s) | $\sigma_{w, \text{int}}$ (m/s) | $\langle w_{\text{atm}} \rangle$ (m/s) | $\sigma_{w, \text{atm}}$ (m/s) |
|------------|---------------------|-----------------------|-----------------------|---|-----------------------------------|---|-----------------------------------|
| 17.01.2009 | 0.9064 | 1.1280 | 1.1562 | -13.02 | 1.74 | -0.02 | 1.40 |
| 19.01.2009 | 0.8910 | 1.1280 | 1.1757 | -20.24 | 1.45 | -0.02 | 0.97 |
| 22.01.2009 | 0.9014 | 1.1280 | 1.1677 | -16.93 | 1.38 | -0.01 | 1.21 |
| 23.01.2009 | 0.8904 | 1.1280 | 1.1738 | -19.15 | 1.25 | -0.01 | 1.14 |
| 25.01.2009 | 0.8884 | 1.1280 | 1.1780 | -20.48 | 1.62 | 0.01 | 1.85 |
| 04.03.2009 | 0.9231 | 1.1280 | 1.1707 | -18.62 | 1.69 | 0.01 | 1.48 |
| 26.11.2010 | 0.9487 | 1.0004 | 0.9741 | 14.55 | 2.11 | -0.03 | 1.97 |
| 28.11.2010 | 0.9464 | 1.0004 | 0.9796 | 11.47 | 3.16 | 0.00 | 2.39 |
| 05.12.2010 | 0.9434 | 1.0004 | 0.9891 | 6.14 | 5.53 | -0.03 | 5.62 |
| 07.12.2010 | 0.9431 | 1.0004 | 0.9826 | 10.01 | 2.99 | -0.00 | 2.76 |
| 09.12.2010 | 0.9396 | 0.9931 | 0.9845 | 4.81 | 2.75 | 0.03 | 2.69 |
| 11.01.2011 | 0.9415 | 0.9931 | 0.9890 | 2.31 | 2.36 | -0.02 | 2.30 |
| 25.01.2011 | 0.9370 | 0.9931 | 0.9813 | 6.00 | 1.47 | 0.02 | 1.39 |
| 09.02.2011 | 0.9489 | 0.9931 | 0.9851 | 4.22 | 2.88 | -0.01 | 2.75 |
| 14.02.2011 | 0.9449 | 0.9931 | 0.9778 | 7.98 | 2.78 | -0.02 | 2.23 |
| 20.02.2011 | 0.9540 | 0.9931 | 0.9856 | 4.02 | 3.19 | 0.02 | 3.15 |
| 23.02.2011 | 0.9464 | 0.9931 | 0.9766 | 9.00 | 3.18 | 0.02 | 2.88 |
| 05.04.2011 | 0.5622 | 1.0284 | 1.0372 | -4.85 | 4.20 | 0.01 | 4.46 |
| 04.11.2011 | 0.5798 | 1.0090 | 1.0199 | -5.70 | 1.72 | -0.00 | 1.78 |
| 08.12.2011 | 0.5821 | 1.0090 | 1.0247 | -8.44 | 0.46 | 0.01 | 0.41 |
| 09.12.2011 | 0.6032 | 1.0090 | 1.0616 | -27.61 | 1.19 | -0.02 | 0.74 |
| 13.12.2011 | 0.6057 | 1.0090 | 1.0564 | -25.31 | 0.95 | -0.02 | 0.69 |
| 16.12.2011 | 0.6068 | 1.0090 | 1.0614 | -27.56 | 1.18 | 0.02 | 1.09 |
| 06.01.2012 | 0.5826 | 1.0090 | 1.0262 | -9.32 | 0.92 | -0.00 | 0.58 |
| 24.01.2012 | 0.5883 | 1.0090 | 1.0491 | -18.82 | 1.33 | 0.01 | 1.84 |
| 28.01.2012 | 0.5877 | 1.0090 | 1.0486 | -18.88 | 1.22 | 0.00 | 1.37 |
| 01.02.2012 | 0.5779 | 1.0283 | 1.0571 | -13.80 | 3.09 | 0.03 | 3.31 |
| 03.02.2012 | 0.5771 | 1.0283 | 1.0543 | -12.51 | 2.03 | 0.02 | 2.05 |
| 05.02.2012 | 0.5775 | 1.0283 | 1.0551 | -12.84 | 1.18 | 0.00 | 1.19 |
| 20.11.2012 | 0.6652 | 1.0050 | 0.9916 | 6.97 | 0.80 | -0.02 | 0.82 |
| 05.12.2012 | 0.6673 | 1.0050 | 0.9761 | 15.60 | 0.56 | -0.03 | 0.48 |

As mentioned above, the frequency of laser 1 showed some jitter or even 2-mode behavior in winters 2010/2011 and 2011/2012. This causes the large deviations of $\langle w_{\text{int}} \rangle$ in Tab. D.1. Note that $\langle w_{\text{int}} \rangle$ and $\sigma_{w, \text{int}}$ are close to zero on 06.12.2012. The vertical wind is close to zero even though the bypass of the daylight filter was installed improperly (D_{seeder} is unusual large) since during the calibration measurement on 16.09.2012 (which is used for the analysis on that day) the bypass was installed improperly as well (see Tab. B.3).

Laser 2 did not show such problems like laser 1, but the measurements with SET (Tab. D.2) are affected by the behavior of the rotary fiber selector (RFS). A jitter of the RFS became apparent in February 2009, probably earlier measurements were affected too. The complete

RFS was replaced in summer 2011. During December 2011 and November/December 2012 the measurements were affected by improperly installed bypass of the daylight filter. The measurements between December 2010 and December 2011 show small values of $|\langle w_{\text{int}} \rangle|$ below 10 m/s.

D.2 Coplanar wind measurements

Table D.3 lists all nighttime measurements from the years 2009 to 2012 with coplanar pointing telescopes, that last for at least 1 h. During all of these measurements the NWT pointed to west and the SET pointed to east. The table lists the averaged seeder Doppler ratio D_{seeder} and the difference of the independently derived zonal wind speeds in different altitude ranges $\langle u_{\text{NWT}} - u_{\text{SET}} \rangle|_{z_1-z_2}$. Typical measurement uncertainties of the zonal wind speeds are on the order of 3–10 m/s (depending on altitude range and integration time).

In January 2009 internal calibration was used for NWT and atmospheric calibration for SET. For the measurement on 05.03.2009 atmospheric calibration was used; but it might be affected by a jitter of the RFS. In November 2009 only internal calibration could be used; these measurements might also be affected by a jitter of the RFS, on 30.11.2009 the bypass of the daylight filter might be installed improperly (D_{seeder} is somewhat smaller than during mid of November). For the measurement on 19.01.2012 atmospheric calibration is used; but it is affected by jitter of the frequency of laser 1. However, the difference between u_{NWT} and u_{SET} is relatively small during that measurement. The measurements from January 2009 show good agreement of the zonal wind speeds measured by NWT and SET, too. The relatively large difference in the altitude range 50–60 km on 25.01.2009 is attributed to gravity waves (*Hildebrand et al.*, 2012).

Table D.3 Nighttime measurements with both telescopes pointing coplanar which last for longer than 1 h. See text for details.

| date | time | D_{seeder} | $\langle u_{\text{NWT}} - u_{\text{SET}} \rangle _{z_1-z_2}$ (m/s) | | | |
|----------------|-------------|---------------------|--|----------|----------|----------|
| | | | 40–50 km | 50–60 km | 60–70 km | 40–70 km |
| 25.01.2009 | 03:15–07:20 | 0.888 | 9.02 | 19.45 | 6.63 | 12.29 |
| 26./27.01.2009 | 16:35–04:00 | 0.893 | −3.52 | 8.15 | 2.06 | 2.77 |
| 27./28.01.2009 | 17:25–02:35 | 0.894 | −5.57 | 1.28 | −4.75 | −2.55 |
| 05.03.2009 | 00:50–02:10 | 0.923 | −19.29 | 1.07 | −14.52 | −9.69 |
| 17./18.11.2009 | 22:10–00:05 | 0.999 | −9.19 | 3.36 | 25.29 | 3.37 |
| 18.11.2009 | 15:05–19:05 | 0.998 | 5.95 | 21.92 | 39.69 | 19.36 |
| 18.11.2009 | 20:25–22:00 | 0.998 | 19.07 | 37.95 | 65.55 | 35.97 |
| 19.11.2009 | 22:10–23:55 | 1.000 | 19.89 | 31.73 | 52.06 | 30.60 |
| 30.11.2009 | 18:25–20:30 | 0.986 | 31.76 | 50.31 | 69.26 | 46.77 |
| 30.11.2009 | 21:45–00:00 | 0.986 | 25.95 | 41.39 | 70.11 | 40.23 |
| 19.01.2012 | 19:50–22:05 | 0.582 | −5.68 | −8.45 | −15.19 | −9.09 |

D.3 Winds and temperatures in Arctic winter

D.3.1 Cumulated monthly mean winds and temperatures in Arctic winter

This section only completes the discussion from Sect. 6.1.1 for the months December and March. The months November, January, and February were discussed in Sect. 6.1.1.

December, Fig. D.1(b) The zonal wind measured by lidar matches the ECMWF data, except below 42 km altitude and above 64 km altitude. While the lower part might again be affected by catenation of detectors, the upper part is ambiguous: The radar wind profiles are between lidar profile and ECMWF profile. The meridional wind derived by lidar is too small compared to ECMWF in the entire altitude range.

March, Fig. D.1(e) The zonal wind derived by lidar is too small compared to the ECMWF data above 50 km altitude. This is dominated by 30 profiles of 2010, while the 6 profiles of 2009 match ECMWF and radar data very good. The mean meridional wind measured by lidar matches the ECMWF data, except above 65 km altitude. Again, this is dominated by 2010, while the mean winds during all other years match the respective ECMWF and radar profiles.

D.3.2 Monthly mean winds and temperatures in Arctic winter for the years 2009 to 2012

This section shortly discusses only selected single months, for which the wind speeds derived by lidar remarkable differ from other data sets.

In **December 2009 (Fig. D.2(e))** the intensity of the seed laser light on the detection system was weak, this yields short scale fluctuations of the seeder Doppler ratio and therefore uncertainties in the retrieved winds.

In **February 2010 (Fig. D.3(b))** there is some offset between lidar wind and ECMWF wind. This might be caused by unstable RFS. Unfortunately there were no vertical wind measurements performed in that season. Therefore, the internal calibration could not be validated.

In **March 2011 (Fig. D.4(c))** only one nighttime measurement was performed (11.03.2011). During that measurement the seeder Doppler ratio shows some short scale fluctuations, the seed laser signal on the detection bench was very weak: Either the bypass of the daylight filter was installed improperly or the intensity of the seed laser was reduced.

In **November 2011 (Fig. D.4(d))** the single measurement on 04.11.2011 suffers from remarkable jitter of the frequency of laser 1. Therefore the meridional wind differs from the ECMWF profile.

In **March 2012 (Fig. D.5(c))** laser 1 shows some remarkable jitter. Additionally the seeder Doppler ratio shows pronounced variation on a time scale of 1 to 2 h; the reason is yet unknown.

In **December 2012 (Fig. D.5(d))** the seeder Doppler ratio is slightly too large. Probably the bypass of the daylight filter was installed improperly.

D.3 Winds and temperatures in Arctic winter

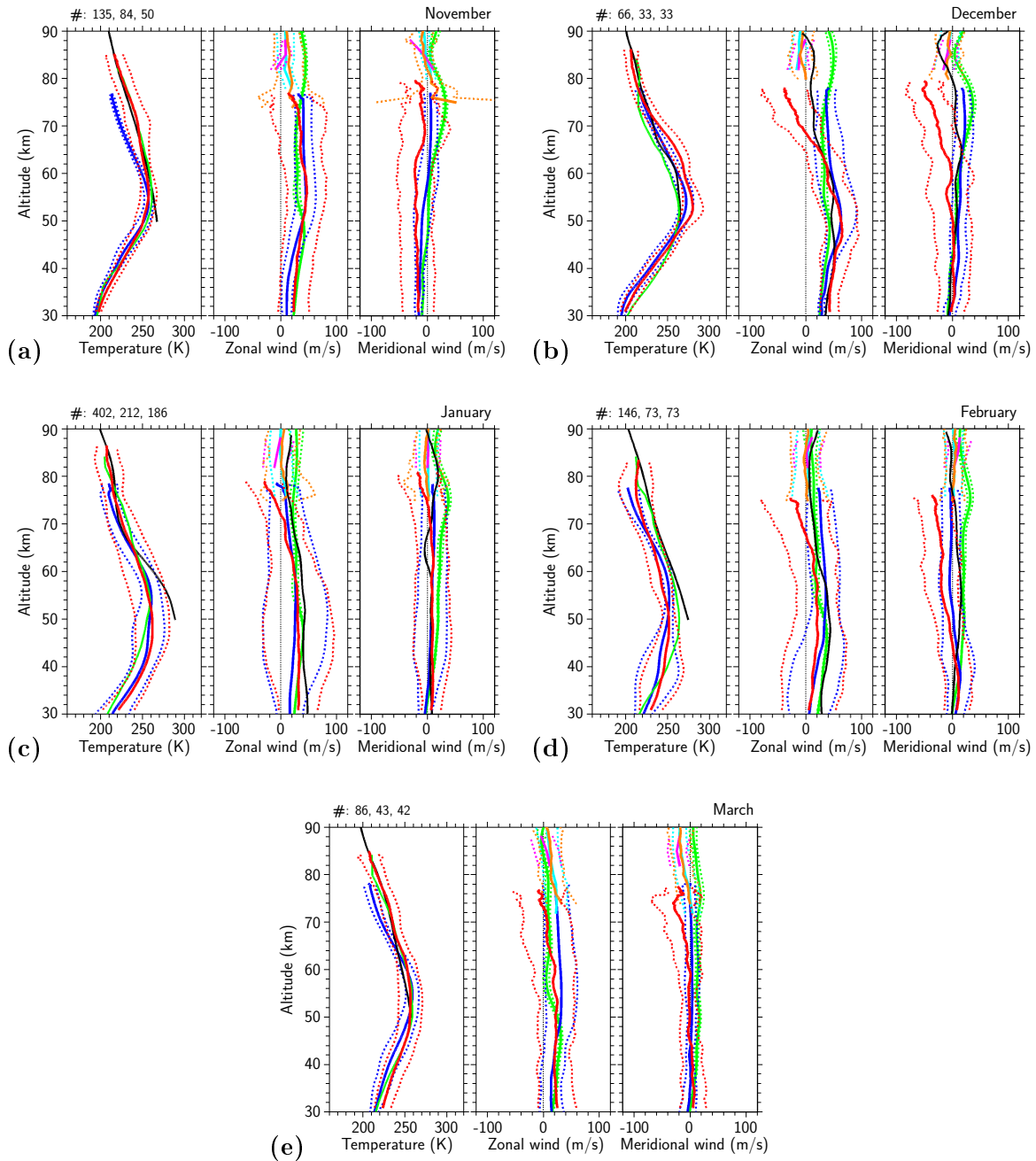


Figure D.1 Over the years 2009–2012 cumulated monthly mean temperatures and horizontal winds for the months November (a), December (b), January (c), February (d), and March (e). Red: ALOMAR RMR lidar, orange: Saura MF radar, cyan: Andenes MF radar, magenta: SKiYMET radar, blue: ECMWF, green: *Sch08* for temperatures, HWM07 for winds, black: meteorological rockets (*LvZ91* for temperatures, *Mey87* for winds). Dotted lines denote the respective standard deviation. The three numbers in the upper left corner indicate the number of lidar profiles included in the panels for temperature, zonal wind speed, and meridional wind speed, respectively.

Appendix D Detailed wind results

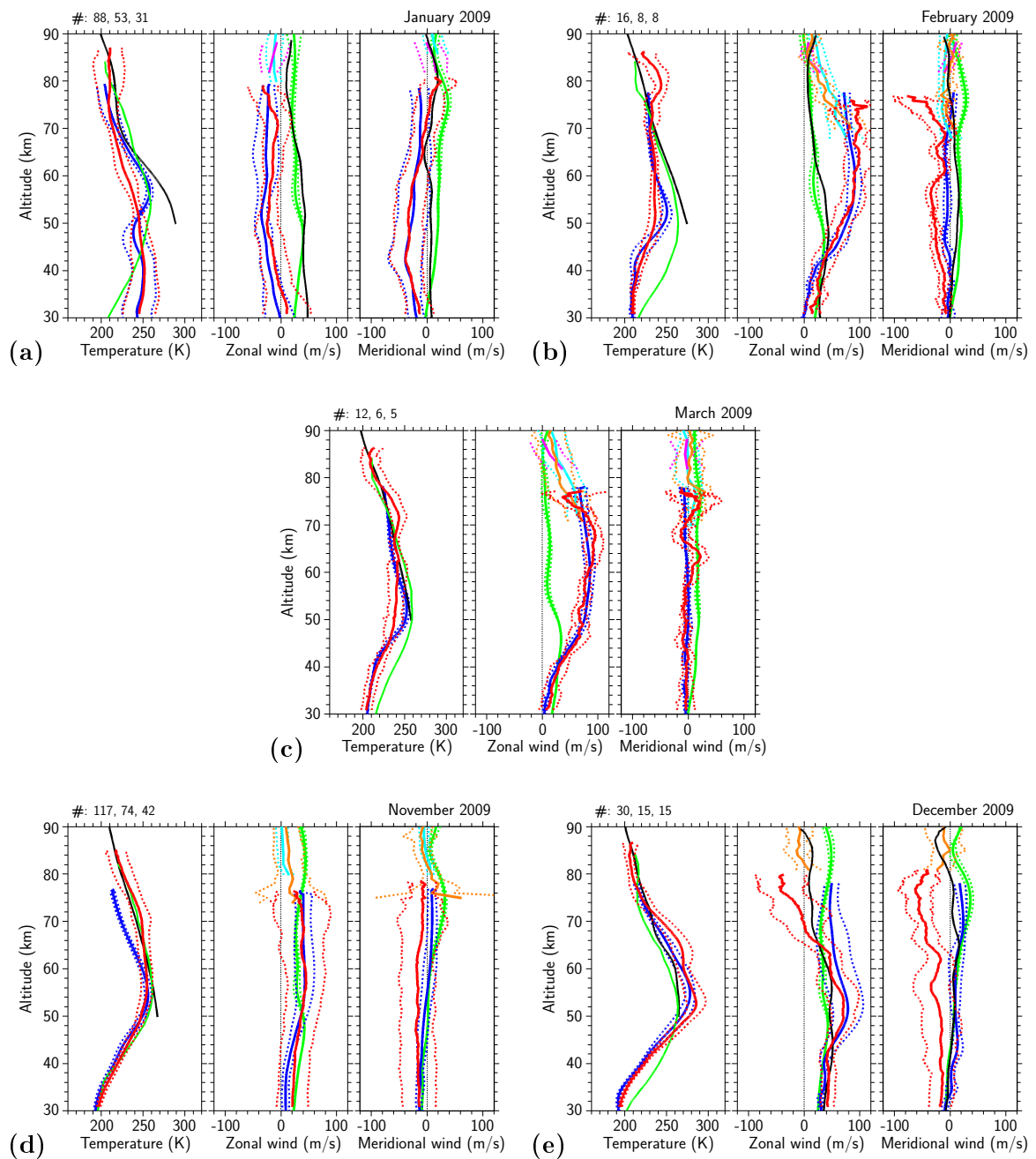


Figure D.2 Monthly mean temperatures and horizontal winds for 2009. Colors like in Fig. D.1

D.3 Winds and temperatures in Arctic winter

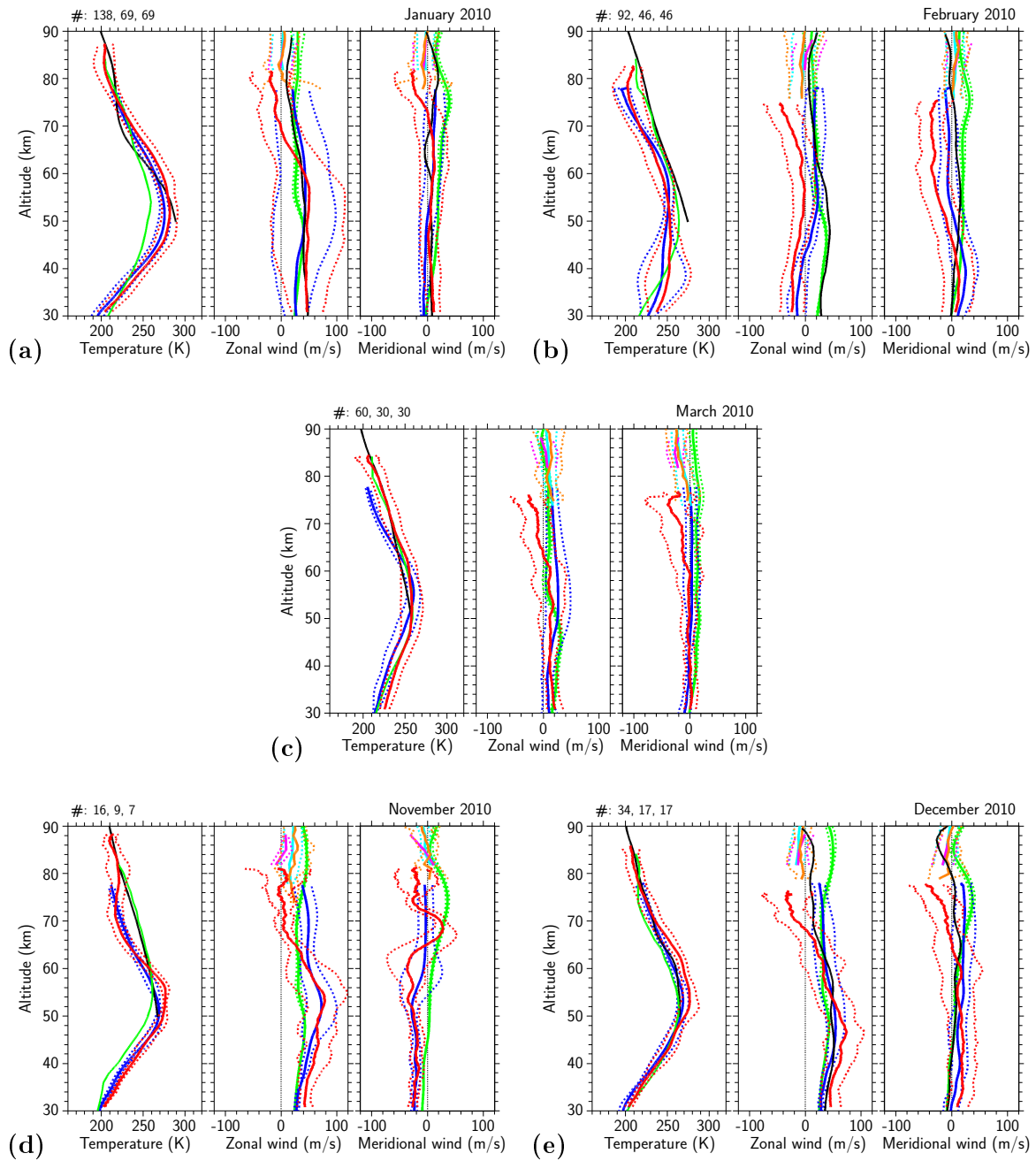


Figure D.3 Monthly mean temperatures and horizontal winds for 2010. Colors like in Fig. D.1

Appendix D Detailed wind results

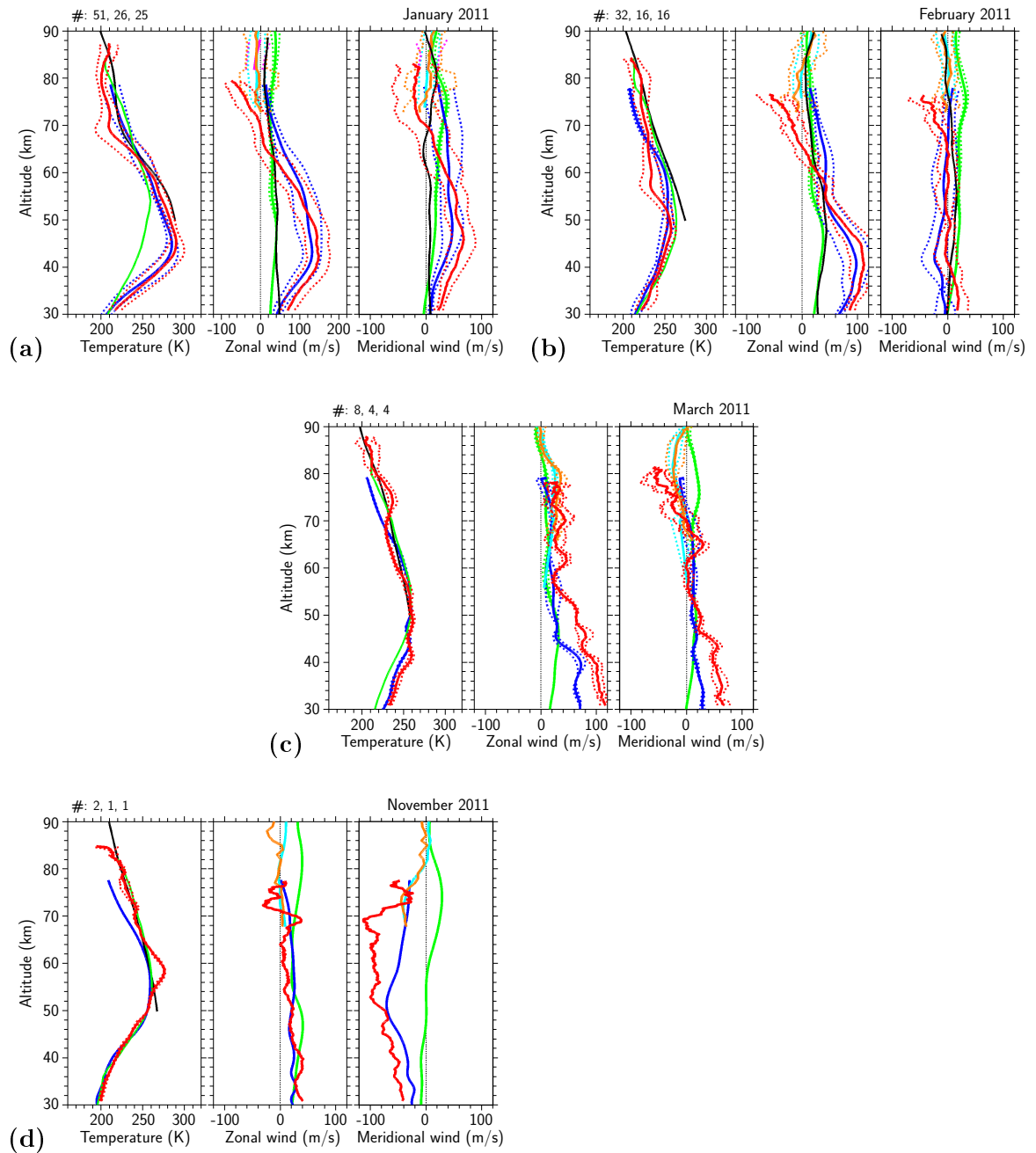


Figure D.4 Monthly mean temperatures and horizontal winds for 2011. Colors like in Fig. D.1

D.3 Winds and temperatures in Arctic winter

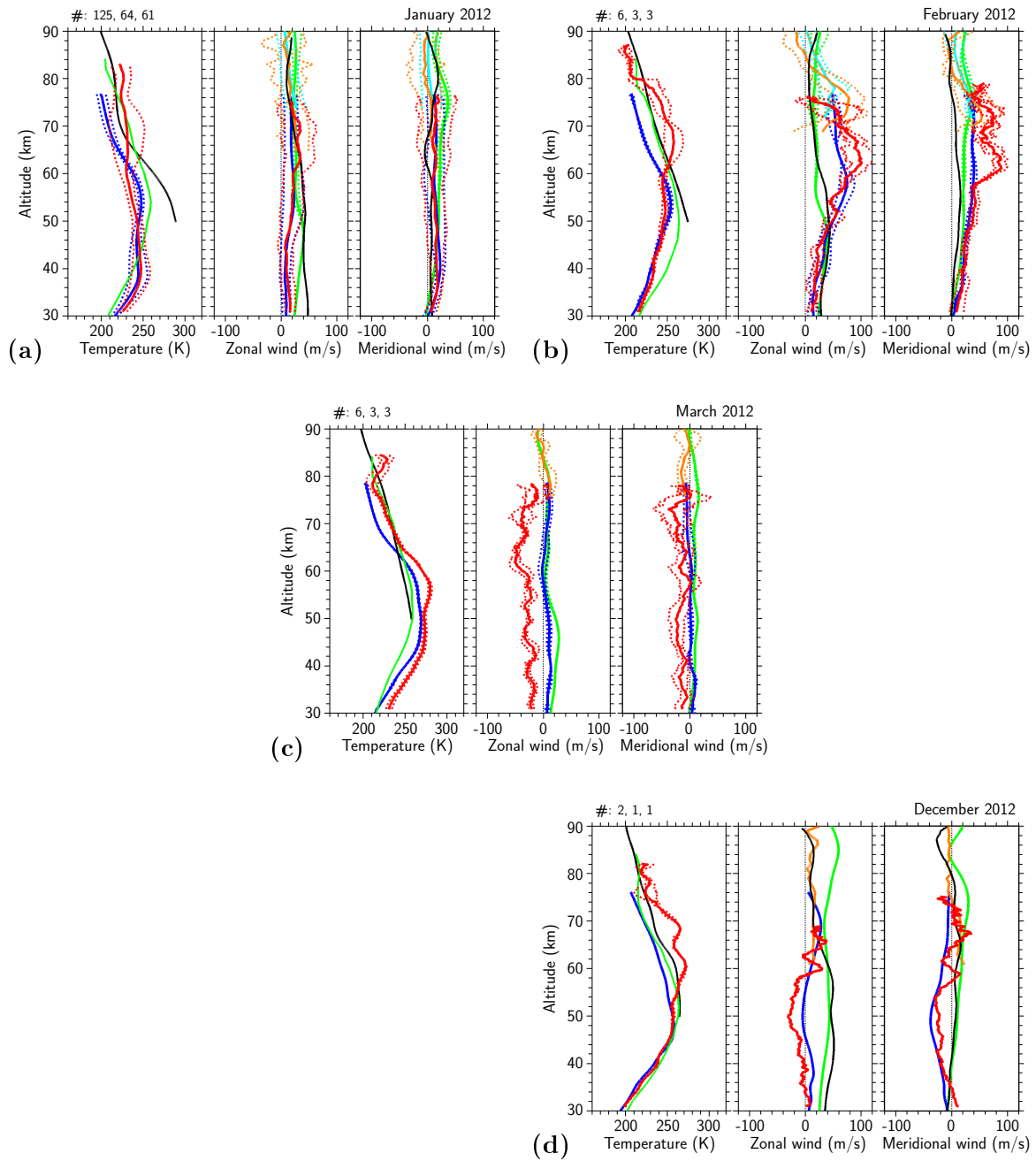


Figure D.5 Monthly mean temperatures and horizontal winds for 2012. Colors like in Fig. D.1

Bibliography

- Baron, P., D. P. Murtagh, J. Urban, H. Sagawa, S. Ochiai, Y. Kasai, K. Kikuchi, F. Khosrawi, H. Körnich, S. Mizobuchi, K. Sagi, and M. Yasui, Observation of horizontal winds in the middle-atmosphere between 30° S and 55° N during the northern winter 2009–2010, *Atmos. Chem. Phys.*, *13*(12), 6049–6064, doi:10.5194/acp-13-6049-2013, 2013.
- Barth, C. A., The 5577-Ångstrom airglow, *Science*, *134*, 1426, 1961.
- Bates, D. R., Rayleigh scattering by air, *Planet. Space Sci.*, *32*(6), 785–790, doi:http://dx.doi.org/10.1016/0032-0633(84)90102-8, 1984.
- Baumgarten, G., Leuchtende Nachtwolken an der polaren Sommermesopause: Untersuchungen mit dem ALOMAR Rayleigh/Mie/Raman Lidar, Ph.D. thesis, Universität Bonn, 2001.
- Baumgarten, G., Doppler Rayleigh Iodine System (DoRIS), *Project proposal for DFG (BA 2834/1-1)*, 2005.
- Baumgarten, G., Doppler Rayleigh/Mie/Raman lidar for wind and temperature measurements in the middle atmosphere up to 80 km, *Atmos. Meas. Tech.*, *3*, 1509–1518, 2010.
- Chandran, A., R. R. Garcia, R. L. Collins, and L. C. Chang, Secondary planetary waves in the middle and upper atmosphere following the stratospheric sudden warming event of January 2012, *Geophys. Res. Lett.*, *40*, 1861–1867, doi:10.1002/grl.50373, 2013.
- Chanin, M.-L., A. Garnier, A. Hauchecorne, and J. Porteneuve, A Doppler lidar for measuring winds in the middle atmosphere, *Geophys. Res. Lett.*, *16*, 1273–1276, doi:10.1029/GL016i011p01273, 1989.
- Cot, C., and J. Barat, Wave-turbulence interaction in the stratosphere, *J. Geophys. Res.*, *91*(D2), 2749–2756, 1986.¹
- Drob, D. P., J. T. Emmert, G. Crowley, J. M. Picone, G. G. Shepherd, W. Skinner, P. Hays, R. J. Niecejewski, M. Larsen, C.-Y. She, J. W. Meriwether, G. Hernandez, M. J. Jarvis, D. P. Sipler, C. A. Tepley, M. S. O'Brien, J. R. Bowman, Q. Wu, Y. Murayama, S. Kawamura, I. M. Reid, and R. A. Vincent, An empirical model of the Earth's horizontal wind fields: HWM07, *J. Geophys. Res.*, 2008.
- Egeland, A. (Ed.), *Historien om Andøya Rakettskytefelt*, Andøya Rakettskytefelt AS, Andenes, 2000.

¹Cot, C., and J. Barat, Wave-Turbulence Interaction in the Stratosphere: A Case Study, *J. Geophys. Res.*, *91*(D2), 2749–2756, 1986.

Bibliography

- Engel, A., T. Möbius, H. Bönisch, U. Schmidt, R. Heinz, I. Levin, E. Atlas, S. Aoki, T. Nakazawa, S. Sugawara, F. Moore, D. Hurst, J. Elkins, S. Schauffler, A. Andrews, and K. Boering, Age of stratospheric air unchanged within uncertainties over the past 30 years, *Nat. Geosci.*, *2*, 28–31, doi:10.1038/NGEO388, 2009.
- Fiedler, J., and G. von Cossart, Automated Lidar Transmitter for Multiparameter Investigations Within the Arctic Atmosphere, *IEEE Trans. Geosci. Remote Sensing*, *37*, 748–755, 1999.
- Fiedler, J., G. Baumgarten, and G. von Cossart, A middle atmosphere lidar for multi-parameter measurements at a remote site, in *Reviewed and revised papers presented at the 24th International Laser Radar Conference*, pp. 824–827, 2008.
- Fiedler, J., G. Baumgarten, U. Berger, P. Hoffmann, N. Kaifler, and F.-J. Lübken, NLC and the background atmosphere above ALOMAR, *Atmos. Chem. Phys.*, pp. 5701–5717, doi:10.5194/acp-11-5701-2011, 2011.
- Franke, S. J., X. Chu, A. Z. Liu, and W. K. Hocking, Comparison of meteor radar and Na Doppler lidar measurements of winds in the mesopause region above Maui, Hawaii, *J. Geophys. Res.*, *110*, D09S02, doi:10.1029/2003JD004486, 2005.
- Fricke, K. H., and U. von Zahn, Mesopause temperatures derived from probing the hyperfine structure of the D₂ resonance line of sodium by lidar, *J. Atmos. Terr. Phys.*, *47*(5), 499–512, doi:10.1016/0021-9169(85)90116-3, 1985.
- Friedman, J. S., C. A. Tepley, P. A. Castleberg, and H. Roe, Middle-atmospheric Doppler lidar using an iodine-vapor edge filter, *Opt. Lett.*, *22*, 1648–1650, 1997.
- Frioud, M., M. Gausa, G. Baumgarten, J. E. Kristjansson, and I. Føre, New Tropospheric LIDAR System in Operation at ALOMAR (69°N, 16°E), in *Reviewed and revised papers presented at the 23rd ILRC Conference, 24-28 July 2006, Nara, Japan*, pp. 179–182, 2006.
- Fritts, D. C., and M. J. Alexander, Gravity wave dynamics and effects in the middle atmosphere, *Rev. Geophys.*, *41*(1), 1003, doi:10.1029/2001RG000106, 2003.
- Galassi, M., J. Davies, J. Theiler, B. Gough, G. Jungman, M. Booth, and F. Rossi, *Gnu Scientific Library: Reference Manual*, Network Theory Ltd., 2003.
- Garnier, A., and M.-L. Chanin, Description of a Doppler Rayleigh LIDAR for Measuring Winds in the Middle Atmosphere, *Appl. Phys. B*, *55*, 35–40, 10.1007/BF00348610, 1992.
- Geller, M. A., Dynamics of the middle atmosphere, *Space Sci. Rev.*, *34*, 359–375, 1983.
- Geller, M. A., and J. Gong, Gravity wave kinetic, potential, and vertical fluctuation energies as indicators of different frequency gravity waves, *J. Geophys. Res.*, *115*(D11), n/a–n/a, doi:10.1029/2009JD012266, 2010.
- Gerstenkorn, S., and P. Luc, *Atlas du spectre d'absorption de la molécule d'iode*, Edition du Centre national de la recherche scientifique, Paris, 1978.
- Hall, C. M., T. Aso, A. H. Manson, C. E. Meek, S. Nozawa, and M. Tsutsumi, High-latitude mesospheric mean winds: A comparison between Tromsø (69°N) and Svalbard (78°N), *J. Geophys. Res.*, *108*, doi:10.1029/2003JD003509, 2003.

- Hamilton, K., Climatological Statistics of Stratospheric Inertia-Gravity Waves Deduced From Historical Rocketsonde Wind and Temperature Data, *J. Geophys. Res.*, *96*, 20,831–20,839, 1991.
- Hansen, G., M. Servazi, and U. von Zahn, First detection of a noctilucent cloud by lidar, *Geophys. Res. Lett.*, *16*(12), 1445–1448, 1989.
- Hauchecorne, A., and M.-L. Chanin, Density and temperature profiles obtained by lidar between 35 and 70 km, *Geophys. Res. Lett.*, *7*, 565–568, doi:10.1029/GL007i008p00565, 1980.
- Hays, P. B., V. J. Abreu, M. E. Dobbs, D. A. Gell, H. J. Grassl, and W. R. Skinner, The High-Resolution Doppler Imager on the Upper Atmosphere Research Satellite, *J. Geophys. Res.*, *98*, 10,713, doi:10.1029/93JD00409, 1993.
- Hecht, J. H., Instability layers and airglow imaging, *Rev. Geophys.*, *42*(1), RG1001, doi:10.1029/2003RG000131, 2004.
- Hildebrand, J., G. Baumgarten, J. Fiedler, U.-P. Hoppe, B. Kaifler, F.-J. Lübken, and B. P. Williams, Combined wind measurements in the arctic middle atmosphere, *Atmos. Meas. Tech.*, *5*, 2433–2445, doi:10.5194/amt-5-2433-2012, 2012.²
- Hocking, W. K., Strengths and limitations of MST radar measurements of middle-atmosphere winds, *Ann. Geophys.*, *15*(9), 1111–1122, 1997.
- Hocking, W. K., B. Fuller, and B. Vandeppeer, Real-time determination of meteor-related parameters utilizing modern digital technology, *J. Atmos. Solar-Terr. Phys.*, *63*, 155–169, doi:10.1016/S1364-6826(00)00138-3, 2001.
- Hoffmann, P., private communication, 2012.
- Holton, J. R., *An Introduction to Dynamic Meteorology, International Geophysics Series*, vol. 48, 3 ed., 511 pp., Academic Press, San Diego, USA, 1992.
- Hoppe, U.-P., and D. C. Fritts, High-resolution measurements of vertical velocity with the European incoherent scatter VHF radar: 1. Motion field characteristics and measurement biases, *J. Geophys. Res.*, *100*(D8), 16,813–16,825, doi:10.1029/95JD01466, 1995.
- Hoppe, U.-P., G. Hansen, and D. Opsvik, Differential absorption LIDAR measurements of stratospheric ozone at ALOMAR: First results, in *Proceedings of the 12th ESA Symposium on European Rocket and Balloon Programmes and Related Research, Lillehammer, Norway (ESA SP-370)*, edited by B. Kaldeich-Schürmann, pp. 335–344, 1995.
- Huang, W., X. Chu, B. P. Williams, S. D. Harrell, J. Wiig, and C.-Y. She, Na double-edge magneto-optic filter for Na lidar profiling of wind and temperature in the lower atmosphere, *Opt. Lett.*, *34*, 199–201, doi:10.1364/OL.34.000199, 2009.
- Hyatt, H. A., J. M. Cherlow, W. R. Fenner, and S. P. S. Porto, Cross section for the Raman effect in molecular nitrogen gas, *J. Opt. Soc. America*, *63*(12), 1604–1606, doi:10.1364/JOSA.63.001604, 1973.

²Hildebrand, J., G. Baumgarten, J. Fiedler, U.-P. Hoppe, B. Kaifler, F.-J. Lübken, and B. P. Williams, Combined wind measurements in the Arctic middle atmosphere, *Atmos. Meas. Tech.*, *5*, 2433–2445, doi:10.5194/amt-5-2433-2012, 2012.

Bibliography

- Iimura, H., D. C. Fritts, M. Tsutsumi, T. Nakamura, P. Hoffmann, and W. Singer, Long-term observations of the wind field in the Antarctic and Arctic mesosphere and lower-thermosphere at conjugate latitudes, *J. Geophys. Res.*, *116*, D20112, doi:10.1029/2011JD016003, 2011.
- Kaifler, B., Na lidar at ALOMAR – electrooptic improvements, analysis algorithms, and selected atmospheric observations 80 to 100 km above Northern Norway, Master's thesis, University of Ulm, 2009.
- Keckhut, P., F. J. Schmidlin, A. Hauchecorne, and M.-L. Chanin, Stratospheric and mesospheric cooling trend estimates from U.S. rocketsondes at low latitude stations (8°S–34°N), taking into account instrumental changes and natural variability, *J. Atmos. Solar-Terr. Phys.*, *61*(6), 447–459, doi:http://dx.doi.org/10.1016/S1364-6826(98)00139-4, 1999.
- Kent, G. S., and R. W. H. Wright, A review of laser radar measurements of atmospheric properties, *J. Atmos. Terr. Phys.*, *32*, 917–943, 1970.
- Killeen, T. L., Q. Wu, S. C. Solomon, D. A. Ortland, W. R. Skinner, R. J. Niecejewski, and D. A. Gell, TIMED Doppler Interferometer: Overview and recent results, *J. Geophys. Res.*, *111*, A10S01, doi:10.1029/2005JA011484, 2006.
- Korb, C. L., B. M. Gentry, and C. Y. Weng, Edge technique: theorie and application to the lidar measurement of atmospheric wind, *Appl. Optics*, *31*, 4202–4213, 1992.
- Kristoffersen, S. K., W. E. Ward, S. Brown, and J. R. Drummond, Calibration and validation of the advanced E-Region Wind Interferometer, *Atmos. Meas. Tech.*, *6*(7), 1761–1776, doi:10.5194/amt-6-1761-2013, 2013.
- Kumar, G. K., and W. K. Hocking, Climatology of northern polar latitude MLT dynamics: mean winds and tides, *Ann. Geophys.*, *28*, 1859–1876, doi:10.5194/angeo-28-1859-2010, 2010.
- Labitzke, K., Temperature changes in the mesosphere and stratosphere connected with circulation changes in winter, *J. Atmos. Sci.*, *29*, 756–766, 1972.
- Labitzke, K., Stratospheric-mesospheric midwinter disturbances: A summary of observed characteristics, *J. Geophys. Res.*, *86*(C10), 9665–9678, doi:10.1029/JC086iC10p09665, 1981.
- Liu, A. Z., W. K. Hocking, S. J. Franke, and T. Thayaparan, Comparison of Na lidar and meteor radar wind measurements at Starfire Optical Range, NM, USA, *J. Atmos. Solar-Terr. Phys.*, *64*, 31–40, doi:10.1016/S1364-6826(01)00095-5, 2002.
- Liu, Z. S., B. Y. Liu, Z. G. Li, Z. A. Yan, S. H. Wu, and Z. B. Sun, Wind measurements with incoherent Doppler lidar based on iodine filters at night and day, *Appl. Phys. B*, *88*, 327–335, doi:10.1007/s00340-007-2674-y, 2007.
- Lübken, F.-J., Thermal structure of the Arctic summer mesosphere, *J. Geophys. Res.*, *104*(D8), 9135–9149, doi:10.1029/1999JD900076, 1999.
- Lübken, F.-J., and A. Müllemann, Temperatures, densities, and winds in the high latitude (78°N) mesosphere, *Adv. Space Res.*, *32*(5), 731–740, doi:10.1016/S0273-1177(03)00408-3, 2003.

- Lübken, F.-J., and U. von Zahn, Thermal Structure of the Mesopause Region at Polar Latitudes, *J. Geophys. Res.*, *96*, 20, 841–20, 857, 1991.
- Manney, G. L., M. J. Schwartz, K. Krüger, M. L. Santee, S. Pawson, J. N. Lee, W. H. Daffer, R. A. Fuller, and N. N. J. Livesey, Aura Microwave Limb Sounder observations of dynamics and transport during the record-breaking 2009 Arctic stratospheric major warming, *Geophys. Res. Lett.*, *36*(12), doi:10.1029/2009GL038586, 2009.
- Markwardt, C. B., Non-linear Least-squares Fitting in IDL with MPFIT, in *Astronomical Data Analysis Software and Systems XVIII, Astronomical Society of the Pacific Conference Series*, vol. 411, edited by D. A. Bohlender, D. Durand, and P. Dowler, p. 251, 2009.
- Matsuno, T., A dynamical model of the stratospheric sudden warming, *J. Atmos. Sci.*, *28*, 1479–1494, 1971.
- Matthias, V., P. Hoffmann, A. Manson, C. Meek, G. Stober, P. Brown, and M. Rapp, The impact of planetary waves on the latitudinal displacement of sudden stratospheric warmings, *Ann. Geophys.*, *31*(8), 1397–1415, doi:10.5194/angeo-31-1397-2013, 2013.
- Meinel, I. A. B., OH Emission Bands in the Spectrum of the Night Sky., *Astrophys. J.*, *111*, 555, doi:10.1086/145296, 1950.
- Meriwether, J. W., and A. J. Gerrard, Mesosphere inversion layers and stratosphere temperature enhancements, *Rev. Geophys.*, *42*(3), RG3003, doi:10.1029/2003RG000133, 2004.
- Meyer, W., C. R. Philbrick, J. Röttger, R. Ruster, H.-U. Widdel, and F. J. Schmidlin, Mean winds in the winter middle atmosphere above northern Scandinavia, *J. Atmos. Terr. Phys.*, *49*(7-8), 675–687, doi:10.1016/0021-9169(87)90012-2, 1987.
- Michels, H., *The Data Plotting Software DISLIN*, Shaker Media GmbH, 2010.
- Mishchenko, M. I., J. W. Hovenier, and L. D. Travis, *Light scattering by nonspherical particles: Theory, measurements, and applications*, 690 pp., Academic Press, San Diego, USA, 1999.
- Müllemann, A., and F.-J. Lübken, Horizontal winds in the mesosphere at high latitudes, *Adv. Space Res.*, *35*(11), 1890–1894, 2005.
- Nastrom, G. D., T. E. Van Zandt, and J. M. Warnock, Vertical wavenumber spectra of wind and temperature from high-resolution balloon soundings over Illinois, *J. Geophys. Res.*, *102*(D6), 6685–6702, doi:10.1029/96JD03784, 1997.
- Nicklaus, K., V. Morasch, M. Höfer, J. Luttmann, M. Vierkoetter, M. Ostermeyer, J. Höffner, C. Lemmerz, and D. Hoffmann, Frequency stabilization of Q-switched Nd:YAG oscillators for airborne and spaceborne LIDAR systems, in *Proceedings of SPIE*, vol. 6451, doi:10.1117/12.701187, 2007.
- Olsen, R. O., and B. W. Kennedy, The Utilization of Starute Decelerators for Improved Upper Atmosphere Measurements, *Tech. Rep. ECOM-5551*, Atmospheric Sciences Laboratory, 1974.
- Picone, J. M., A. E. Hedin, D. P. Drob, and A. C. Aikin, NRLMSISE-00 empirical model of the atmosphere: Statistical comparison and scientific issues, *J. Geophys. Res.*, *107*(A12), 1468, doi:10.1029/2002JA009430, 2002.

Bibliography

- Placke, M., P. Hoffmann, M. Gerding, E. Becker, and M. Rapp, Testing linear gravity wave theory with simultaneous wind and temperature data from the mesosphere, *J. Atmos. Solar-Terr. Phys.*, *93*(0), 57–69, doi:http://dx.doi.org/10.1016/j.jastp.2012.11.012, 2013.
- Rasetti, F., Incoherent scattered radiation in diatomic molecules, *Phys. Rev.*, *34*, 367–371, 1929.
- Rees, D., M. Vyssogorets, N. P. Meredith, E. Griffin, and Y. Chaxell, The Doppler Wind and Temperature System of the ALOMAR Lidar facility: overview and initial results, *J. Atmos. Terr. Phys.*, *58*(16), 1827–1842, 1996.
- Rüfenacht, First middle-atmospheric zonal wind profile measurements with a new ground-based microwave Doppler-spectro-radiometer, *Atmos. Meas. Tech.*, *5*, 2647, 2012.³
- Sandford, D. J., C. L. Beldon, R. E. Hibbins, and N. J. Mitchell, Dynamics of the Antarctic and Arctic mesosphere and lower thermosphere – Part 1: Mean winds, *Atmos. Chem. Phys.*, *10*, 10,273–10,289, doi:10.5194/acp-10-10273-2010, 2010.
- Sato, A statistical study of the structure, saturation and sources of inertio-gravity waves in the lower stratosphere observed with the mu radar, *J. Atmos. Terr. Phys.*, 1994.⁴
- Schmidlin, F. J., H. Lee, and W. Michel, The Inflatable Sphere: A Technique for the Accurate Measurement of Middle Atmosphere Temperatures, *J. Geophys. Res.*, *96*(D12), 22,673–22,682, doi:10.1029/91JD02395, 1991.
- Schöch, A., Thermal structure and gravity waves in the Arctic middle atmosphere above ALOMAR (69.3°N, 16.0°E), Ph.D. thesis, Universität Rostock, 2007.
- Schöch, A., G. Baumgarten, and J. Fiedler, Polar middle atmosphere temperature climatology from Rayleigh lidar measurements at ALOMAR (69°N), *Ann. Geophys.*, *26*(7), 1681–1698, 2008.
- Seidel, D. J., R. J. Ross, and J. K. Angell, Climatological characteristics of the tropical tropopause as revealed by radiosondes, *J. Geophys. Res.*, 2001.
- She, C.-Y., J. D. Vance, B. P. Williams, D. A. Krueger, H. Moosmuller, D. Gibson-Wilde, and D. Fritts, Lidar studies of atmospheric dynamics near polar mesopause, *Trans. Am. Geophys. Union (EOS)*, *83*, 289–, doi:10.1029/2002EO000206, 2002.
- Shepherd, G. G., G. Thuillier, W. A. Gault, B. H. Solheim, C. Hersom, J. M. Alunni, J.-F. Brun, S. Brune, P. Charlot, and L. L. Cogger, WINDII, the wind imaging interferometer on the Upper Atmosphere Research Satellite, *J. Geophys. Res.*, *98*, 10,725, doi:10.1029/93JD00227, 1993.
- Shibata, Y., C. Nagasawa, M. Abo, and T. Nagai, System Evaluation of an Incoherent Wind Doppler LIDAR Using an Iodine Filter, *Jpn. J. Appl. Phys.*, *48*(3), 032,401, doi:10.1143/JJAP.48.032401, 2009.

³Rüfenacht, R., N. Kämpfer, and A. Murk, First middle-atmospheric zonal wind profile measurements with a new ground-based microwave Doppler-spectro-radiometer, *Atmos. Meas. Tech.*, *5*, 2647, 2012.

⁴Sato, K., A statistical study of the structure, saturation and sources of inertio-gravity waves in the lower stratosphere observed with the mu radar, *J. Atmos. Terr. Phys.*, 1994.

- Singer, W., D. Keuer, P. Hoffmann, P. Czechowsky, and G. Schmidt, The ALOMAR-SOUSY radar: Technical design and further developments, in *Proceedings of the 12th ESA Symposium on European Rocket and Balloon Programmes and Related Research, Lillehammer, Norway (ESA SP-370)*, vol. ESA SP-370, edited by B. Kaldeich-Schürmann, pp. 409–415, 1995.
- Singer, W., D. Keuer, and W. Eriksen, The ALOMAR MF radar: Technical design and first results, in *Proceedings 13th ESA Symposium on European Rocket and Balloon Programmes and Related Research, Oeland, Sweden, 26-29 May 1997 (ESA SP-397)*, vol. ESA SP-397, edited by B. Kaldeich-Schürmann, pp. 101–104, 1997.
- Singer, W., J. Bremer, W. K. Hocking, J. Weiss, R. Latteck, and M. Zecha, Temperature and wind tides around the summer mesopause at middle and Arctic latitudes, *Adv. Space Res.*, 31(9), 2055–2060, doi:10.1016/S0273-1177(03)00228-X, 2003a.
- Singer, W., R. Latteck, D. A. Holdsworth, and T. Kristiansen, A new narrow beam MF radar at 3 MHz for studies of the high-latitude middle atmosphere: System description and first results, in *Proceedings of the 10th Workshop on Technical and Scientific Aspects of MST Radar (MST10), Peru, 2003b*.
- Singer, W., R. Latteck, and D. A. Holdsworth, A new narrow beam Doppler radar at 3 MHz for studies of the high-latitude middle atmosphere, *Adv. Space Res.*, 41, 1487–1493, doi:10.1016/j.asr.2007.10.006, 2007.
- Singer, W., P. Hoffmann, G. K. Kumar, N. J. Mitchell, and V. Matthias, Atmospheric Coupling by Gravity Waves: Climatology of Gravity Wave Activity, Mesospheric Turbulence and Their Relations to Solar Activity, in *Climate And Weather of the Sun-Earth System (CAWSES): Highlights from a priority program*, edited by F.-J. Lübken, Springer, Dordrecht, The Netherlands, accepted, 2012.
- Souprayen, C., A. Garnier, A. Hertzog, A. Hauchecorne, and J. Porteneuve, Rayleigh-Mie Doppler wind lidar for atmospheric measurements. I: Instrumental setup, validation, and first climatological results, *Appl. Optics*, 38, 2410–2421, doi:10.1364/AO.38.002410, 1999.
- Space Weather Prediction Center, Solar Proton Events Affecting the Earth Environment, <http://www.swpc.noaa.gov/ftpsdir/indices/SPE.txt>, accessed on 07.10.2013, 2013.
- Strelnikova, I., private communication, 2012.
- Suzuki, S., F.-J. Lübken, G. Baumgarten, N. Kaifler, R. Eixmann, B. P. Williams, and T. Nakamura, Vertical propagation of mesoscale gravity wave from the lower to the upper atmosphere, *J. Atmos. Solar-Terr. Phys.*, 97, 29–36, doi:10.1016/j.jastp.2013.01.012, 2013.
- Szewczyk, A., B. Strelnikov, M. Rapp, I. Strelnikova, G. Baumgarten, N. Kaifler, T. Dunker, and U.-P. Hoppe, Simultaneous observations of a Mesospheric Inversion Layer and turbulence during the ECOMA-2010 rocket campaign, *Ann. Geophys.*, 31, 775–785, doi:10.5194/angeo-31-772-2013, 2013.
- Tepley, C. A., Neutral winds of the middle atmosphere observed at Arecibo using a Doppler Rayleigh lidar, *J. Geophys. Res.*, 99(D12), 25,781–25,790, doi:10.1029/94JD02213, 1994.
- von Cossart, G., private communication, 2013.

Bibliography

- von Zahn, U., J. Fiedler, B. Naujokat, U. Langematz, and K. Krüger, A note on record-high temperatures at the northern polar stratopause in winter 1997/98, *Geophys. Res. Lett.*, *25*(22), 4169–4172, doi:10.1029/1998GL900091, 1998.
- von Zahn, U., G. von Cossart, J. Fiedler, K. H. Fricke, G. Nelke, G. Baumgarten, D. Rees, A. Hauchecorne, and K. Adolfsen, The ALOMAR Rayleigh/Mie/Raman lidar: objectives, configuration, and performance, *Ann. Geophys.*, *18*, 815–833, 2000.
- Widdel, H.-U., Vertical movements in the middle atmosphere derived from foil cloud experiments, *J. Atmos. Terr. Phys.*, *49*(7/8), 723–741, doi:10.1016/0021-9169(87)90015-8, 1987.
- Widdel, H.-U., Foil chaff clouds as a tool for in-situ measurements of atmospheric motions in the middle atmosphere: Their flight behaviour and implications for radar tracking, *J. Atmos. Terr. Phys.*, *52*(2), 89–101, doi:10.1016/0021-9169(90)90071-T, 1990.
- Wu, D. L., M. J. Schwartz, J. W. Waters, V. Limpasuvan, Q. Wu, and T. L. Killeen, Mesospheric Doppler Wind Measurements from Aura Microwave Limb Sounder (MLS), *Adv. Space Res.*, *42*(7), 1246–1252, doi:http://dx.doi.org/10.1016/j.asr.2007.06.014, 2008.
- Xia, H., X. Dou, D. Sun, Z. Shu, X. Xue, Y. Han, D. Hu, Y. Han, and T. Cheng, Mid-altitude wind measurements with mobile rayleigh doppler lidar incorporating system-level optical frequency control method, *Opt. Express*, *20*(14), 15,286–15,300, doi:10.1364/OE.20.015286, 2012.
- Young, A. T., Rayleigh scattering, *Appl. Optics*, *20*(4), 533–535, 1981.
- Yuan, T., J. Yue, C.-Y. She, J. P. Sherman, M. A. White, S. D. Harrell, P. E. Acott, and D. A. Krueger, Wind-bias correction method for narrowband sodium Doppler lidars using iodine absorption spectroscopy, *Appl. Optics*, *48*, 3988, doi:10.1364/AO.48.003988, 2009.
- Yuan, T., B. Thuraiajah, C.-Y. She, A. Chandran, R. L. Collins, and D. A. Krueger, Wind and temperature response of midlatitude mesopause region to the 2009 Sudden Stratospheric Warming, *J. Geophys. Res.*, *117*(D9), D09,114, doi:10.1029/2011JD017142, 2012.

Acknowledgments

Finally, I like to thank everybody who helped me during the last years to finish this thesis, and everybody who contributed to acquire the data I used.

Nearly exactly five-and-a-half years ago I started this Ph.D. project. Prof. Dr. Franz-Josef Lübken offered me a Ph.D. position at IAP in Kühlungsborn and Dr. Gerd Baumgarten presented his ideas for this thesis, but he concealed its challenges. Well, since he helped me to solve these, I like to thank him for his guidance. He introduced me in detail to the ALOMAR RMR lidar, gave me hints how to analyze huge amounts of data, and provided and maintained an extensive *C* library (using it saved me a lot of time).

Dr. Jens Fiedler is the second person for me to ask whenever a question arose, concerning the lidar, data analysis, phrases in abstracts or this thesis. For me, his most sustainable suggestion was to try the text editor *Vim*, thank you!

Torsten Köpnick gave me very useful hints when I was programming software for the lidar; thank you for sharing some tiny part of your experience. I am also grateful for the lifts you gave me not only in winter.

I have been at ALOMAR a couple of times, mostly this was a great time. I like to thank the complete staff at the ALOMAR observatory for the warm welcomes and helping hands whenever needed, I am especially grateful to Reidar Lyngra. This thesis benefited from the excellent measurement effort of the ALOMAR staff and numerous voluntary lidar operators: thanks to Natalie Kaifler, Moritz Koza, and Michael Priester for contributing to successful winter campaigns. During my stays at ALOMAR it happened quite often, that I had to call for help, even during night; for their remote assistance I like to thank Prof. Dr. Götz von Cossart, Jens Fiedler, and Gerd Baumgarten.

When I started at IAP, I had only limited knowledge of *C* programming and no idea how to use the *Bash*. Therefore, I am grateful to Natalie Kaifler for a lot of help and hints.

Dr. Anne Haack read part of this manuscript and suggested some smooth phrases. Michael Priester helped me whenever I was frustrated by the printers.

The data presented in Sect. 5.2.3 have been published in a joint research article; I thank all the co-authors for their help during the compilation of that manuscript, and especially Bernd Kaifler for providing the Na lidar data.

Dr. Irina Strelnikova and Dr. Peter Hoffmann provided the radar data that I used in this thesis, thank you.

The European Centre for Medium-Range Weather Forecasts (ECMWF) is gratefully acknowledged for providing the operational analysis data.

The DORIS project is supported by DFG (Deutsche Forschungsgemeinschaft, BA 2834/1-1).

Selbständigkeitserklärung

Hiermit versichere ich an Eides statt, die vorliegende Arbeit selbständig und ohne fremde Hilfe verfasst, keine außer den von mir angegebenen Quellen und Hilfsmitteln verwandt und die den genutzten Werken inhaltlich oder wörtlich entnommenen Stellen als solche kenntlich gemacht zu haben.

Kühlungsborn, den 24. Oktober 2013

(Jens Hildebrand)